EFFECTIVE AND APPARENT ELASTIC STIFFNESS

TENSORS FOR POROUS SOLIDS UTILIZING

BOUNDARY ELEMENT ANALYSIS

by

Bashir Saad Elmabrouk

A thesis submitted to the Faculty and the Board of Trustees of the Colorado School of Mines in partial fulfillment of the requirements for the degree of Doctor of Philosphy (Engineering).

Golden, Colorado
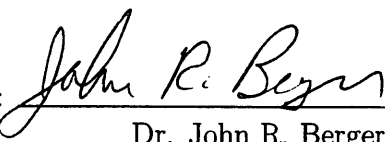
Date _March 16, 2012_

Signed: _____
Bashir Saad Elmabrouk

Signed: _____
Dr. John R. Berger
Thesis Advisor

Golden, Colorado

Date _March 16, 2012_

Signed: _____
Dr. John R. Berger
Interim Head
Department of Mechanical Engineering

ii

ABSTRACT

To accurately model the mechanical behavior of a wide range of porous materials, a predictive numerical model using the boundary element method is presented. Furthermore, this dissertation establishes a new method for predicting the homogenized orthotropic elastic properties of porous solids (ceramics, sintered materials, foams, etc) utilizing a symmetric Galerkin boundary element method (SGBEM) and the material fabric tensor. Several tools are used to extract the stiffness tensor of porous materials with different microstructural features. We use boundary element analysis, material fabric tensor, and homogenization theory to predict the apparent and effective elastic properties.

In homogenization theory, a representative volume element (RVE) selected for voided solids can often be too large for numerical or experimental determination of effective elastic constants. Volume elements which are smaller than the RVE can be useful in extracting apparent elastic stiffness tensors which provide bounds on the homogenized elastic stiffness tensor. The effects of boundary conditions, volume fraction, pore shape, and pore distribution on the elastic properties are the main questions answered by this dissertation.

The approach adopted here makes efficient use of SGBEM to compute the volume averages of stress and strain needed for the analysis. The boundary integral equations needed for calculation of the volume averages of stress and strain are easily evaluated from the variables appearing in the boundary element analysis. The methods developed here were successfully applied to samples of lead zirconate titanate (PZT) ceramic and excellent agreement with experimental results was obtained. For this analysis, PZT ceramic micrographs of different porosity and pores shape were analyzed and the eigenvalues of the fabric tensors calculated. Predictions of the apparent elastic constants as a function of solid volume fraction were then made. Furthermore,

the effect of material volume fraction, pore shape, and pore orientation on the fabric tensor for some idealized materials is presented. Additionally, the uncertainties in these parameters and the resulting uncertainties in the elastic constants were determined.

TABLE OF CONTENTS

LIST OF FIGURES

LIST OF ABBREVIATIONS

The Green's Function . . . . GF

Representative Volume Element . . . . RVE

Boundary Element Method . . . . BEM

Symmetric Galerkin Boundary Element Method . . . . SGBEM

Mean Intercept Length . . . . MIL

Star Volume Distribution . . . . SVD

Star Length Distribution . . . . SLD

Fabric Tensor . . . . FT

Porous lead zirconate titanate . . . . PZT

Kinematic Uniform Boundary Conditions . . . . KUBC

Static Uniform Boundary Conditions . . . . SUBC

Mixed Uniform Boundary Conditions . . . . MUBC

ACKNOWLEDGEMENTS

To my parents, Al-Haj Saad and Al-Hajja Alsharda.

CHAPTER 1

INTRODUCTION

In this first chapter, a brief background and the motivation for the dissertation are presented. The main objectives and scope of the dissertation are precisely stated and identified. Finally, the organization and the outline of the dissertation are clarified in the last section of this chapter.

1.1 Background and Motivation

Materials which consist of continuous matrices containing multiple pores or cracks of different size, shape and orientation are called cellular or porous materials [16]. Sponge, wood, cork, and cancellous bone are examples of natural porous solids. Some porous materials like ceramics and metallic foams are light weight and have good stiffness and excellent strength which made them a suitable selection for many applications in lightweight structures.

The mechanical properties of porous solids are dependent on their microstructural geometry [38]. In order to investigate the mechanical properties of a porous solid, we assume it to be a linear elastic material and, hence, can be characterized by a fourth-rank elastic stiffness tensor which relates the stress to the strain tensor [7]. The mechanical behavior of porous solids is very complicated and includes effects due to porosity, heterogeneity, anisotropy, micromechanics, load conditions and discontinuous behavior. In addition, traditional experimental methods have some difficulty estimating some of these properties.

The boundary element method (BEM) provides a significant platform in order to solve many physical and engineering problems. Boundary element analysis has emerged as a powerful alternative to finite elements particularly when high accuracy is required for problems such as certain stress analysis problems or when the domain

extends to infinity [23]. In BEM the discretization process is simpler, hence the codes are easier to use with mesh generators which is more difficult with finite elements.

In order to predict the apparent and effective "homogenized" stiffness tensors we have to assume that a statistically uniform homogeneous element, termed a representative volume element (RVE), can be defined in the porous solid. The RVE is defined to be large enough to contain the typical microstructure of the material, but it must be sufficiently small so that homogeneous displacements and tractions can be applied on its boundary. In numerical homogenization theory, three different scales are involved, the *macroscopic* scale on which the size of the pores is very small, the *mesoscopic* level which is the RVE level, and the *microscopic* level where the size of the volume element is less than RVE, see Figure 1.1. In many situations, an RVE can not be realized and we must work with volumes smaller than the RVE. For volume elements which are smaller than the RVE, elastic stiffness tensors can be defined which also provide bounds on the homogenized elastic stiffness tensor. Finally, the relationship between the homogenized variables must be independent of the position or the size of the volume element and all the statistical information about the material is supposed to be available in one single realization of this volume element, which mathematically is called the ergodicity assumption [31].
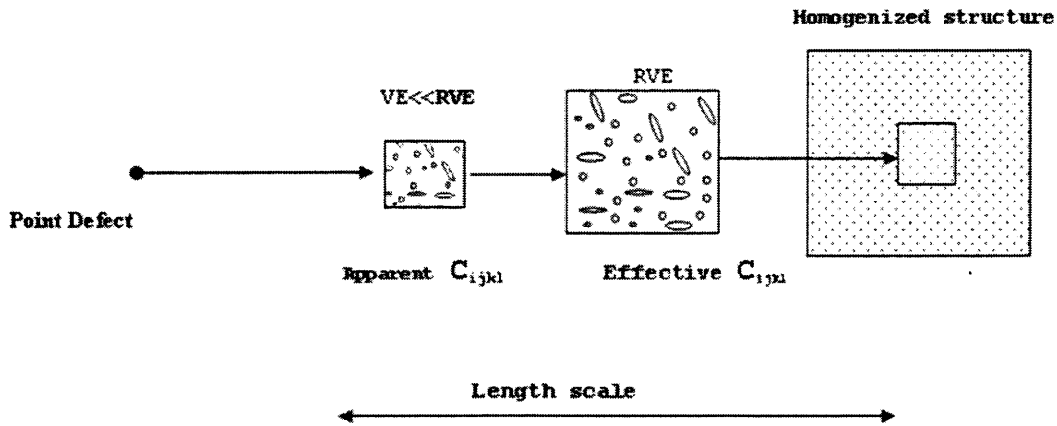
Figure 1.1: Representative Volume Element (RVE) and volume element less than the RVE.

2

Boundary element analysis of the volume elements is an excellent technique to estimate apparent and effective properties of a porous solid. The numerical analysis of a volume element by the BEM is dependent on a good understanding of the relationship between the applied boundary condition and elastic stiffness tensors. This dissertation is centered on the numerical analysis of volume elements (RVE), stress/strain volume (area) averaging and the effect of fabric tensor on material properties. Therefore, special attention is paid to the boundary conditions imposed on the volume elements as this plays a significant role in the homogenization problem. Special attention will also be paid to the application of Hill's criterion which expresses the principle of virtual work between the microscopic and the macroscopic level of the structure. The homogenization approach and the boundary element method formulation will be analyzed and discussed in detail in subsequent chapters of this dissertation.

1.2 Scope and Objectives

The principal aim of this dissertation is to create a predictive numerical model for studying mechanical properties for a wide range of porous solids. Specifically, we will use a fabric tensor approach to characterize the microstructure, and use a Symmetric Galerkin Boundary Element Method (SGBEM) to compute mechanical properties. Computational models are used in concert with published experimental findings and theoretical formulations to offer effective conclusions to materials scientists and engineers. The general objectives undertaken in this dissertation are:

1. Boundary element analysis of volume elements to determine the 2D orthotropic elastic properties of a number of porous solids by use of the fabric tensor.

2. Study the effect of porosity and pore shapes on the effective and apparent elastic stiffness tensors in a wide range of idealized models.

3. Perform a numerical investigation to study the influence of representative vol-

ume element size on the effective and apparent elastic properties of solids with voids.

4. Compare and study three methods of constructing the fabric tensors, namely, Mean Intercept Length (MIL), Star Length Distribution (SLD), and Star Volume Distribution (SVD) and investigate the error propagation in apparent elastic constants from each method.

1.3 Outline of the Dissertation

The Chapters of the dissertation are organized as follows:

In Chapter 2, a critical review and state of art of the effective and apparent elastic constants for porous solids are presented. In this regard, it should be noted that all prior homogenization models are formulated with the purpose of obtaining the effective properties of the materials. The fabric tensor definition and some methods of analysis of structural anisotropy such as mean intercept length are covered and compared. Additionally, the relationships between the fabric tensor and material elastic constants are also reviewed.

Chapter 3 presents a comprehensive formulation of the Boundary Element Method (BEM) and the Symmetric Galerkin Boundary Element Method (SGBEM). Green's function and Boundary Integral Equations (BIE) in elasticity are also reviewed. Finally, a BEM approach to the calculation of the stress/strain volume averages is presented.

Chapter 4 presents the effect of different types of applied boundary conditions on the volume element to prediction of apparent elastic constants. In this study three types of boundary conditions are applied: kinematic uniform boundary conditions (KUBC), static uniform boundary conditions (SUBC) and mixed uniform boundary conditions (MUBC). We next apply the developed methodology to two porous ceramic specimens. The effect of RVE size is studied, and the variation of elastic moduli with

porosity of the ceramics is predicted and plotted.

The effect of pore shapes and size on the fabric tensor of porous solids are presented in Chapter 5. Three idealized models with different aspect ratios are generated and numerically studied. In one case, the fabric tensor is kept fixed to study the effect of the porosity change on the apparent elastic constants. The details of these numerical models, as well as the boundary element analysis and volume average calculations, are studied and examined in Chapter 5.

Sensitivity and error analysis of the material fabric tensors are presented and analyzed in Chapter 6. Also, investigations conducted on uncertainty in the fabric tensors and the subsequent errors in material anisotropy calculations is presented. Finally, the remainder of the dissertation discusses additional suggestions on homogenization theory and fabric-elastic constant relationships.

CHAPTER 2

ELASTIC CONSTANTS OF POROUS SOLIDS

Any material containing matrix solids with multiple pores or cracks is called a cellular or porous solids. Many engineering and natural materials, including cork, wood, cancellous bone, ceramics, composites and metals sintered from powder compacts are essentially porous. These materials have a complex microstructure which can be described by the shape, size and orientation of the pores, Figure 2.1. Estimation of the effective elastic moduli of such materials, characterized by microscopic heterogeneity, pore shapes and size, has been a matter of considerable interest for some time. Representative volume elements (RVEs) from voided solids can often be too large for numerical or experimental determination of effective elastic constants. Volume elements (VEs) which are smaller than the RVE can be used in extracting apparent elastic stiffness tensors which provide bounds on the homogenized elastic stiffness tensor.
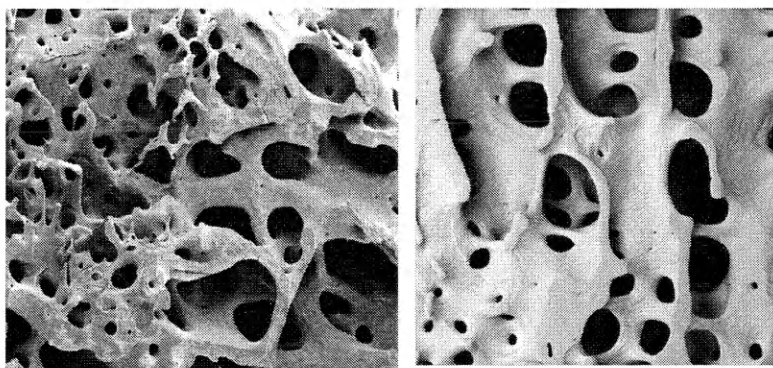
Figure 2.1: Complex porous solid (cancellous bone) [21].

The simplest characteristic feature of a porous solid is its volume fraction, v_s, which is the solid volume of the matrix solid material divided by total volume,

$$v_s = \frac{V_m}{V_m + V_v} \tag{2.1}$$

6

where V_m is the matrix volume and V_v is the voids volume. The porosity Φ is often used, where $\Phi = 1 - v_s$. However, the solid volume fraction is *not* sufficient to predict mechanical properties.

2.1 Examples of Porous Solids

From an engineering viewpoint, porous solids can be classified by different criteria such as pore size, shape and production methods. As mentioned above, wood, cork, sponge and cancellous bone are all examples of natural porous solids. Metallic foams, polymers, and porous ceramics are widely used in modern industries, e.g., aircraft, automotive, biomechanics applications and many others. Another example of a porous material is syntactic foams which are composite materials synthesized by filling a metal, polymer, or ceramic matrix with hollow particles. Syntactic foams are widely used for marine applications, aerospace, and ground transportation vehicle applications [57].

Metallic foams are porous structures consisting of a solid metal containing a large volume fraction of gas-filled pores, see Figure 2.2. Metallic foams typically retain some physical properties of their base material. They have properties that make them suitable for a number of materials applications, such as lightweight structures and many other engineering application. The defining characteristic of metallic foams is a very high porosity, and the strength of foamed metal possesses a power law relationship to its density. The study of metallic foams has become attractive to researchers interested in materials science and engineering applications. For many potential applications, an understanding of the mechanical behavior of these foams is necessary.

Ceramics can be prepared by heating and subsequent cooling, and have partly crystalline structure [45]. With the growing needs for porous ceramics in many material applications, a number of scientists have developed new technologies for fabri-

cating these materials while attempting to control their pore characteristics and to identify pore-related properties [44]. An example of a porous ceramic is the porous lead zirconate titanate (PZT 95/5) ferroelectric ceramic shown in Figure 2.3 also repeated as Figure 4.1. These materials were made by sintering compacts consisting of PZT and pore formers [75].
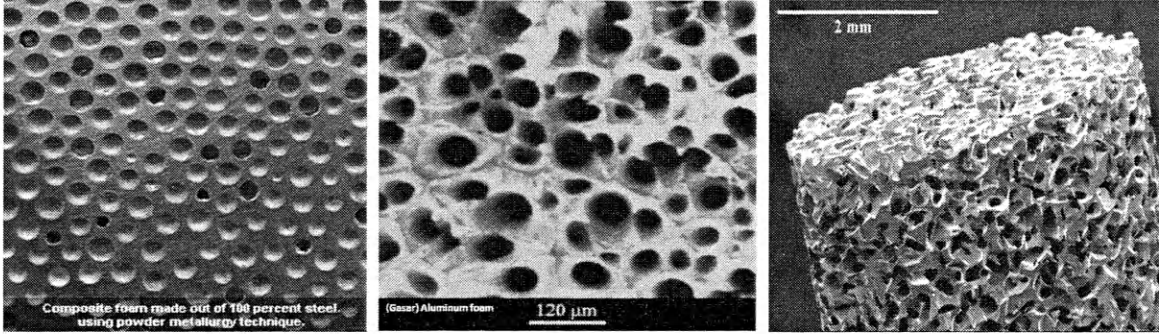
Figure 2.2: 2D and 3D Metallic Foams [71].

The mechanical behavior of two particular kinds of PZT ceramics as a function of pore shape and porosity is presented later in the dissertation.
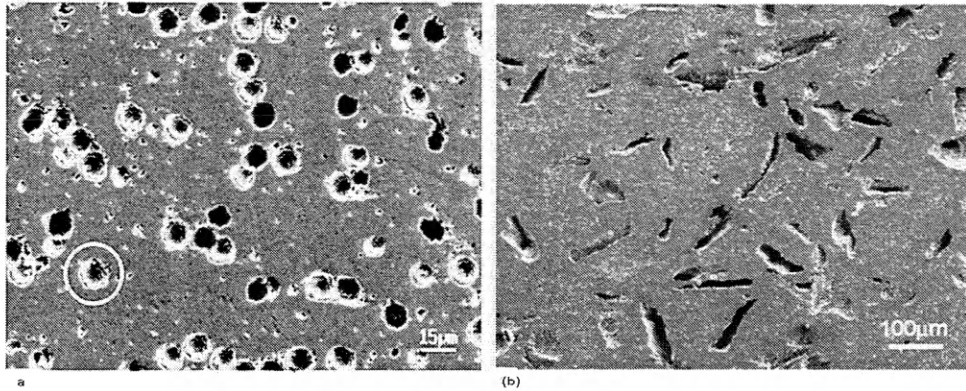
Figure 2.3: Micrographs of Porous Lead Zirconate Titanate (PZT) Ceramics [75].

2.2 Homogenization: RVE's and Volumes Smaller Than RVE

In mechanics of porous materials, we seek to calculate the apparent or effective stiffness tensors when the constitution and geometry of the material are known. Ho-

8

mogenization theory has a rich history starting from the early work of Hill [28], Kroner [39], Hashin [24] and Hashin and Shtrikman [25], and many others. Recently, a critical review and an excellent state of the art of the homogenization approach in micromechanics was provided by Pindera, et al. [56]. The representative volume element (RVE) technique is widely used in numerical homogenization approaches. An RVE is defined to be large enough to statistically contain all microstructural details of the material, but it must be sufficiently small so that homogenous displacement and traction boundary conditions can be applied [66]. Briefly, an RVE contains sufficient statistical and microstructural information to be representative of any similar volume taken from any location in the heterogeneous solid. We then assume that elastic properties extracted from the volume averages of stress and strain on the volume element can be taken as the overall properties of the homogenized material. RVE size is a significant criterion in the accuracy of the determination of the overall elastic stiffness tensors and plays an important role in homogenization theory. Investigations on the size of RVE have been conducted by a number of researchers using numerical simulation. For instance, Houdaigui, et al. [11] applied a computational homogenization scheme to estimate the size of RVE for linear elastic polycrystalline copper. They showed that the shape of a RVE is not necessarily a small size cube and the effective properties do not exist for all types of polycrystalline aggregates. Furthermore, in comparison with standard mechanics, Hollister and Kikuchi [29] preferred using the homogenization theory over standard mechanics of materials approach for periodic microstructures in composite materials.

2.2.1 Concept of Homogenization

A heterogeneous solid behaves similarly at the macroscopic level and in its constituents (microscopic level), but with different, effective, values of the material properties. In microstructural approaches the stress and strain fields in a heterogeneous

9

material are split into contributions corresponding to different length scales. It is assumed that these length scales are sufficiently different so that fluctuations of the stress and strain fields at the microscopic level influence the macroscopic level behavior at the larger length scale only via their volume averages [50]. Furthermore, compositional gradients of the stress and strain fields at the macroscopic level are not significant at the smaller length scale, where these fields appear to be locally constant and can be described in terms of uniform applied stresses and strains [39].

Mathematically, the strain and stress fields are split as

$$\varepsilon_{ij} = \langle \varepsilon_{ij} \rangle + \varepsilon'_{ij} \qquad \text{and} \qquad \sigma_{ij} = \langle \sigma_{ij} \rangle + \sigma'_{ij}, \tag{2.2}$$

where $\langle \varepsilon_{ij} \rangle$ and $\langle \sigma_{ij} \rangle$ are the stress and strain at the macroscopic level (volume averages), whereas ε'_{ij} and σ'_{ij} stand for the microscopic fluctuations.

For any RVE, the strain and stress at the microscopic level, ε_{ij} and σ_{ij}, and the corresponding macroscopic responses, $\langle \varepsilon_{ij} \rangle$ and $\langle \sigma_{ij} \rangle$, can be written as:

$$\varepsilon_{ij} = A(x)_{ik} \langle \varepsilon_{kj} \rangle \qquad \text{and} \qquad \sigma_{ij} = B(x)_{ik} \langle \sigma_{kj} \rangle. \tag{2.3}$$

Where $A(x)_{ik}$ and $B(x)_{ik}$ are second rank tensors.

At the macroscopic level of stress, strain, or composition, homogenization relations can be defined as

$$\langle \varepsilon_{ij} \rangle = \frac{1}{V} \int_V \varepsilon_{ij} \; dV \tag{2.4}$$
$$= \frac{1}{2V} \int_\Gamma (u_i n_j + u_j n_i) d\Gamma$$

$$\langle \sigma_{ij} \rangle = \frac{1}{V} \int_V \sigma_{ij} \; dV \tag{2.5}$$
$$= \frac{1}{2V} \int_\Gamma (t_i x_j + t_j x_i) d\Gamma,$$

where the divergence theorem was used to reduce the volume integrations to surface

integrations. where V and Γ are the volume and the surface of the region under consideration, u_j is the displacement vector, $t_i = \sigma_{ij}n_j$ is the surface traction, and n_j is the surface normal vector. The second rank tensors, $A(\mathbf{x})$ and $B(\mathbf{x})$ are called mechanical strain and stress concentration tensors (or influence functions), respectively [40]. Note that Eqs. (2.2), (2.3) and (2.5) imply that volume averages of fluctuations vanish for sufficiently large integration volumes,

$$\frac{1}{V} \int_V \varepsilon'_{ij} \, dV = \frac{1}{V} \int_V \sigma'_{ij} \, dV = 0.$$

(2.6)

Similarly, surface integrals over fluctuations typically vanish. The general statically admissible stress fields σ_{ij} and kinematically admissible strain fields ε_{ij} then satisfy

$$\int_V \sigma_{ij}\varepsilon_{ij} \, dV = \int_V \sigma_{ij} \, dV \int_V \varepsilon_{ij} \, dV.$$

(2.7)

For the special cases of homogeneous stress and strain boundary conditions then Eq. (2.7) can be shown to hold by transforming the volume integrals into surface integrals, to which the fluctuations σ'_{ij} and ε'_{ij} vanish. This is referred to as Hill's lemma [28]. Such conditions imply that the volume averaged strain energy density of an heterogeneous material can be obtained from the volume averages of the stresses and strains, provided the micro- and macroscopic levels are sufficiently different. Accordingly, homogenization can be interpreted as finding a homogeneous comparison material that is energetically and mechanically equivalent to a given microstructural material. The microscopic levels of real heterogeneous materials are at least to some extent random and highly complex. Exact expressions for $A(\mathbf{x}), B(\mathbf{x}), \varepsilon_{ij}, \sigma_{ij}$ are realistically hard to determine, so approximations have to be made. These approximations are based on the assumption that the heterogeneous material is statistically homogeneous. Thus, mesoscopic levels and RVEs selected randomly within the sample are taken to give rise to the same averaged material properties which, in turn, correspond to the material's overall or effective material properties [39]. Note that

we must still satisfy the ergodicity assumption: all statistical information about the material must be contained in the RVE.

As mentioned, the homogenization volume should be selected to be a representative reference volume element (RVE), i.e., a volume element that is statistically representative of the material microscopic level. Such a volume element must be sufficiently large to allow a meaningful sampling of the microscopic level and sufficiently small for the influence of macroscopic gradients to be negligible and for an analysis of the microscopic levels to be possible. Hashin and Shtrikman [25] stated this symbolically as MACRO>>MESO>>MICRO, where MICRO is the apparent elastic constants level, MACRO scale is where the size of the pores is very small, and MESO stands for the length scale of the RVEs.

The homogenized strain and stress fields of an elastic heterogeneous solid as obtained by Eq. (2.2), $\langle \varepsilon_{ij} \rangle$ and $\langle \sigma_{ij} \rangle$, can be linked by the effective elastic tensors C^e_{ijkl} and S^e_{ijkl} as:

$$\langle \varepsilon_{ij} \rangle = S^e_{ijkl} \langle \sigma_{kl} \rangle \quad and \quad \langle \sigma_{ij} \rangle = C^e_{ijkl} \langle \varepsilon_{kl} \rangle, \tag{2.8}$$

which may be viewed as the elastic tensors of an appropriate equivalent homogeneous material [66]. Using Eq. (2.4) and Eq. (2.5) these effective elastic tensors can be obtained from the local elastic tensors C_{ijkl} and S_{ijkl} then from the concentration tensors $A(\mathbf{x})$ and $B(\mathbf{x})$ as volume averages:

$$C^e_{ijkl} = \frac{1}{V} \int_V C_{ijkl} A(\mathbf{x}) dV \tag{2.9}$$

$$S^e_{ijkl} = \frac{1}{V} \int_V S_{ijkl} B(\mathbf{x}) dV$$

In the above, C^e_{ijkl} and S^e_{ijkl} are the effective stiffness and the effective compliance tensors for the homogenized composite, respectively. Note that the effective stiffness and compliance tensors are not equal to simply the volume averages.

2.2.2 Concept of Effective and Apparent Elastic Constants

In this section, the definition of the apparent and effective properties of the solid is introduced. As mentioned previously, representative volume elements (RVEs) can often be too large for numerical or experimental determination of effective elastic constants. Volume elements which are smaller than the RVE can be useful in extracting *apparent* elastic stiffness tensors C_{ijkl}^a, which provide bounds on the homogenized elastic stiffness tensor [34]. Generally, in engineering modeling and calculations, materials are assumed as homogeneous continua and the macroscopic analysis calculates average stress and strain within the equivalent homogeneous structure.

Huet [31] presented some elegant results about the concept of effective and apparent elastic constants of a statistically uniform material. In this work, he states that when the material volume is statistically uniform, then

$$\langle \sigma_{ij} \rangle = C_{ijkl}^e \langle \varepsilon_{kl} \rangle \tag{2.10}$$

where σ_{ij} is the stress tensor, ε_{kl} is the strain tensor, $\langle \cdot \rangle$ represents the volume average of the quantity between the angled brackets and C_{ijkl}^e is the *effective* elastic stiffness tensor. This works on volumes greater than or equal to the RVE. Also, the loading conditions are such that homogeneous fields would result if the materials were homogeneous. Then C_{ijkl}^e is independent of the boundary conditions taken on the material volume.

If the local relationship is $\sigma_{ij} = C_{ijkl}\varepsilon_{kl}$, then Eq.(2.10) can be written as

$$\langle C_{ijkl}\varepsilon_{kl} \rangle = C_{ijkl}^e \langle \varepsilon_{kl} \rangle \tag{2.11}$$

which is a definition of C^e. We can also write this as

$$\langle C_{ijkl}\varepsilon_{kl} \rangle = \langle C_{ijkl} \rangle \langle \varepsilon_{kl} \rangle + \langle C_{ijkl}'\varepsilon_{kl}' \rangle \tag{2.12}$$

where $\langle C_{ijkl}'\varepsilon_{kl}' \rangle$ represents the fluctuation about the average value. Note here that

$\langle C_{ijkl} \rangle$ is *not* equal to C^e_{ijkl} which is also evident by Eq. (2.9). Hill [28] showed that $\langle C_{ijkl} \rangle$ is an upper bound for C^e_{ijkl}. Huet [31] termed this the Hill-Voigt upper bound on the stiffness tensor.

Alternatively, we can form an effective compliance tensor,

$$\langle S_{ijkl} \sigma_{kl} \rangle = S^e_{ijkl} \langle \sigma_{kl} \rangle, \tag{2.13}$$

which is a definition of S^e_{ijkl}. We can also write this as

$$\langle S_{ijkl} \sigma_{kl} \rangle = \langle S_{ijkl} \rangle \langle \sigma_{kl} \rangle + \langle S'_{ijkl} \sigma'_{kl} \rangle. \tag{2.14}$$

Again, $\langle S_{ijkl} \rangle$ is *not* equal to S^e. Hill [28] showed that $\langle S_{ijkl} \rangle$ is an upper bound for S^e_{ijkl}. Huet [31] termed this the Hill-Reuss upper bound on the compliance tensor, or equivalently the lower bound on the stiffness tensor.

One can also define effective properties from an energetic perspective by computing volume averages of stress and strain in a free-energy formulation. The energetic definition and the mechanical definition of the effective elastic stiffness tensors are the same if the Hill [28] criterion is satisfied,

$$\langle \sigma_{ij} \varepsilon_{ij} \rangle = \langle \sigma_{ij} \rangle \langle \varepsilon_{ij} \rangle, \tag{2.15}$$

which is another form for Eq. (2.7). Note that the Gauss theorem can be used to recast the Hill condition as

$$\int_{\Gamma} (t_i - \langle \sigma_{ij} \rangle n_j)(u_i - \langle \varepsilon_{ij} \rangle x_j) d\Gamma = 0 \tag{2.16}$$

where Γ is the boundary of the volume and $t_i = \sigma_{ij} n_j$, u_i, n_j and x_j are the components of the traction, displacement, normal and position vectors, respectively.

If certain boundary conditions can be identified which satisfy the Hill criterion, then an effective elastic stiffness tensor can be obtained which is identical from the mechanical and energetic definitions. This can then be done without any statistical assumptions concerning the volume element, which is of critical importance in the case

of volume elements smaller than the RVE. Recall that for the RVE, the relationship between stress and strain should be independent of the boundary conditions. If we are at a volume size less than the RVE this is no longer generally true.

2.2.3 Boundary Conditions and the Hill Criterion

Sab [61] and Huet [32] showed that a RVE may be defined as a volume that shows the same overall material properties irrespective of the boundary conditions applied. This definition of an RVE explains the dependence of the mechanical property on the size of the RVE considered [26]. Hill [28] demonstrated that the RVE must be structurally typical of the porous solid on average and must contain an adequate number of voids such that the apparent moduli are independent of the boundary conditions. He also showed that the necessary and sufficient conditions for equivalence between the energetically and mechanically defined properties of elastic materials are contained in the Hill condition, Eq.(2.15). Hashin and Shtrikman [25] stated that stress and strain fields in the RVE should be statistically homogeneous when subjected to homogeneous uniform boundary conditions. The accuracy of the RVE approximation depends on how well the assumed boundary conditions reflect each of the boundary conditions that the RVE is subjected in-situ.

In numerical modeling, the volume element available for analysis may be less than the RVE. The question then arises as to what one can say concerning the elastic stiffness or compliance tensors for the homogenized material. This question has been investigated in a series of papers [26], [27], [31], [54] where the idea of *apparent* elastic stiffness and compliance tensors was presented. Although, in general, stiffness-tensor results on a volume less than the RVE will be dependent on the specific boundary conditions taken, the boundary conditions can still be specified such that the Hill criterion is satisfied. Typically, these boundary conditions are taken as kinematic uniform boundary conditions (KUBC), static uniform boundary conditions (SUBC), or mixed

15

uniform boundary conditions (MUBC). Hill [28] originally determined the KUBC and SUBC, as these generate uniform strain (KUBC) or uniform stress (SUBC) conditions in the volume. The MUBC were developed by Hazanov [27] and [26], who also showed that for the apparent elastic stiffness and compliance tensors,

$$C^{\sigma}_{ijkl} \leq C^{m}_{ijkl} \leq C^{u}_{ijkl}, \quad S^{u}_{ijkl} \leq S^{m}_{ijkl} \leq S^{\sigma}_{ijkl} \tag{2.17}$$

where $C^{\sigma}_{ijkl}, C^{m}_{ijkl}$ and C^{u}_{ijkl} are the apparent stiffness tensors obtained from SUBC, MUBC, and KUBC, respectively, with similar notation used for the apparent compliance tensors. The MUBC were further refined as periodic mixed uniform boundary conditions (PMUBC) in [54]. Details concerning the various boundary conditions will be given later in the coming chapters.

Therefore, if we are using volumes less than the RVE, we can calculate upper and lower bounds on the stiffness or compliance tensor by applying SUBC or KUBC, or we can obtain an intermediate estimate using MUBC on the volume element. As the volume element becomes larger, these bounds eventually converge to the effective stiffness or compliance tensor, see Figure 2.4.
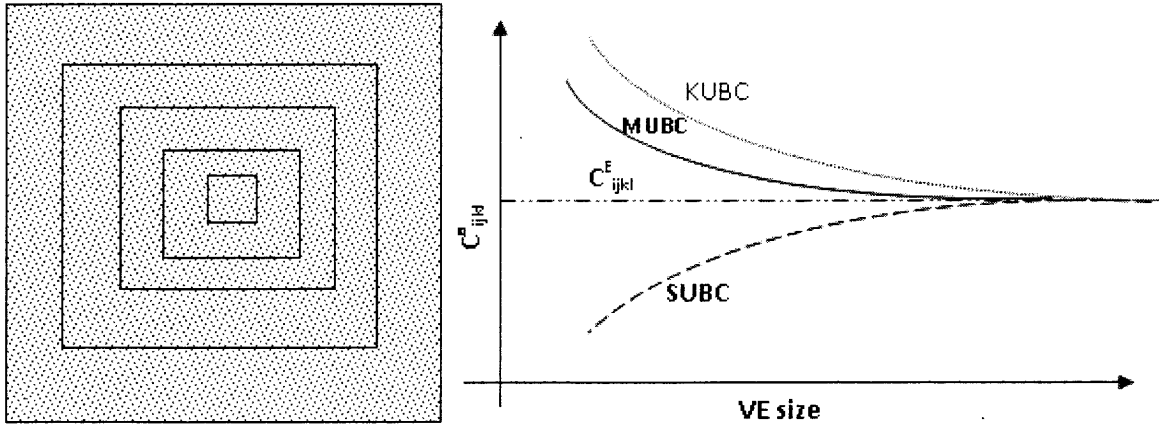
Figure 2.4: Volume element size and elastic constant values.

The Hill condition, Eq. (2.15) and Eq. (2.16), is satisfied by three different types

of boundary conditions for heterogeneous media. These boundary conditions have an important influence on the predicted elastic stiffness tensors by any numerical method. In the case of linear elasticity the Hill criterion is satisfied by three different types of boundary conditions. The displacements or the tractions are generally chosen to be uniform.

1. Kinematic Uniform Boundary Conditions (KUBC): (Dirichlet)

   The displacement u_i is imposed at point x_i belonging to the boundary such that:

$$u_i = \varepsilon_{ij}^0 x_j \quad \forall x_j \in \Gamma \tag{2.18}$$

2. Static Uniform Boundary Conditions see Figure 2.5 (SUBC): (Neumann)

$$t_i = \sigma_{ij}^0 n_j \quad \forall x_j \in \Gamma \tag{2.19}$$

3. Mixed Uniform Boundary Condition: (Mixed, MUBC)

$$(t_i - \sigma_{ij}^0 n_j)(u_i - \varepsilon_{ij}^0 x_j) = 0 \quad \forall x_j \in \Gamma \tag{2.20}$$

In Eqs. (2.18)-(2.20), ${}^0\varepsilon_{ij}$ and ${}^0\sigma_{ij}$ denote constant tensors, prescribed *a priori* on the volume element. In the case of MUBCs different combinations of *a priori* prescribed boundary values are possible but have to fulfill the above condition. Each of these BCs yields different "apparent" stiffness tensors [54] and are the source of the strong definition of the elastic effective tensor. These boundary conditions are frequently used in classical homogenization theorems. In this dissertation, the three types of boundary conditions are applied on cellular solid volume elements. Typical SUBCs applied to a volume element are shown in Figure 2.5.
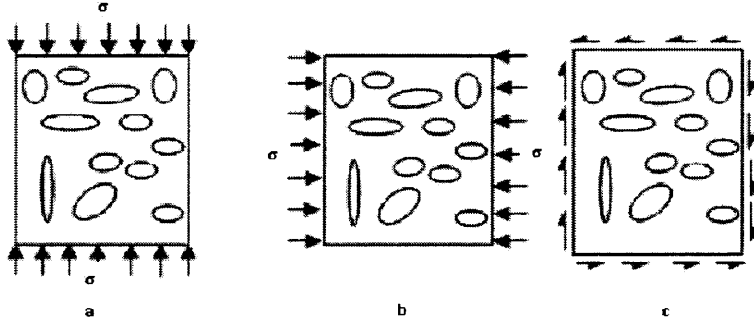
Figure 2.5: SUBCs Applied on Volume Element:

$$(a) \quad {}^0\sigma_{ij} = \begin{bmatrix} 0 & 0 \\ 0 & -\sigma \end{bmatrix}, \quad (b) \quad {}^0\sigma_{ij} = \begin{bmatrix} -\sigma & 0 \\ 0 & 0 \end{bmatrix}, \quad (c) \quad {}^0\sigma_{ij} = \begin{bmatrix} 0 & \sigma \\ \sigma & 0 \end{bmatrix}.$$

2.3 Fabric Tensor (FT)

In material science and its applications, the prediction of the elastic stiffness tensor as a function of the porosity or the solid volume fraction can be done utilizing the fabric tensor of the material. The fabric tensor is a second-rank tensor used to describe the nature of the structural anisotropy and provides information about the microstructure of the material [35]. The fabric tensor can therefore be used to characterize the microstructure of porous materials such as ceramics, foams, cancellous bone, and granular materials. The fabric tensor may be constructed from mean intercept lengths [22], volume orientation distribution [53], star-volume distribution [52], or the star-length distribution [65]. Whitehouse [74] showed that the fabric tensor is the key measurement of the structural anisotropy of cancellous bone. Harrigan, et al. [22] showed that a fabric tensor can be introduced to characterize the microstructure in various porous materials. Cowin [7] assumed that the matrix material of the porous elastic solid is isotropic and derived a relationship between the elastic constants of

18

a porous anisotropic material and the fabric tensor. In addition, he determined the anisotropy of the porous elastic solid by the fabric tensor and showed that the material symmetries of orthotropy, transverse isotropy and isotropy correspond to the cases of three, two and one distinct eigenvalues of the fabric tensor, respectively. These eigenvalues are used for quantification of structural anisotropy. In conclusion, in many cases the anisotropy and the orthotropic elastic properties of the porous elastic solid can be determined by the fabric tensor.

2.3.1 Mean Intercept Length (MIL)

The mean intercept length (MIL) is a method that has been used to quantify structural anisotropy of porous and cellular materials. MIL is the average distance, L, between the interfaces of a microstructure measured along a straight line, see Figure 2.6. Experimental data on cancellous bone samples by Harrigan and Mann [22] showed that a polar plot of L at the angle of measurement generates an ellipse in any plane cross-section intersecting a bone sample. The polar plot of mean intercept length is an ellipse whose principal axes and axes ratio describe microstructure orientation and anisotropy, respectively. The MIL was represented in [22] as a second rank tensor, $\mathbf{H}$, where it was shown that the mean intercept length, plotted as a radius at the angle of measurement, generates an ellipse in any plane. The construction of a fabric tensor from MIL requires an assumption that the material can be described by an elliptical distribution. Generalization of this fact to three dimensions shows that the mean intercept length, plotted as a radius from the origin at the angle of measurement, generates the surface of an ellipsoid of general formula

$$Ax_1^2 + Bx_2^2 + Cx_3^2 + 2Dx_1x_2 + 2Ex_1x_3 + 2Fx_2x_3 = 1 \qquad (2.21)$$

where A, B, C, D, E and F are constants. More specifically, if the mean intercept length L is plotted as a radius and related to cartesian coordinates by $x_i = Ln_i$, then

$$\frac{1}{L^2} = n_j H_{ij} n_i \qquad (2.22)$$

where

$$H = \begin{bmatrix} A & D & E \\ D & B & F \\ E & F & C \end{bmatrix}$$

and $\mathbf{n}$ is a unit vector in the direction of the mean intercept length measurement.
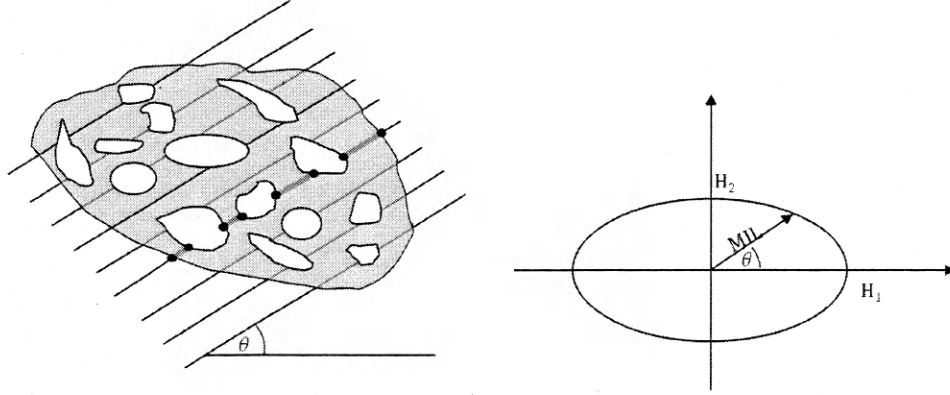
Figure 2.6: Mean Intercept Length Measurement in 2D.

As stated in [74], the mean intercept length is simply the average distance between two solid/void interfaces in a given direction and the distribution of the MIL forms an ellipsoid, and provides a second-rank fabric tensor $\mathbf{H}$. In porous materials, the fabric tensor $\mathbf{H}$ is a second-rank tensor used to describe the nature of the structural anisotropy. Cowin [7] defined a fabric tensor $\mathbf{M}$ to be the inverse square root of the mean intercept length tensor $\mathbf{H}$. Hence, the eigenvalues of the fabric tensor are the principal mean intercept lengths. Furthermore, there are three slightly different definitions of $\mathbf{H}$ encountered in the literature [3], [22], [77]: $\mathbf{H, M}$ and $\mathbf{G}$. All are related via

$$\mathbf{M} = \mathbf{H}^{-\frac{1}{2}} = v_s \mathbf{I} + \mathbf{G} \qquad (2.23)$$

20

where v_s is the solid volume fraction. Also, $\mathbf{M}$ must be normalized such that $\mathrm{Tr}\,\mathbf{M} = 3$ in order for certain constants appearing in the fabric tensor-stiffness tensor relationship to have physical meaning. Following Eq. (2.23), the eigenvalues m_i of the normalized fabric tensor $\mathbf{M}$ are related to the eigenvalues h_i of the fabric tensor $\mathbf{H}$ by

$$m_i = \frac{3}{\sqrt{h_i}}\,\frac{\sqrt{h_1 h_2 h_3}}{\sqrt{h_1 h_2}\,+\,\sqrt{h_1 h_3}\,+\,\sqrt{h_2 h_3}} \qquad (2.24)$$

2.3.2 Star Length Distribution (SLD)

In fabric tensor construction methods, the calculations are based on sums and numbers of lineal intercept lines which are usually equally spaced and are rotated from a standard alignment configuration into a prescribed sampling direction θ_i. Consider the following basic measurement quantities derived from an array of parallel test lines. Let $L(\theta_i)$ be the total length of test lines. Depending on the surface representation of the volume of interest, $L(\theta_i)$ may be constant. An intercept is an isolated line segment arising from the intersection of a test line with the boundary of the phase of interest and lying within this phase [33]. $SLD(\theta)$ is defined as the length L of an object (or set of objects) measured along a line ℓ with direction θ for a typical point within that (set of) object(s) [65],

$$SLD(\theta_i) = A(L_i(\theta_i)), \qquad 0 \leq \theta \leq 180^o \qquad (2.25)$$

where $A()$ denotes the mean value over uniform random positions of the point within the object(s). Using a line grid to define the intersections, see Figure 2.7, it can be shown that the expectation of a point being a part of intersection i is proportional to the length of that section L_i, whereas the total number of intersections n is proportional to the total length of the intersections, so that Eq. (2.25) can be written as

$$SLD(\theta_i) = \frac{\sum_{i=1}^{n} L^2(\theta_i)}{\sum_{i=1}^{n} L(\theta_i)}, \qquad 0 \leq \theta \leq 180^o \qquad (2.26)$$

where $SLD(\theta_i)$ is star length component, θ is semicircular orientation, n the number of intersections, and L is the fabric tensor. In this equation, the intercepts are weighted by their length.

Odgaard, et al. [53] also defined the SLD fabric tensor as the average length of an intercept with random orientation through a random point and stated that it is more sensitive to the detection of microstructural orientation than those involving MIL method. The algorithm of SLD for the two-dimensional case is illustrated in Figure 2.7. This figure shows that the SLD method estimates the length from a random point and shows a matrix of pixels (grey) representing the crossing of a vertical and a horizontal strut. A series of equally spaced grid lines is laid over the structure at an angle θ. The intersection i of a grid line with the matrix material has length L_i, which is related to the number of (quadratic) pixels in this intersection $npix_i$, the pixel size (or picture resolution) $dpix$, and the angle θ.

Note that effectively the longest projection of L_i on the coordinate axes is measured, and that the length is subsequently calculated by correcting for the angle. Obviously, the intersecting line may contain only one pixel in the direction of the projection, because otherwise L_i would be overestimated for most angles θ. There is no formal relationship between the SLD fabric tensor $\mathbf{L}$ and MIL fabric tensors, but all can be used for prediction of mechanical properties [53].

2.3.3 Star Volume Distribution (SVD)

Star volume distribution was originally proposed by Cruz-Orive, et al. [10] and is conceptually related to the volume orientation descriptor (VO) introduced by Odgaard, et al. [53]. This measure is similar to SLD with the exception that intercepts are weighted more heavily. A point grid algorithm for calculating SVD was recently presented in [53]. In SVD, a regularly spaced point grid is generated over the sampling domain. The subset of points that fall within the phase of interest is
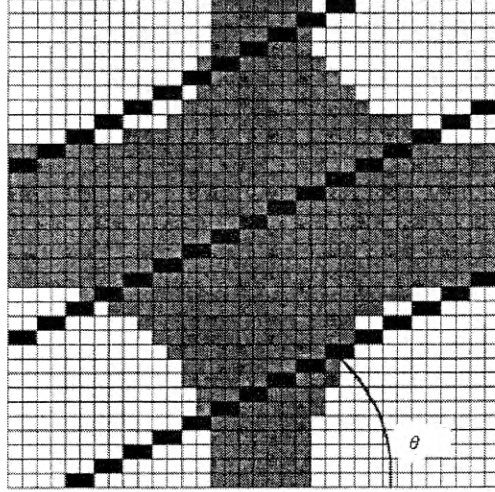
Figure 2.7: The procedure of the star length distribution (SLD). A grid of test lines (black) at an angle θ is placed on a porous solid specimen. For each pixel of these lines that lies within the solid volume, the solid length in the direction θ is determined. The solid length in this direction is averaged over all pixels to get $SLD(\theta)$ [65].

retained for scanning. For each member of a set of uniformly distributed orientations, a test line is generated at every sampling point and an intersection with the phase of interest is determined. Averaging the cubed intercept lengths over all of the points yields the mean volume as a function of orientation. In this case, the definition of SVD becomes

$$SVD(\theta_i) = \frac{\sum_{i=1}^{n} S^4(\theta_i)}{\sum_{i=1}^{n} S(\theta_i)}, \tag{2.27}$$

where $\mathrm{SVD}(\theta_i)$ is star volume component, θ is semicircular orientation, n the number of intersections, and S is the fabric tensor.

Star volume distribution SVD is the variation of the star volume component with orientation see Figure 2.8. The SVD fabric tensor $\mathbf{S}$ is calculated using the orientation matrix method (ellipsoid of inertia) with the modification that each direction is weight by its star volume component.

In general, the star volume distribution method (SVD) provides more detailed anisotropy information than the mean intercept length method [65]. To become

23
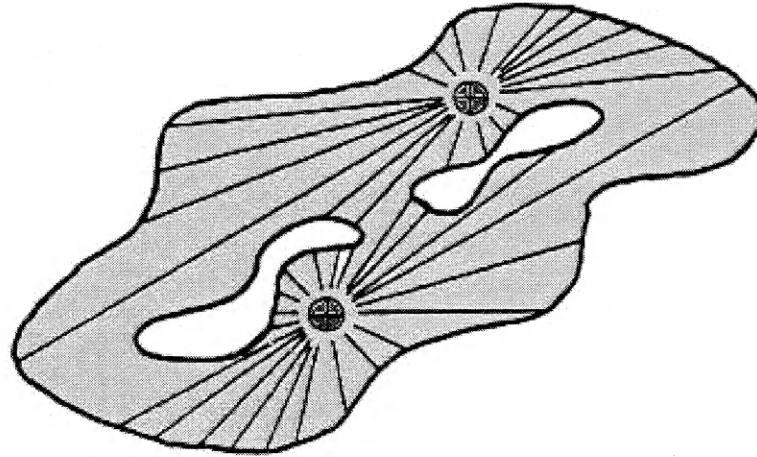
Figure 2.8: Star volume distribution: a point grid is laid on the structure. For each point within the structure, the intercept length through the point is determined in several directions [65].

suitable for prediction of mechanical properties the SVD is often approximated with a second order tensor. Authors in [52] and [53] stated that these approximations are good predictors of mechanical anisotropy.

MIL, SLD and SVD may all reveal the structural information that is necessary for a proper material characterization. All these methods are based on binary images and share a common drawback. The application of these methods to porous material micrographs requires image segmentation. Image segmentation is very delicate and often the most controversial step of image preprocessing. To circumvent this difficulty methods based on grayscale images can be used directly to quantify structural anisotropy. Several methods using different approaches have been proposed [52].

2.3.4 Quant3D Software

Quant3D is a versatile program that can be used to analyze material fabrics in any 2-D and 3-D data set. These analyses include quantification of anisotropy in

24

trabecular bone and textural analysis of metamorphic rocks [36]. Quant3D quantifies three-dimensional fabric tensors using a variety of metrics. As mentioned above, fabric tensors are produced based on the star volume distribution (SVD), star length distribution (SLD), and mean intercept length (MIL) methods. Principal component directions and magnitudes are provided for the tensors, providing the degree of anisotropy and shape indices of the phase of interest. Three-dimensional rose diagrams are a unique feature implemented in Quant3D for analyzing non-orthogonal directional fabric components.

Quant3D was developed at The University of Texas at Austin where a group of specialized software packages for quantitative analysis of High-Resolution X-ray Computed Tomography (HRXCT) data sets have been developed. All of the programs are written in Interactive Data Language (IDL). The user manual of the Quant3D is available on line [30] and examples of log files are attached in the appendix.

2.3.5 The Relationship Between Fabric Tensor and Elastic Constants

Relations between the stiffness and fabric tensors have been established using two different approaches [7] and [77]. Cowin [7] derived an elegant relationship between the fabric tensor and the elasticity stiffness tensor of a porous material. Cowin assumed the stress is an isotropic function of strain and fabric which lead to expressions for the orthotropic stiffness of the form

$$E_i = m_1 + m_2 II_H + m_3 H_i + m_4 H_i^2, \quad i = 1, 2, 3 \tag{2.28}$$

$$G_{ij} = m_5 + m_6 II_H + m_7(H_i + H_j) + m_8(H_i^2 + H_j^2) \quad i, j = 1, 2, 3, i \neq j \tag{2.29}$$

where E_i are the orthotropic Young's moduli, G_{ij} are the orthotropic shear moduli, the m_i are 8 unknown functions of the structural density ρ and H_i are the eigenvalues of the fabric tensor, and II_H is the second invariant of the fabric tensor, $II_H =$

$H_1H_2 + H_1H_3 + H_2H_3$. These expressions in Cowin's approach have large number of parameters to be determined. Also the compliance to stiffness tensors invertibility and positive definiteness of strain energy are not guaranteed.

An alternative approach was presented by Zysset and Curnier [77] to predict the relationship of elastic stiffness with the volume fraction. Based on a scalar and a symmetric, traceless second rank fabric tensor, Zysset and Curnier [77] derived the relations between the orthotropic elastic stiffness constants and the fabric tensor. This was accomplished using a Fourier expansion in spherical harmonics of the orientation distribution function of a positive random symmetric microstructural property. In addition to linear elasticity, the model can also be applied to the construction of anisotropic yield criteria based on a fourth order tensor, such as Hill's criterion. Strict positive definiteness of the corresponding elasticity tensor is guaranteed under explicit conditions on the independent constants for arbitrary fabric tensors. Thus, the model gives the orthotropic engineering constants as

$$E_i = E_0 v_s^k z_i^{2\ell}, \qquad (2.30)$$
$$\nu_{ij} = \nu_0 \left(\frac{z_j}{z_i} \right)^\ell,$$
$$G_{ij} = G_0 v_s^k z_i^\ell z_j^\ell$$

where ℓ, k are constants and E_0, ν_0 and G_0 can be interpreted as the Young's modulus, the Poisson ratio, and the shear modulus of the matrix material ($v_s = 1$) provided the fabric tensor is properly normalized. Note in Eqs.(2.30) that the Poisson ratio is independent of v_s. This is supported by many experimental studies included in [3]. Eqs. (2.30) were used in [3] in the context of boundary element analysis to predict the effect of solid volume fraction on principal stresses in anisotropic bimaterials.

It is interesting to note that Eqs.(2.30) can not, strictly speaking, be applied in the limit as the solid volume fraction approaches 1 (or, equivalently, the porosity approaches zero). One critical assumption in the development of Eqs.(2.30) is that

the fabric tensor remains constant over all values of solid volume fraction. Roughly speaking, this means that the structure of the voids, or in the case of bone the trabecular architecture, remains constant as the solid volume fraction changes. This assumption is, of course, violated when the solid volume fraction approaches 1 because the eigenvalues of the fabric tensor must all equal one as there are no voids.

CHAPTER 3

BOUNDARY ELEMENT METHOD

In numerical modeling, the Boundary Element Method (BEM) is an attractive option to solve many engineering problems. BEM has been classified as a modern numerical technique for solving complex partial differential equations [5]. The BEM is based upon transforming the differential equation into an integral equation and numerically approximating the solution of this boundary integral equation [4]. The mathematical foundations of the boundary element method are the theorems of Gauss, Stokes and Green which reduce the volume differential equation to a boundary integral equation. Recently, BEM has been widely used by researchers leading to the development of many commercial and private codes.

The boundary element method has been found to be useful in numerous engineering fields, including elasticity, geomechanics, structural mechanics, electromagnetics, acoustics, hydraulics, low-Reynolds number hydrodynamics, biomechanics, off-shore structures, and cathodic protection [72]. The BEM offers the advantage of replacing a given problem with another one in a spatial dimension reduced by one. In three dimensional problems, only the boundary surface is discretized, whereas in two dimensional problems, only the domain boundaries are discretized as shown in Figure 3.1.

A wide variety of algorithms have been employed to numerically approximate the solution of the boundary integral equation, and this dissertation focuses on one particular method, the Symmetric-Galerkin Boundary Element Method (SGBEM) and its application to porous materials. The formulation of the SGBEM for elasticity problems will be reviewed and considered in this chapter. Many journal papers and texts have been written that provide additional details on Symmetric-Galerkin Boundary Element Method (SGBEM) for instance Gray et al. [67], Sirtori et al. [46]

and Aliabadi [1].
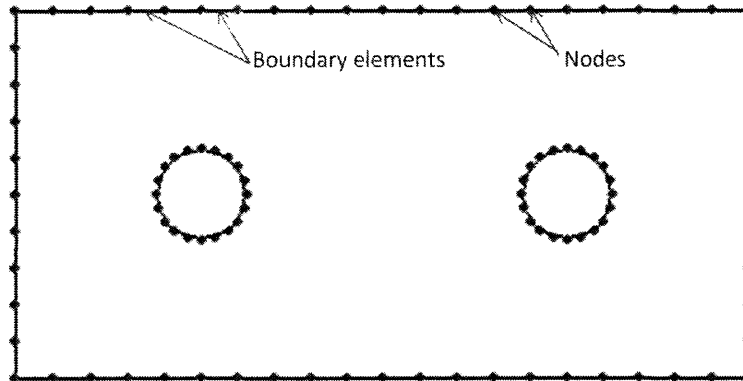
Figure 3.1: BEM discretization [6].

Advantages of the Boundary Element Method (BEM)

Here we summarize the main advantages of using the boundary element method.

1. Reduction of problem dimension by 1.

   In BEM modeling, there is less data preparation time, and easier to to apply changes to the applied mesh. BEM is very useful for problems that require meshing such as crack extension problems.

2. High accuracy.

   Stresses and strains result from BEM analysis are highly accurate as there are no approximations imposed on the solution in interior domain points. Also, this method is suitable for modeling problems with rapidly changing stresses.

3. Less computer time and storage.

   In comparison with other numerical methods, BEM has a high accuracy level using less number of nodes and elements which means less computational time and memory storage.

4. Filter out unwanted information.

   The solution at internal points of the domain is optional in BEM, so the focus

can be only on a particular internal region, which filters out all unwanted data and reduces computer time and effort.

The early work of Rizzo [59] and Cruse [9] provided the formulation of BEM based on an integral statement of elasticity, and this can be cast into a relation involving unknowns only over the boundary of the domain under study. This process generates an algebraic system of equations to solve for the unknown nodal values that approximate the boundary solution. This system allows variation in element size, shape and approximating scheme to suit the application. The main advantage of the BEM is its unique ability to provide a complete solution in terms of boundary values only, with substantial savings time and efforts. Another advantage is that the resulting BEM equations system is generally much smaller than that generated by finite difference and finite element methods [4].

3.1 The Green's Function (GF)

In the boundary element method, the Green's function is the fundamental solution to the governing differential equation and is critical in order to reduce the partial differential equation to a boundary integral equation (BIE) [49]. In many cases, Green's function can be used to construct useful solutions, and it is frequently used in numerical methods formulation as a basic ingredient for solving potential and elasticity problems [58]. The exact form of the Green's function depends on the differential equation, the shape of the domain under study, and the type of boundary conditions applied. Green's functions are named in honor of English mathematician and physicist George Green (1793-1841).

Lord Kelvin in the 19th century obtained the Green's function for a three-dimensional homogeneous, isotropic, elastic solid. This solution gives the displacement at a point q when a point force is acting at another point p. We review Green's functions for both potential and elasticity problems in the following sections.

30

3.1.1 The Green's Function in Potential Problems

In potential theory, we are looking to find a solution for Laplace's equation. The fundamental solution or the "free space" Green's function is simply given in 2D as

$$G(P, Q) = \frac{1}{2\pi} \log\left(\frac{1}{r}\right),$$ (3.1)

where

$$\nabla^2 G(P, Q) = -\delta(P, Q),$$ (3.2)

and P and Q are called the source point and the field point, respectively, and $\delta(P, Q)$ is Dirac delta function, and r is the distance between points Q and P,

$$r = |Q - P| = \sqrt{(x_Q - x_P)^2 + (y_Q - y_P)^2 + (z_Q - z_P)^2}.$$

The corresponding normal derivatives are given by

$$\frac{\partial G}{\partial n}(P, Q) = -\frac{1}{2\pi} \frac{n \cdot R}{r^2}$$ (3.3)

$$\frac{\partial^2 G}{\partial N \partial n}(P, Q) = -\frac{1}{2\pi} \left[-\frac{N \cdot n}{r^2} + 2\frac{(n \cdot R)(N \cdot R)}{r^4} \right],$$ (3.4)

where $R = Q - P$ is the unnormalized tangent vector, see Figure 3.2, $N = N(P)$ is the unit outward normal at P, ∂N indicates a derivative with respect to the coordinates of P, and $n = n(Q)$ is the unit outward normal at Q. The Green's function in three dimensions is

$$G(P, Q) = \frac{1}{4\pi r},$$ (3.5)

and the corresponding normal derivatives are

$$\frac{\partial G}{\partial n}(P, Q) = -\frac{1}{4\pi} \frac{n \cdot R}{r^3}$$ (3.6)

$$\frac{\partial G}{\partial N}(P, Q) = \frac{1}{4\pi} \frac{n \cdot R}{r^3}$$ (3.7)

31

$$\frac{\partial^2 G}{\partial N \partial n}(P, Q) = \frac{1}{4\pi} \left[\frac{N \cdot n}{r^3} - 3\frac{(n \cdot R)(N \cdot R)}{r^5} \right], \qquad (3.8)$$
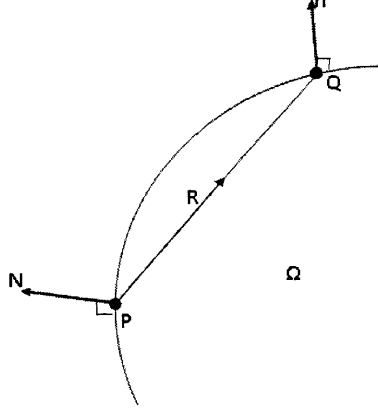
Figure 3.2: Field and source points (P,Q) and vector R.

A derivation of Eq.(3.1) and Eq.(3.5) is given in [67], where the Green's function is defined as physically corresponding to the electrostatic potential at the field point Q given a point charge at P, see Figure 3.3. Thus, $G(P, Q)$ is also called the "point source potential", and for each fixed P, it satisfies the Laplace equation as a function of Q for $Q \neq P$. When $r \to 0$ or $P = Q$, there is a singularity in the 3D Green's function Eq.(3.5) which behaves as r^{-1}, worse than the $\log(1/r)$ for 2D case, Eq.(3.1).

Application of Green's second identity to Laplace's equation $\nabla^2 \phi = 0$, transforms the partial differential equation (PDE) to a boundary integral equation (BIE) as

$$C(P)\phi(P) = \int_{\Gamma} [G(P, Q)q(P) - H(P, Q)\phi(Q)]\, d\Gamma \qquad (3.9)$$

where Γ is the boundary of the domain Ω, $q = \frac{\partial \phi}{\partial n}$, $\quad H = \frac{\partial G(P,Q)}{\partial n}$, and

$$C(P) = \begin{cases} 1 & P \in \Omega \\ 1/2 & P \in \Gamma, \quad \Gamma \quad \text{is smooth} \\ (1 - \frac{\alpha}{2\pi}) & P \in \Gamma, \quad \Gamma \text{ is not smooth} \\ 0 & P \notin \Omega. \end{cases} \qquad (3.10)$$

where α is the interior angle of the corner at P.

$$G(P,Q) = \frac{1}{4\pi r}$$
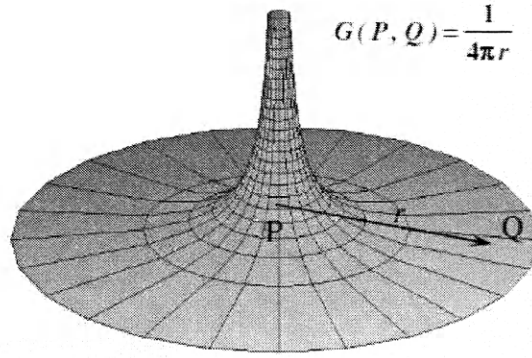
Figure 3.3: 3D Green's function G(P,Q) [67].

After discretizing the BIE and introducing approximations for ϕ and q we obtain the following BEM matrix equation:

$$[G]\{\phi\} = [H]\{q\} \qquad (3.11)$$

where H and G are two N $\times$ N matrices containing the integrals of the BIE kernels, approximations functions, and Jacobians, and q, ϕ are vectors of boundary values.

So far, we have calculated the coefficients of the $[H]$ and $[G]$ matrices noting that some values of vectors ϕ and q are known but the problem is not unique until applying the boundary conditions. All nodal points must have a prescribed boundary condition of either ϕ or q. After applying the boundary conditions we can rearrange Eq.(3.11) to obtain the linear system:

$$[A]\{x\} = \{b\} \qquad\qquad (3.12)$$

where x is a vector of the unknown values of ϕ and q at the nodes, b is found by multiplying the elements of H or G by the known values of ϕ and q on the boundaries, hence there are only N unknowns in this system of equations.

Eq.(3.12) can be solved in a variety of ways, such as Gauss elimination. Upon the solution of the linear system, we have the values of ϕ and q at any point on the boundary. Also it is possible to calculate any internal value of ϕ or q at any internal point inside the domain Ω via Eq.(3.9).

3.1.2 The Green's Function in Elasticity Problems

The three-dimensional isotropic elasticity equations, derived from Newton's law, state that the divergence of the stress tensor is zero. Thus, the equilibrium equations in the absence of body forces are

$$\nabla \cdot \sigma = \sigma_{ij,j} = 0, \qquad (i, j = 1, 2, 3). \qquad (3.13)$$

In this case the stress and strain tensors are defined for an isotropic solid as

$$\sigma_{ij} = 2\mu\varepsilon_{ij} + \lambda\varepsilon_{kk}\delta_{ij}, \qquad\qquad (3.14)$$
$$\varepsilon_{ij} = \frac{1}{2}(u_{i,j} + u_{j,i}),$$

where δ_{ij} is the Kronecker delta, μ is the shear modulus, λ is the Lamé's modulus, and u_i is the displacement vector. Here the summation convention is employed and a subscript after the comma denotes partial differentiation with respect to that coordinate. Combining Eq.(3.13) and Eq.(3.14) we obtain the Navier-Cauchy equation for equilibrium in terms of displacements,

$$\mu u_{k,jj}(x) + (\lambda + \mu)u_{j,jk} = 0 \qquad (j, k = 1, 2, 3), \qquad (3.15)$$

34

One way to derive the fundamental solution for Navier-Cauchy equation is through the use of the Galerkin vector, g_i where

$$\nabla^2(\nabla^2 g_i) = 0. \tag{3.16}$$

The Galerkin vector is a general displacement potential for an elastic isotropic body and is also Love's strain function [18]. The Galerkin vector approach is commonly used to evaluate the fundamental solution due to a unit point load in infinite elastic medium (Kelvin's solution). The displacements are expressed in terms of Galerkin vector as [1]

$$2\mu u_i = 2(1 - \nu)g_{i,jj} - g_{i,ji}. \tag{3.17}$$

Note if we know the Galerkin vector g, then we can calculate ε_{ij} and σ_{ij} using the strain-displacement relation, and Hooke's law, Eq. (3.14). The Galerkin vector for three and two dimensions given respectively by

$$g_i = \frac{1}{8\pi\mu} r e_i, \tag{3.18}$$

$$g_i = \frac{1}{8\pi\mu} r^2 \log(r) e_i \tag{3.19}$$

where e_i is a unit vector.

The BEM formulation for linear elasticity can be derived using several methods and approaches. S. Li et al. [43] give a detailed derivation using the Maxwell-Betti theorem. This reciprocal theorem is a statement of equivalence of virtual work and states that: if an object subjected to two load cases, A and B, two equilibrium states result, u_i, U_i, with body forces b_i, b_i^*, and surface tractions t_i, T_i. The divergence theorem and the equilibrium equations then lead to the reciprocal theorem,

$$\int_\Gamma T_i u_i d\Gamma + \int_V b_i^* u_i \, dV = \int_\Gamma U_i t_i \, d\Gamma + \int_V U_i b_i \, dV. \tag{3.20}$$

The traction terms are only considered on the surface and the body forces are con-

sidered through the volume. The point force can be expressed as a body force with the Dirac delta function, $b_i^* = \delta(P - Q)e_i$. We also take T_i and U_i to be the Kelvin fundamental solution. Assuming the body forces in the physical case, b_i, to be zero, we then obtain

$$u_i(P) = \int_\Gamma U_{ki}(P, Q)t_i(Q) \; d\Gamma - \int_\Gamma T_{ki}(P, Q)u_i \; d\Gamma, \qquad (3.21)$$

where $u_i(P)$ is the displacement in the physical case at point P see Figure 3.4. The key in BEM is both volume integrals have been removed from this equation, which gives the method some advantages over FEM [6]. The Kelvin kernels are given in two dimensions by

$$U_{ki} = \frac{1}{8\pi\mu(1 - \nu)}[(3 - 4\nu)\log(1/r)\delta_{kj} + r_{,k}r_{,j}], \qquad (3.22)$$

where $r_{,i} = \partial r/\partial x_i$ and

$$T_{ki} = \frac{-1}{4\pi(1 - \nu)r}\frac{\partial r}{\partial n}\left[(1 - 2\nu)\delta_{kj} + 2r_{,k}r_{,j}\right] + \frac{1 - 2\nu}{4\pi(1 - \nu)r}(n_k r_{,j} - n_j r_{,k}). \qquad (3.23)$$

Now consider Eq. (3.21) when the point P is taken to the boundary. In taking P to the boundary, we introduce a multiplier $C(P)$, obtained from a limiting process of the integrals, where $C(P)$ takes the value of one half if P is on a smooth boundary, see Eq.(3.10). We now have the final form of the Boundary Integral Equation (BIE),

$$c_{ki}u_i + \int_\Gamma T_{ki}u_i \; d\Gamma = \int_\Gamma U_{ki}t_i \; d\Gamma. \qquad (3.24)$$

This boundary integral equation is the key equation in the BEM formulation and it's clear that the reciprocal nature of the displacements and tractions lies within this equation.

To integrate Eq. 3.24 we first discretize the boundary as

$$c_{ki}u_i + \sum_{n_j=1}^{N} \int_{\Gamma_n} T_{ki}u_i \; d\Gamma_n = \sum_{n_j=1}^{N} \int_{\Gamma_n} U_{ki}t_i \; d\Gamma_n \qquad (3.25)$$

36
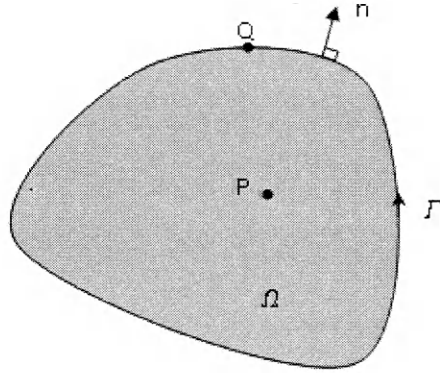
Figure 3.4: Solid domain with field and source points (P,Q).

As mentioned earlier, the terms U_{ki} and T_{ki} can be easily calculated for any pair of points, but it is not trivial to integrate these functions over the boundary element Γ_n, analytically. Numerical integration (trapezoidal, Simpson's rules and Gauss-Legendre quadrature) is usually used. Gauss-Legendre quadrature is typically used in most BEM programs for integrations when P and Q are not on the same element.

The singularities of the fundamental solutions requires careful analysis when the load point is accommodated on the boundary, or when P and Q are on the same element. In this case we surround P with a small circle of radius ε and then examine the solution as $\varepsilon \to 0$ which results new boundaries $\Gamma + \Gamma_\varepsilon$. We will discuss singular and hypersingular integrals in subsequent sections.

Approximations for u_i and t_i are now introduced. Similar to FEM, the nodes are discrete points at which the values of displacement and traction will be interpolated from. The displacement and traction at any other point on the element can then be found by interpolating from the nodes. This is done through the use of shape functions, which in the case of a quadratic continuous element, shown in Figure 3.5, will have a set of shape functions, in the local coordinate ξ, $\quad -1 \le \xi \le 1$, as

$$N_1(\xi) = \frac{1}{2}\xi(\xi - 1) \tag{3.26}$$

$$N_2(\xi) = (1 - \xi)(1 + \xi)$$

$$N_3(\xi) = \frac{1}{2}\xi(\xi + 1)$$
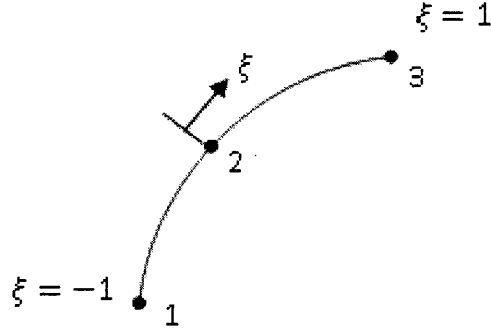
Figure 3.5: Quadratic continuous element with 3 nodes.

The displacement, u_i, at any point on the element can then be found by interpolation as

$$u_i(\xi_j) = \sum_{j=1}^{3} N_j u_i(\xi_j), \tag{3.27}$$

where $u_i(\xi_j)$ is the nodal displacement u_i at node ξ_j. Similarly the traction, t_i, at any point at any element is

$$t_i(\xi_j) = \sum_{j=1}^{3} N_j t_i(\xi_j). \tag{3.28}$$

We now replace the displacement, u_i, and traction, t_i, in equation Eq.(3.29) by the interpolated forms Eq.(3.27) and Eq.(3.28). We then have

$$C_{ki}u_i(P) + \sum_{n=1}^{N}\int_{-1}^{1} T_{ki}\sum_{n=1}^{3} N_j u_i(\xi_j)J\, d\xi = \sum_{n=1}^{N}\int_{-1}^{1} U_{ki}\sum_{n=1}^{3} N_j t(\xi_j)_i J\, d\xi, \tag{3.29}$$

where J is the Jacobian of the transformation from x_i to ξ_i. Eq. (3.29) can next be written as

$$C_{ki}u_i(P) + \sum_{n=1}^{N}\left\{\sum_{j=1}^{3} U_i^n(\xi_j) \int_{-1}^{1} T_{ki}N_j J \ d\xi\right\} = \sum_{n=1}^{N}\left\{\sum_{j=1}^{3} t_i^n(\xi_j) \int_{-1}^{1} U_{ki}N_j J \ d\xi\right\}.$$

(3.30)

For any position P, can be evaluated as products of fundamental solutions, shape functions, and Jacobians.

Writing Eq. (3.30) for each choice of $P_i \quad i = 1, 2, \ldots .3N$ nodal points we then have

$$\mathbf{Hu} = \mathbf{Gt},$$

(3.31)

where $\mathbf{H}$ and $\mathbf{G}$ are $3N \times 3N$ square matrices, and the vectors $\mathbf{u}$ and $\mathbf{t}$ contain either known or unknown nodal values of displacement and traction.

For a well posed problem, $3N$ of the $6N$ nodal values of displacement and traction will be prescribed. Eq. (3.31) therefore represents $3N$ unknown nodal values.

The last step in solving the problem is to rearrange Eq. (3.31) to bring all the unknowns to the left hand side, and taking all the terms specified as boundary conditions to the right hand side. We then obtain the linear system

$$\mathbf{Ax} = \mathbf{b}.$$

(3.32)

The unknown vector $\mathbf{x}$ can be found by any linear system solver such as Gauss elimination. The vector $\mathbf{x}$ contains all the unknown nodal values of displacement and traction on the boundary. After solving for the unknown boundary values, the displacement at any internal point may be computed directly from the discretized form of Eq. (3.21).

3.2 Singular and Hypersingular Integrals

As previously mentioned, Green's functions are divergent when the source and field points coincide, $P = Q$, and the singularity appears. This singularity becomes progressively stronger with higher derivatives, and thus the evaluation of singular and hypersingular integrals is critical. There are many techniques available in the literature for defining and computing singular integrals [55]. To discuss this subject, consider the BIE previously introduced,

$$w_i(P) = u_i(P) + \int_\Gamma [T_{ij}(P,Q)u_j(Q) - U_{ij}(P,Q)t_j(Q)]d\Gamma_Q. \tag{3.33}$$

where w_i is the displacement kernel.

Eq.(3.33) provides an equation for displacement when P is either interior or exterior to the domain, but the essential case $P \in \Gamma$ needs more examination and discussion. The solution when P is located on the boundary cannot be trivial, as this must produce singular integrals. To solve this, Gray et al. [67] adopted an elegant approach solving singular and hypersingular integrals. They defined the boundary equation as a limit as P approaches the boundary, of either the interior or exterior equation; it will turn out that the two limits of Eq.(3.33) result in the same boundary equation. The singular integrals are therefore defined in terms of this limit, and while this definition is physically reasonable and intuitively simple, they found out that it is necessary to establish that the limits exist, and moreover that they can be readily computed.

One motivation for adopting the boundary limit is that, in addition to Eq.(3.33), it is also necessary to be able to handle the corresponding equation for its normal derivative,

$$\Sigma_{ij}^I(P) \equiv \sigma_{lk}(P) + \int_\Gamma [S_{lkm}(P,Q)u_m(Q) - D_{lkm}(P,Q)t_m(Q)]dQ \tag{3.34}$$

$$\Sigma_{ij}^E(P) \equiv \int_\Gamma [S_{lkm}(P,Q)u_m(Q) - D_{lkm}(P,Q)t_m(Q)]dQ, \qquad (3.35)$$

where Σ_{ij}^I and Σ_{ij}^E are interior and exterior stress equations, respectively. The kernels $D_{lkm}(P,Q)$ (singular) and $S_{lkm}(P,Q)$ (hypersingular) result from differentiating U_{kj} and T_{kj}.

Note that these equations are obtained by differentiating Eq.(3.33), and then interchanging the derivative with the integral. This interchange is allowed if P is off the boundary due to the symmetry properties of the Green's function, thus interior and exterior equations are mathematically appropriate. In the symmetric-Galerkin boundary element method, and to achieve symmetric matrices, treating the singularity in Eq.(3.33) is necessary . In addition to the equation for surface stress, Eq.(3.35), it is important for many applications to be able to calculate any directional derivative. A second key advantage of a boundary limit definition in elasticity is that combining interior and exterior equations will lead to a highly effective algorithm for computing the surface gradient, either flux $\nabla\phi$ or surface stress [67].

3.3 Numerical Solutions: Collocation and Galerkin

Determining analytical solutions for the integral equations is not usually possible. Hence, it is necessary to reduce the continuous equations to a discrete system of linear equations that can be easily solved [73]. This approach was discussed previously in this chapter. In addition to the collocation approach previously described, Galerkin approach, can also be used to reduce the continuous integral equations, Eq.(3.33) and Eq.(3.35), to a finite system. Collocation is a simple procedure, where the boundary integral equations are explicitly enforced at a finite set of points. These collocation points are chosen to be the nodes used to discretize the boundary of the domain. Thus, a collocation approximation of Eq.(3.33) can be simply stated as

41

$$w_i(P_k) = 0, \qquad\qquad (3.36)$$

where P_k, $1 \leq k \leq M$ are the selected boundary points. If the boundary displacement and traction are interpolated from their values at these M points, $u_i(P_k)$ and $t_i(P_k)$, then the boundary conditions usually provide M of these $2M$ numbers. The point-wise enforcement of Eq.(3.33) in Eq.(3.36) then provides the M equations needed to solve for the unknown values. When applying the collocation approach, the resulting matrices are non-symmetric [67].

In addition to collocation, the Galerkin approach is also frequently used in the solution of integral equations. The Galerkin method does not require that the integral equations be satisfied at any point [48], but the equations are enforced in a weighted average way,

$$\int_\Sigma \psi_k(P) w_i(P_k) = 0, \qquad\qquad (3.37)$$

$$\int_\Sigma \psi_k(P) \Sigma(P_k) = 0, \qquad\qquad (3.38)$$

where $\psi_k(P)$ are the chosen weight functions. Same typical choices for weight functions are shown in Figure 3.6. The M equations needed can be generated by an appropriate choice of M weights. The strict definition of Galerkin is that the weight function $\psi_k(P)$ is composed of the shape functions that are nonzero at the node P_k, the shape functions being the local basis functions used to interpolate the boundary functions.

Mathematically, in the collocation method, the equations are satisfied at speci-fied points. The collocation solution is therefore called a "strong" solution, whereas Galerkin in mathematical terminology, is called a "weak" solution [8]. The require-ment that the equations hold in integrated sense has a geometric interpretation: the approximate Galerkin solution is obtained by projecting the exact solution onto the

subspace consisting of all functions which are a linear combination of the shape functions [43].
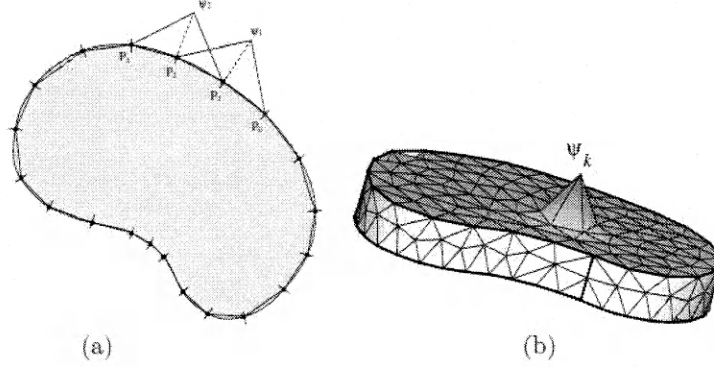
Figure 3.6: Galerkin weight functions for 2D and 3D BEM [67].

Gray, et al. [67] stated that the Galerkin method provides a nicer treatment of boundary corners and is more accurate than collocation. However, the primary advantage of Galerkin is that the treatment of singular and hypersingular integrals is much more accurate and simpler than the collocation method [73, 5].

The stress BIE is needed in symmetric Galerkin boundary element method. The interior and exterior stress equations are obtained by differentiating the displacement Eq. (3.33), with respect to P,

$$\Sigma_{ij}^{I}(P) \equiv \sigma_{lk}(P) + \int_{\Gamma}[S_{lkm}(P,Q)u_m(Q) - D_{lkm}(P,Q)t_m(Q)]dQ = 0 \qquad (3.39)$$

$$\Sigma_{ij}^{E}(P) \equiv \int_{\Gamma}[S_{lkm}(P,Q)u_m(Q) - D_{lkm}(P,Q)t_m(Q)]dQ = 0, \qquad (3.40)$$

where Σ_{ij}^{I} and Σ_{ij}^{E} are interior and exterior stress equations, respectively. The kernels $D_{lkm}(P,Q)$ (singular) and $S_{lkm}(P,Q)$ (hypersingular) for the stress equation result from differentiating U_{kj} and T_{kj} Eq. (3.22) and Eq. (3.23), and are given by [59]

$$D_{kjl} = \frac{1}{4\pi(1-\nu)r}\left[(1-2\nu)(\delta_{kj}r_{,l} + \delta_{jl}r_{,k} - \delta_{lk}r_{,j}) + 2r_{,k}r_{,j}r_{,l}\right] \qquad (3.41)$$

43

$$S_{kjl} = \frac{G}{2\pi(1-\nu)r^2}\left[2\frac{\partial r}{\partial n}\{(1-2\nu)(\delta_{lk}r_{,j} + \nu\delta_{kj}r_{,l} + \delta_{jl}r_{,k}) + 4r_{,k}r_{,j}r_{,l}\}\right. \quad (3.42)$$
$$+2\nu(n_k r_{,j}r_{,l} + n_l r_{,k}r_{,j}) + (1-2\nu)(2n_j r_{,l}r_{,k} + \delta_{kj}n_l + \delta_{jl}n_k)$$
$$\left. -(1-4\nu)\delta_{lk}n_j\right].$$

Although the Kelvin solution and its derivatives are lengthy expressions, they are still rational algebraic expressions and the singular integration methods developed for the simpler Laplace problem will carry over directly to elasticity. The important point is that the order of the singularities at $r = 0$ is precisely the same for elasticity and the Laplace differential equations [67].

3.4 Symmetric Galerkin Boundary Element Method (SGBEM)

For several reasons, the symmetric Galerkin boundary element method has became more significant in the field of BEM for the solution of elastostatics problems [63]. For instance, the internal points can be evaluated more accurately near the domain boundaries, as compared to the collocation method. The ability to use standard continuous elements even for hypersingular equations where the collocation method requires discontinuous elements to ensure continuity is another important aspect of the method [55]. Finally, in SGBEM there is no need for special treatment of corners since there are enough equations at hand to deal with the discontinuity of the tractions over non-smooth boundaries.

The basic SGBEM framework for two dimensional elastic boundary value problems is introduced in this section. For a number of applications the integral equation for surface displacement is enough, but the symmetric Galerkin boundary element method employed also uses the stress BIE given by Eq. (3.40). The boundary integral equations for stresses and displacement used in the SGBEM are repeated here as

$$w_i(P) = u_i(P) + \int_\Gamma [T_{ij}(P,Q)u_j(Q) - U_{ij}(P,Q)t_j(Q)]d\Gamma_Q = 0, \qquad (3.43)$$

$$\Sigma_{ij}(P) = \sigma_{ij}(P) + \int_\Gamma [S_{ijk}(P,Q)u_k(Q - D_{ijk}(P,Q)t_k(Q)]d\Gamma_Q = 0. \qquad (3.44)$$

Note that as the fundamental solution tensors U_{ij} and T_{ij} are singular at $Q = P$, behaving as $\log(r)$ and r^{-1}, for the two dimensions respectively, for $r \to 0$. Moving the differentiation with respect to P under the boundary integral is permissible only if P is off the boundary. Thus, in the calculations reported herein, the singular integration algorithm is based upon the fact that Eq.(3.43) and Eq.(3.44) are only defined for P off the boundary: the singular integrals are computed for P near the boundary, and the limit as P approaches the boundary is then evaluated [18, 19]. Note that the singularity in S_{ijk} is of the form r^{-2}: a primary reason for employing the Galerkin approximation is to have an effective means of treating this higher order (hypersingular) singular kernel.

It should also be mentioned that the boundary limit procedure is not the only successful singular integration method, many procedures have been proposed in the literature. In particular, one can write the stress equation without moving the P derivative under the integral sign, and within the Galerkin formulation an integration by parts can be carried out. This procedure results in kernel functions that are only weakly singular, and these integrals can be readily computed [16, 43].

We will use the three-noded quadratic elements presented previously but with a slightly different interpolation. Employing the parameter space $t \in [0,\ 1]$, and defining $t_1 = 0$, $t_2 = 1/2$ and $t_3 = 1$, the shape functions are defined as

$$\begin{aligned}
\psi_1(t) &= (1-t)(1-2t), \\
\psi_2(t) &= 4t(1-t), \\
\psi_3(t) &= t(2t-1).
\end{aligned} \qquad (3.45)$$

The approximate representations of the boundary and boundary functions are then given by

$$\alpha_i = \sum_{\ell=1}^{3} \psi_\ell(t)\, \alpha_i^\ell \qquad (3.46)$$

where α_i can be u_i, t_i, x_i, or y_i, and α_i^ℓ is the nodal value of α_i.

Having defined the shape functions, a Galerkin approximation of the integral equations can be discussed. In this approximation, the displacement and traction integral equations are enforced 'on average', in the form

$$\int_\Gamma \hat{\psi}_\ell(P)\, w_i(P) d\Gamma_P = 0, \qquad (3.47)$$

$$\int_\Gamma \hat{\psi}_\ell(P)\, \Sigma_{ij}(P) n_j(P) d\Gamma_P = 0,$$

where $n_j(P)$ is the component of the local normal vector at P. Note that the Galerkin approach to solving the integral equations is different than collocation methods where the equations must hold at selected points, *i.e.*, $w_i(P_k) = 0$ and $\Sigma_{ij}(P_k)n_j(P_k) = 0$. Finally, the weight function $\hat{\psi}_\ell(P)$ is comprised of all shape functions that are equal to one at the node P_ℓ, and thus there are sufficient equations to solve for the boundary unknowns.

The symmetric-Galerkin formulation was first considered by Sirtori [64] and Hartmann et al. [23], and then extensively developed by Maier and co-workers [48, 46, 47, 63]. Note that in the Galerkin approach the source and field points P and Q are treated equally, and the kernels U_{ij} and $S_{ijk}n_j$ are themselves symmetric, *e.g.*

$$U_{kj}(Q,P) = U_{jk}(P,Q)\, . \qquad (3.48)$$

Thus, if displacement is specified everywhere on the boundary, the displacement equation Eq.(3.47), leads to a symmetric system of equations for the unknown tractions. Similarly the traction equation yields a symmetric matrix if the boundary data is entirely known tractions. In general, if the displacement equation is employed on the

part of the boundary where displacement is specified, while the traction equation is employed on the part of the boundary where traction is known, then the resulting linear equations are symmetric. This follows from the additional observation that T_{ij} and D_{ijk} are related through the first order derivatives of U_{ij}. The key task in the numerical implementation of Eq.(3.47) is the evaluation of the singular integrals, and an advantage of the Galerkin approach is that the extra boundary integration makes defining and computing the hypersingular S_{ijk} kernel integral significantly easier. In this work, the singular integration (for all kernels) is accomplished by means of direct hybrid analytical/numerical algorithms that result from defining the integrals as a limit to the boundary [19], [67]. In this approach, one sees that the individual, *i.e.* coincident and adjacent element, hypersingular integrals are divergent. However, the divergent terms that show up in the limit process can be shown to cancel, and the complete integral is finite.

The additional boundary integration is the key to obtaining a symmetric coefficient matrix, as this ensures that the source point P and field point Q are treated in the same manner in evaluating the kernel tensors U_{kj}, T_{kj}, D_{kjl} and S_{kjl}. After discretization, the resulting equation system can be written in block-matrix form [67] as:

$$\begin{bmatrix} H_{11} & H_{12} \\ H_{21} & H_{22} \end{bmatrix} \begin{Bmatrix} u_{bv} \\ u_* \end{Bmatrix} = \begin{bmatrix} G_{11} & G_{12} \\ G_{21} & G_{22} \end{bmatrix} \begin{Bmatrix} t_* \\ t_{bv} \end{Bmatrix} \tag{3.49}$$

where u_* and t_* are unknown displacement and traction vectors, respectively and $\Gamma_{b(u)}$ is the portion of the boundary Γ_b with prescribed displacement and $\Gamma_{b(t)}$ is the portion with prescribed traction, see Figure 3.7.

Here, the first and second rows represent, respectively, the BIE written on $\Gamma_{b(u)}$ and the HBIE written on $\Gamma_{b(t)}$. Further, rearranging Eq.(3.49) into the form $[A]\{x\} = \{b\}$, and multiplying the HBIE by one, obtains

$$\begin{bmatrix} -G_{11} & H_{12} \\ G_{21} & H_{22} \end{bmatrix} \begin{Bmatrix} t_* \\ u_* \end{Bmatrix} = \begin{Bmatrix} -H_{11}u_{bv} + G_{12}t_{bv} \\ H_{21}u_{bv} - G_{22}t_{bv} \end{Bmatrix} \qquad (3.50)$$
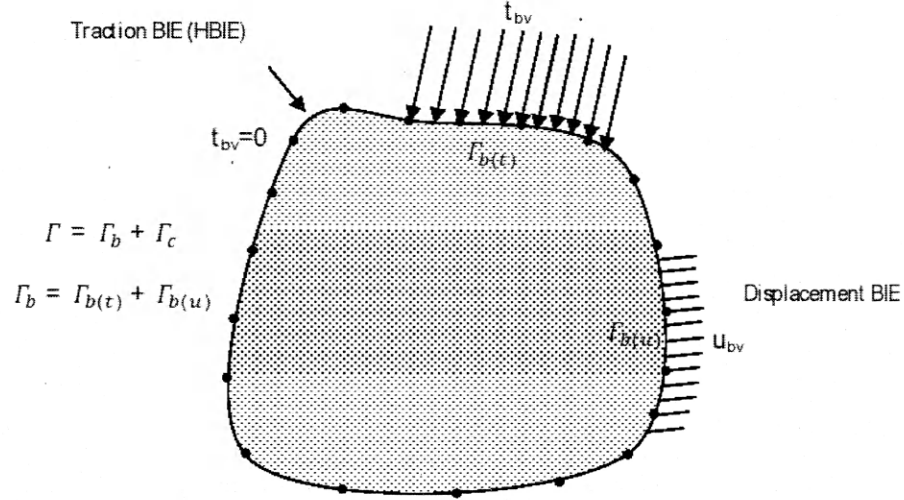
Figure 3.7: BEM discretization.

The symmetry of the coefficient matrix, $G_{11} = G_{11}^T, H_{22} = H_{22}^T$, and $H_{12} = G_{21}^T$ now follows from the symmetry properties of the kernel tensors [20].

3.5 Boundary Integral Calculation of Volume Averages

In the homogenization problem, the calculation of volume averages of stress and strain plays a very significant role. To efficiently calculate these averages, we take advantage of the boundary nature of the solution with boundary elements and use the results to compute effective stiffness or compliance tensors. The relationship between the volume average strain and the displacement boundary conditions can be written using the divergence theorem as [28], [29], [31]:

$$\langle \varepsilon_{ij} \rangle = \frac{1}{V} \int_V \varepsilon_{ij} dV = \frac{1}{2V} \int_\Gamma \left(u_i n_j + u_j n_i \right) d\Gamma \tag{3.51}$$

where u_i and n_i are components of the displacement and the normal vectors, respectively, and Γ is the boundary of the volume element. Similarly, the relationship between the average stress and the boundary traction is

$$\langle \sigma_{ij} \rangle = \frac{1}{V} \int_V \sigma_{ij} dV = \frac{1}{2V} \int_\Gamma \left(t_i x_j + t_j x_i \right) d\Gamma \tag{3.52}$$

where t_i is the boundary traction and x_i is the local coordinate of the volume element boundary. It is important to note that there is no unique relationship between the average stress or strain and the boundary tractions or displacements in the two- or three-dimensional case [29]. In other words, a number of different boundary displacements integrated over the boundary may produce the same average strain.

Application of the divergence theorem to obtain the surface integral formulation for the average stress requires that the local equilibrium equations must be satisfied point-wise in the domain. Therefore, the existence of the surface integral form given by Eq. (3.52) is guaranteed. Since we are using a boundary integral formulation for the solution of the elasticity problem, our solution exactly satisfies all governing equations within the domain, the approximation is on the boundary values of traction and displacement and not in the domain [12].

Eqs.(3.51) and (3.52) are *ideally* suited to computation by the boundary element method. After calculating the unknown boundary values of traction and displacement using the symmetric Galerkin BEM described in the previous sections, Eqs.(3.51) and (3.52) can easily be discretized and evaluated since all the boundary data are known. Let $\Gamma = \Gamma_o \bigcup \Gamma_v$ where Γ_o is the outer boundary of the volume element and Γ_v is the total boundary of the voids, see Figure 3.8. Then, for the $\langle \sigma_{ij} \rangle$ calculation, since the voids have traction-free surfaces,

$$\int_{\Gamma_v} (t_i x_j + t_j x_i) \, d\Gamma = 0, \tag{3.53}$$

so the only integral to perform is over the outer boundary of the volume element.
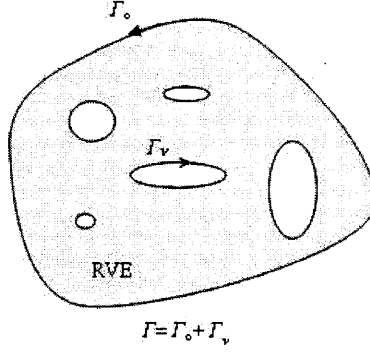
Figure 3.8: RVE with with voids and outer boundaries.

Restricting our calculations to the two-dimensional case, we introduce the usual quadratic, isoparametric shape functions, $N_k(\xi), -1 \le \xi \le 1$,

$$\begin{aligned}
N_1(\xi) &= \frac{1}{2}\xi(\xi - 1), \\
N_2(\xi) &= (1 - \xi)(1 + \xi), \\
N_3(\xi) &= \frac{1}{2}\xi(\xi + 1).
\end{aligned} \tag{3.54}$$

then we have

$$\langle \varepsilon_{ij} \rangle = \frac{1}{2V} \sum_{n=1}^{N} \int_{-1}^{1} \left[\left(\sum_{k=1}^{3} N_k u_i^{(k)} \right) n_j + \left(\sum_{k=1}^{3} N_k u_j^{(k)} \right) n_i \right] J d\xi \tag{3.55}$$

where N is the total number of boundary elements on Γ, the $u_i^{(k)}$ are the (known) nodal values of boundary displacement,

$$n_j = (-1)^{j-1} \frac{1}{J} \sum_{k=1}^{3} \frac{dN_k}{d\xi} x_j^{(k)} \tag{3.56}$$

$x_j^{(k)}$ are the nodal values of x_j, and J is the Jacobian of the transformation,

50

$$J = \left[\left(\sum_{k=1}^{3} \frac{dN_k}{d\xi} x_1^{(k)} \right)^2 + \left(\sum_{k=1}^{3} \frac{dN_k}{d\xi} x_2^{(k)} \right)^2 \right]^{1/2} \tag{3.57}$$

Note that the Jacobian term will cancel in Eq. (3.55) and (3.56), but we will need the Jacobian for the average stress calculation. That calculation can be obtained from the discretized form of Eq. (3.52),

$$\langle \sigma_{ij} \rangle = \frac{1}{2V} \sum_{n=1}^{N_o} \int_{-1}^{1} \left[\left(\sum_{k=1}^{3} N_k t_i^{(k)} \right) x_j + \left(\sum_{k=1}^{3} N_k t_j^{(k)} \right) x_i \right] J d\xi \tag{3.58}$$

where N_o is the number of boundary elements on the outer boundary *only*, the $t_i^{(k)}$ are the (known) nodal values of boundary traction, and the boundary coordinate x_j is interpolated in the usual way as

$$x_j = \sum_{k=1}^{3} N_k x_j^{(k)} \tag{3.59}$$

Although these results are for the two-dimensional setting, extension to three dimensions can be readily made.

Eqs. (3.56) and (3.58) allow us to readily compute the volume averages of stress and strain needed to evaluate the apparent elastic constants using information directly from the boundary element analysis.

CHAPTER 4

APPARENT ELASTIC CONSTANTS OF PZT CERAMICS

PZT ceramics are porous solids and are made of a composition of lead zirconate/lead titanate, containing about 95 % lead zirconate and 5% lead titanate [62]. Relative to other kinds of ceramics, PZT ceramics are widely used in a variety of pressure sensors and exhibit greater stiffness and higher operating temperatures, which make them widely used in ceramic industries. PZT ceramics are manufactured by burning pore formers with different shapes and contents during the sintering process. Figure 4.1 shows a porous PZT ceramic with different pore shapes and porosities. Resent work of [62] demonstrated that porous PZT ceramics helped prevent high-voltage break-downs at low temperature during explosive shock wave transformation. They also investigated experimentally the effects of porosity and pore shape on elastic constant of porous PZT ceramics. The effects of porosity and pore shape on electrical prop-erties of porous PZT ceramics are investigated in [75]. Furthermore, in an excellent agreement with the experimental work of [75], this dissertation studied numerically the effect of porosity and pore shape and volume element size on the elastic properties of porous PZT ceramics.

Because extracting the elastic stiffness tensor from representative volume element (RVE) is not always practicable, we are forced to work with volume elements which are smaller than the RVE, and we can determine *apparent* elastic constants. A methodol-ogy for approximating the apparent stiffness tensor using BEM and microstructural information is presented here. This is applicable even when these properties have a strong dependence on the boundary conditions and fabric tensor. Here, we present and apply this approach to determine the apparent elastic stiffness tensor of a PZT ceramic. Apparent elastic constants will vary with the position of the volume element, so the ergodicity assumption will not be satisfied. However, we can still approximate

the apparent elastic stiffness tensor of PZT ceramic, and the Hill criterion is still satisfied through appropriate boundary conditions.
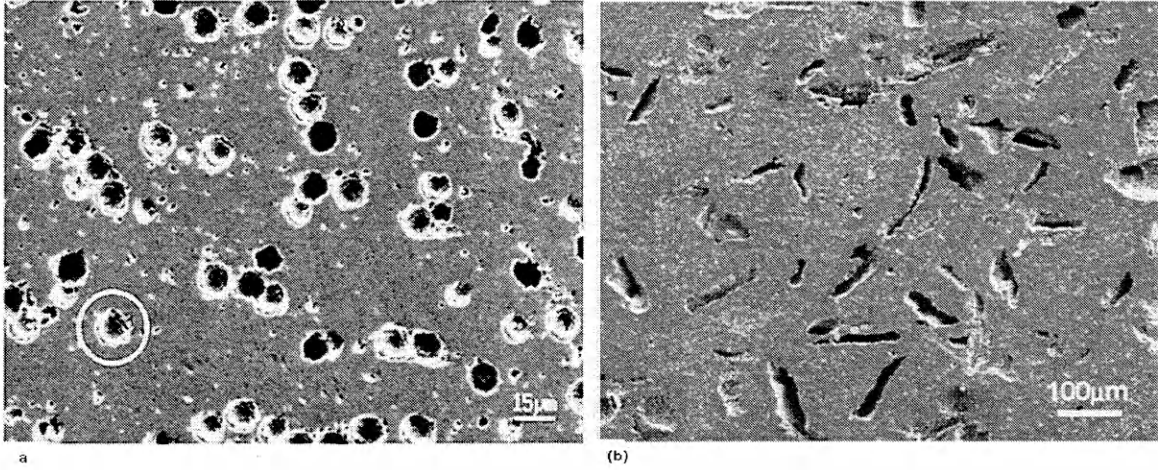
Figure 4.1: PZT ceramics (a) PZT ceramic with spherical pore shapes and porosity: 16.4% (PZT2); and (b) PZT ceramic with irregular pore shapes and porosity: 14.7% (PZT1) [75].

The main objective of this chapter is to present an appropriate two-dimensional boundary element model to study the mechanical behavior of a PZT ceramic with varying porosity, and pore size. Moreover, the Symmetric Galerkin Boundary Element Method (SGBEM) will be used to study the effects of volume element size on the solid ceramics properties.

4.1 Methodology

In the following sections of this chapter, we will discuss the over all methodology for analyzing two micrographs of PZT ceramics. To study the elastic constants variation with volume element size, an overview of fabric tensor approach and construction method will be presented. Furthermore, predictions of the elastic constants as a function of solid volume fraction will be plotted. In addition, we extract apparent elastic stiffness tensors using a symmetric Galerkin boundary element method, and the role of boundary conditions will be discussed. Finally, results are discussed and

53

concluding remarks are presented.

4.1.1   Extraction of PZT Ceramic Apparent Stiffness Tensor

To demonstrate the analysis methods described in the previous chapters, we will analyze two micrographs of porous lead zirconate titanate (PZT 95/5) ferroelectric ceramic shown in Figure 4.1. These micrographs were investigated and characterized in [75] and presented in this dissertation with permission of Elsevier. To conduct the numerical analysis, we will construct the fabric tensor for the two specimens, extract apparent elastic stiffness tensors using a boundary element analysis, and finally predict the elastic stiffnesses as a function of solid volume fraction and determine the volume element smallest size required for the analysis.

For the fabric tensor approach, mean intercept lengths (MIL) are used to construct the fabric tensor $\mathbf{H}$. These measurements were obtained on the micrographs of the ceramic specimens using Quant3D software (see Section 2). Furthermore, the eigenvalues were extracted from the fabric tensor $\mathbf{H}$ and properly normalized as z_1 and z_2. For the two-dimensional analysis the fabric tensor eigenvalues normalized as $z_1 + z_2 + z_3 = 3$, and we assume $z_2 = z_3$ in order for $E_2 = E_3$, $\nu_{12} = \nu_{13}$ and $G_{12} = G_{13}$ (transverse isotropic).

To perform the symmetric Galerkin boundary element analysis, the PZT ceramic micrographs were discretized as shown in Figure 4.2 and Figure 4.3. For the PZT ceramic with irregular pore shapes and a porosity 16.4%, we will refer to it as PZT1 (Figure 4.2). For the PZT ceramic with spherical pores and porosity 14.7%, we will refer to it as PZT2 (Figure 4.3).

For the numerical analysis, these two models were subjected to the following three types of boundary conditions on the outer boundary of the solid Γ_o:

1. Kinematic Uniform Boundary Conditions (KUBC).

   The displacement u_j is imposed at point x_j belonging to the boundary such

that

$$u_i = \varepsilon_{ij}^0 x_j \quad \forall x \in \Gamma_0$$

where ε_{ij}^0 is a constant strain tensor prescribed a *priori*. Note that this boundary condition satisfies Eq.(2.15) as it produces uniform strain in the volume.

2. Static Uniform Boundary Conditions (SUBC).

A uniform traction t_j is imposed on the boundary such that:

$$t_i = \sigma_{ij}^0 n_j \quad \forall x \in \Gamma_0$$

where σ_{ij}^0 is a constant stress tensor prescribed a *priori*. This boundary condition also satisfies Eq.(2.15) as it produces uniform stress in the volume.

3. Mixed Uniform Boundary Condition (MUBC).

There are several choices for MUBC which will satisfy the form of the Hill criterion given in Eq.(2.16),

$$\left(t_i - \sigma_{ij}^0 n_j\right)\left(u_i - \varepsilon_{ij}^0 x_j\right) = 0 \quad \forall x \in \Gamma_0$$

The mixed uniform boundary conditions MUBC were first introduced by Zysset and Pahr [54]. They stated that MUBC are the best choice in the case of very small volume elements in order to obtain the same overall elastic constants as periodic BCs, i.e. the effective elastic properties. Appropriate choices for MUBC are studied and reviewed in [54].

As illustrated in Figure 2.4, each of these choices for boundary conditions will yield different apparent constants, as discussed in detail in Chapter 2. When the average stresses and strains are computed from the boundary element analysis from Eq. (3.51) and Eq. (3.52), a system of five equations (in two dimensions) can be formed and the five material properties needed to compute the apparent stiffness tensor can be obtained. We note that the stresses and strains used in the volume averages calculations must first be transformed to the principal material coordinates. This transformation

is accomplished using the rotation angle obtained from the eigenvectors of the fabric tensor since the principal axes at the material and the fabric tensor are coincident [53]. The tensor rotation can be performed using standard tensor transformation methods. The results from the SGBEM analysis for the apparent stiffness tensor and three different boundary conditions, are shown in Table 4.1. Note in Table 4.1 that the predictions of the elements of the apparent stiffness tensor agree with the bounds given in Chapter 2.
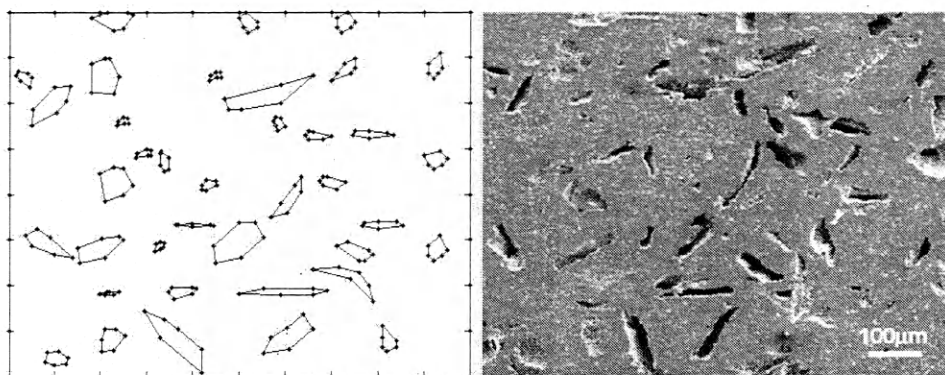
Figure 4.2: Boundary element mesh for PZT1.
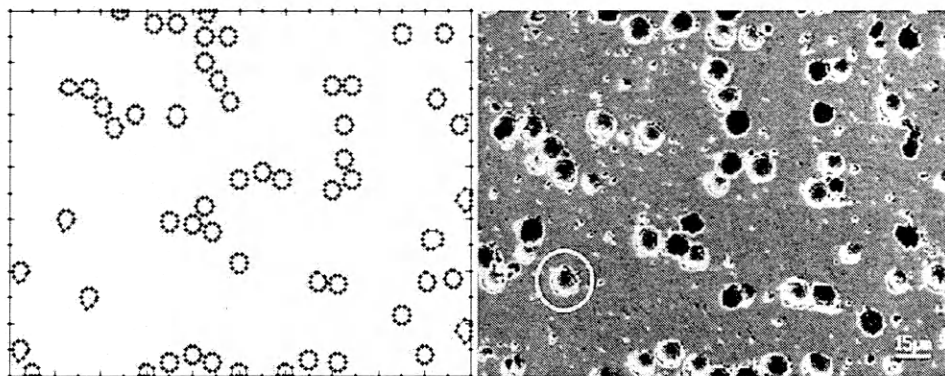
Figure 4.3: Boundary element mesh for PZT2.

To construct the fabric tensor, mean intercept length measurements were obtained on the micrographs of the ceramic specimens using commercial computerized tomography software (Quant3D). The mean intercept lengths were used to construct the

fabric tensor **H**, then the eigenvalues were extracted and properly normalized as z_1 and z_2 for the two-dimensional analysis, see Table 4.2. As mentioned above, the eigenvectors corresponding to the fabric tensor eigenvalues were extracted from the image analysis by Quant3D software, these are needed to know the orientation of the principal material axes relative to the (x, y) coordinates fixed by the boundaries of the micrograph. It is in the principal material axes where the relationships given by Eq. (2.30) are valid.

Table 4.1: Results for the apparent elastic constants from SGBEM analysis (E and G values are in GPa).

BCs	KUBC	SUBC	MUBC
PZT1			
E_1	101.10	91.20	92.76
E_2	86.90	80.80	85.32
G_{12}	43.11	31.98	35.18
ν_{12}	0.25	0.21	0.22
PZT2			
E_1	102.78	98.31	101.31
E_2	95.16	92.86	94.01
G_{12}	40.94	37.72	39.00
ν_{12}	0.26	0.23	0.24

Having estimates of the apparent stiffness tensor as well as the eigenvalues of the fabric tensor, we may now estimate the constants k, ℓ appearing in Eq. (2.30). For the bulk isotropic material properties E_0, ν_0 we use values for PZT ceramic from [75] of $E_0 = 165$ GPa and $\nu_0 = 0.22$, G_0 can be calculated from E_0 and ν_0 since the solid matrix is assumed to be isotropic,
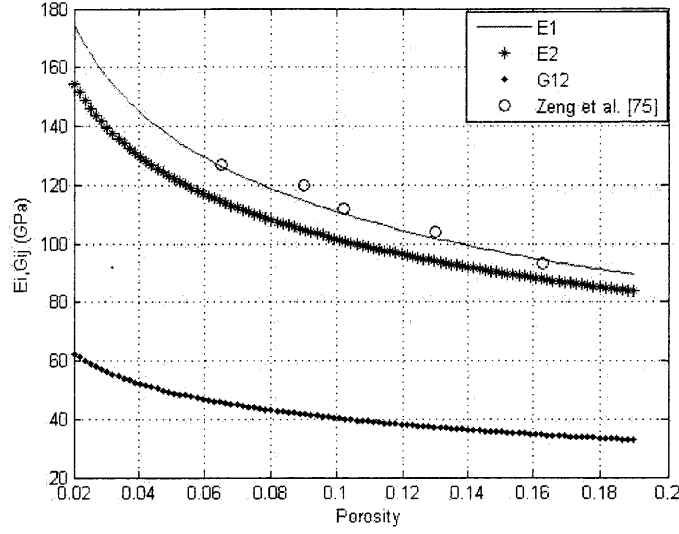
Figure 4.4: Variation of elastic moduli with porosity for PZT1 (irregular pore shapes) and the *circles* represent the experimentally measured values [75].

$$G_0 = \frac{E_0}{2(1 + \nu_o)}. \tag{4.1}$$

The results are given in Table 4.2 where the MUBC results from Table 4.1 were used to perform a least-squares estimate for k, ℓ. The recomputed values of the orthotropic elastic stiffnesses (based on Eq. 2.30) are shown in Table 4.2 in order to compare to those shown in Table 4.1. Predictions for E_1, E_2 and G_{12} as functions of porosity $(1\text{-}v_s)$ using Eq. (2.30) and the constants from Table 4.2 are shown in Figure 4.4 and Figure 4.5. Note the excellent comparison with the experimental results reported in [12].

Table 4.2: Results for the constants in the fabric-stiffness relations, Eq. 2.30, and recomputed values of the elastic constants. Values of E and G are in GPa.

	v_s	z_1	z_2	θ^o	k	ℓ	E_1	E_2	G_{12}	ν_{12}
PZT1	0.836	1.0612	0.9687	41.13	0.35	0.48	92.89	85.00	35.85	0.24
PZT2	0.853	1.0306	0.9847	27.83	0.28	0.71	100.67	94.36	33.94	0.22
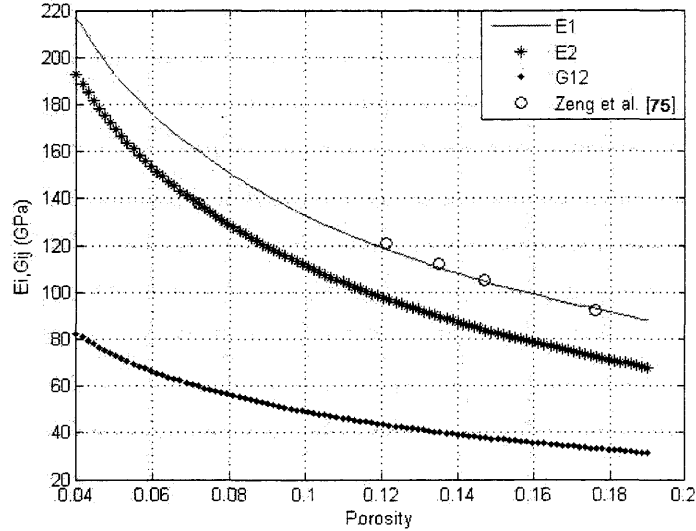
Figure 4.5: Variation of elastic moduli with porosity for PZT2 (spherical pore shapes) and the *circles* represent the experimentally measured values [75].

4.1.2   Effect of Volume Element Size

The existence of a representative volume element (RVE) is critical for extracting material overall properties. Studying the volume element size is necessary for quantitative comparisons in determining the apparent elastic properties. One definition of an RVE is related to the volume size at which the material properties become independent of the choice of boundary conditions [61]. But, for volumes smaller than the RVE, the boundary conditions are very significant in the estimation of the apparent mechanical properties.

In this section, we study the effect of volume element size on the apparent stiffness of PZT2 (PZT ceramic with spherical pores and porosity of 14.7%). A core problem in such investigation is the determination of the appropriate size of volume element in order to get an accurate approximation of apparent properties. This is related to the longstanding issues of the determination of the size of the volume element (VE) in homogenization theory.

As mentioned above, if we are using volumes less than the RVE, we can calculate

upper and lower bounds on the stiffness or compliance tensor by applying SUBC or KUBC, or we can obtain an intermediate estimate using MUBC on the volume element (see Chapter 2). Briefly, as the volume element becomes bigger, these bounds eventually converge to the effective stiffness or compliance tensor see (Figure 2.4). Therefore, our objective is to find the smallest size of volume element required to estimate precisely the effective elastic constants.

To perform this objective, the PZT ceramic micrograph with spherical pores shown in Figure 4.1 was divided to four smaller volume elements: VE1, VE2, VE3, and VE4. As shown in Figure 4.6, where $VE1 = V$, $VE2 = 0.75V$, $VE3 = 0.5V$ and $VE4 = 0.25V$ where VE is the full volume.

To perform this target, these volumes were discretized for SGBEM analysis and simulation. As discussed previously in this chapter, these models were subjected to the three types of boundary conditions on Γ_o, the outer boundary of the solid. These choices for boundary conditions will yield different elastic constants. Similar calculations as those described previously were performed to calculate the elastic constants from the average stresses and strains. Because our model is in two dimensions, we end up with a system of five equations with five unknowns.

The results for the Young's modulus E_1 are shown in Table 4.3. Moreover, using mixed uniform boundary conditions, the variation of the Young's modulus E_1 with the volume elements under consideration is shown in Figure 4.7.

4.2 Results and Discussion

In this chapter we have explored three points: (i) Application of the symmetric Galerkin boundary element method (SGBEM) and the fabric tensor approach on micrographs of PZT ceramics. (ii) Extracting the apparent elastic constants of PZT ceramics and comparison with the experimental data in the literature. (iii) The effects of volume element size on the elastic constants in two kind of PZT ceramic materials.

60
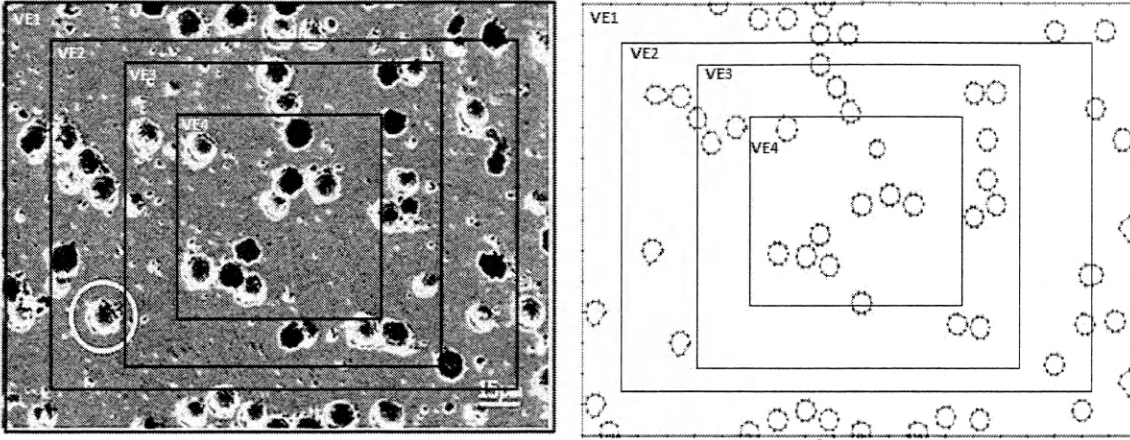
Figure 4.6: Volume element divisions of PZT2 ceramic micrograph.

We will discuss our results on each of these point next.

Table 4.3: Results for the Young's moduli E_1 in (GPa) for the different volume elements.

VE	KUBC	SUBC	MUBC
$VE1$	102.78	98.31	101.31
$VE2$	109.90	91.80	103.82
$VE3$	111.11	89.98	106.85
$VE4$	115.25	85.21	109.06
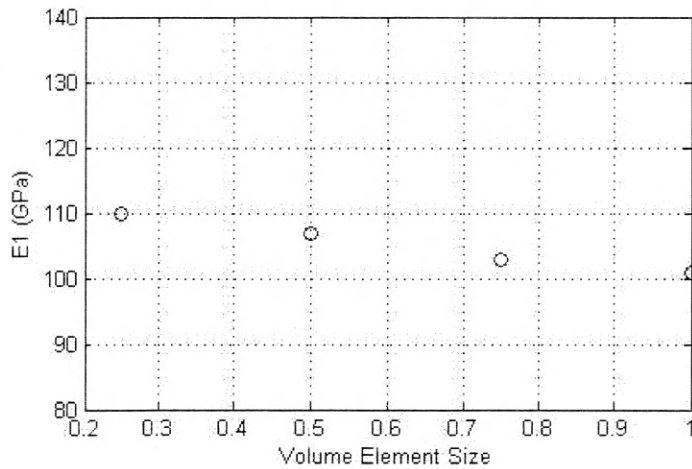
Figure 4.7: Young's modulus variation with volume element size.

In order to predict predicting the overall material properties, fabric measurements

61

were obtained on two PZT 95/5 ceramic micrographs. A computerized tomography software (Quad3D) was used to determine the fabric tensors, eigenvalues, and eigenvectors. The overall elastic moduli for PZT ceramics were then computed using volume average-stress and strain values combined with the fabric tensor eigenvalues. The calculated results were compared with the experimental data in the literature and show an excellent agreement, see Figure 4.4 and Figure 4.5. Furthermore, by applying three types of boundary conditions, (KUBC, SUBC, and MUBC) we could compare our numerical results with bounds reported in the homogenization literature. Our results agreed exactly with the bounds given in the literature.

One of our objectives in this chapter was to find the smallest size of volume element required to compute the effective elastic constants. The effect of volume element size on Young's modulus E_1 of PZT1 was analyzed and plotted. The fact that the values of the apparent elastic constant depend on the RVE size was approved. Larger volumes are necessary to obtain an apparent properties which are not too far from the effective elastic constants. However, the chosen volume element VE cannot be taken as small as one may wish, because there exists in general a condition in the estimation of the effective properties. The convergence of apparent constants obtained using three types of boundary conditions toward the effective modulus (see Table 4.3).

CHAPTER 5

EFFECT OF VOID SHAPE, SIZE, AND ORIENTATION ON THE FABRIC TENSOR

The elastic constants of single phase porous materials exhibit properties that are dependent on the void shapes, size, and orientation. The volume fraction, v_s or porosity, Φ, are one important microstructural feature in porous materials and have a significant influence on their mechanical and physical properties [60]. In addition, the aspect ratio of the elliptical voids and their direction may have an effect on the elastic constants of the porous solids. These features of microstructural geometry comprise the structural anisotropy, which is accounted for by the use of a fabric tensor [12]. The purpose of the study in the present chapter is to determine the relation between these features and the material's apparent elastic constants.

As mentioned in previous chapters, homogenization theories have been widely used for the analysis and design of porous materials. With such an approach, a representative volume element (RVE) is sought, which is representative of the material behavior including microstructural properties that may affect the stress analysis. The fabric tensor is one approach to characterize a material's microstructure within an RVE. The fabric tensor can be best viewed as a term in a tensorial series representation of an orientation distribution function [74]. A second order fabric tensor is used to describe materials which are isotropic, transversely isotropic, or orthotropic in a homogenized sense. A second-rank fabric tensor was originally used by Cowin [7], [69], [70] to describe a material's microstructure from which homogenized elastic constants could be predicted. These definitions were refined and developed later in a series of elegant works by Zysset [54], [77], [76]. The refinements to the original Cowin expressions insured that the elastic stiffness tensor was positive definite and decreased the number of constants required in the Cowin expressions. These analysis

methods were applied to a common set of experimental data in [76] and it was found that in certain cases the Cowin relations did indeed yield stiffness tensors that were not positive definite.

To construct the fabric tensor for any porous material, there are a variety of methods described in the literature as described in Chapter 2. The most commonly used method is the mean intercept length (MIL) [22] but a number of other methods are also used. For example, the star-volume distribution (SVD) [10], star-length distribution (SLD) and volume orientation (VO) [52] are frequently used. MIL was first proposed by Whitehouse [74], which at some arbitrarily selected direction defined the mean intercept length as the relative solid area divided by the total projected boundary perimeter per unit area. The distribution of the MIL forms an ellipsoid, and the coefficient of the ellipsoid provide a second-rank fabric tensor $\mathbf{H}$. The MIL fabric tensor, $\mathbf{M} = \mathbf{H}^{-1/2}$ has eigenvectors which represent the principal directions (i.e the axes of the ellipsoid) and eigenvalues which define the tendency of the material to be oriented along the respective principal directions [22]. The eigenvalues of $\mathbf{H}$ are z_1, z_2 and z_3 and must be normalized as $z_1 + z_2 + z_3 = 3$ for use in predicting elastic constants. Also, $z_2 = z_3$ in the two-dimensional case of transverse isotropy. The investigations reported in [3] and [12] used the fabric tensor $\mathbf{H}$ to explore the use of boundary element methods in predicting orthotropic elastic constants.

In this chapter the influence of pore shape, pore orientation, and volume fraction on the apparent elastic constants of both a PZT ceramic and several model materials is examined using three methods of fabric tensor construction: MIL, SVD, and SLD. A comparison of these fabric tensor construction methods is presented. We note that the fabric determination methods reviewed in Chapter 2, i.e., MIL, SLD and SVD, are not the only methods available in the literature. There are several other measurement methods, such as volume orientation descriptor (VO) [53], mean free path, and areal porosity distribution, which have been widely used in bone mechanics [33]. These

additional methods will not reviewed in this dissertation.

5.1 Construction of Second-Rank Fabric Tensors

As mentioned previously the fabric tensor can be constructed from mean intercept lengths, (MIL) [74], volume orientation distribution [53], star-volume distribution (SVD) [10], star-length distribution (SLD) [52] as well as other methods. In this chapter, we will consider some of these methods to construct the models fabric tensor and its eigenvalues. To construct fabric tensors from either the SVD or SLD data, we will use the common approach of fitting an ellipsoid directly to the directional distribution data. However, for SVD and SLD data there are other approaches used to construct the fabric tensor such as the moment of inertia based $T-$matrix method of [37] and [14].

The main objective of this chapter is to study the effect of aspect ratio, void orientation, and volume fraction on elastic properties and the fabric tensor. For this purpose, we generate several different idealized material models with different aspect ratios and a variety of volume fractions. The first part of this investigation will aim to study the effect of the aspect ratio of the pores on the elastic properties when the volume fraction is kept constant. Next, we study the effect of the orientation of the pores on the fabric tensor.

5.2 Effect of Aspect Ratio

The aspect ratio of the elliptical pores has an effect on the elastic stiffness. In this section we generate three idealized models (I1, I2, I3) with aspect ratios of 0.400, 0.625, and 1.000 see Figure 5.1, Figure 5.2, and Figure 5.3. The volume fraction, v_s, is kept constant for all three models. Three fabric tensor construction methods are used to compare the results with volume average calculations.

Also, the orientation angle θ for each model is given in Table 5.1. We can assume

that the body coordinates and the principal material coordinates are aligned since the rotation angle, θ, for I1, I2, and I3 is approximately zero. We also note that the orientation angle agrees with the orientation of the pores.

We next determine elastic constants in a manner similar to that reported in Chapter 4. Results for the eigenvalues of I1, I2, and I3 are presented in Table 5.1. Note that the eigenvalues are slightly different from MIL, SVD, and SLD. For the transversely isotropic situation assumed here, there are five unknown constants in the effective elastic stiffness tensor for each model, so we will calculate the necessary volume averages for SUBC type of boundary conditions. Then we extract the elastic stiffness values in a least-squares sense from this data which is shown in Table 5.2. Here we will mainly reported the in-plane engineering constants, i.e., E_1, E_2, and G_{12}, noting that ν_{12} (not reported here) is independent of the solid volume fraction v_s [3], and that the fifth unknown elastic constant pertains to out-of-plane normal stress. Results for these volume-average based elastic constants are given in the last column of Table 5.2. For comparison, in Table 5.3 we also present the apparent elastic constants calculated from each type of boundary condition presented in Chapter 2. (SUBC, KUBC and MUBC).

Table 5.1: Fabric tensor eigenvalues and orientation angle from MIL method for I1, I2, and I3.

I1, I2, and I3	I1:a/b=0.4	I2:a/b=0.625	I3:a/b=1
z_1	1.6667	1.3321	1.0144
z_2	0.6667	0.8339	0.9928
θ^o	1.1451	1.0121	0.9421
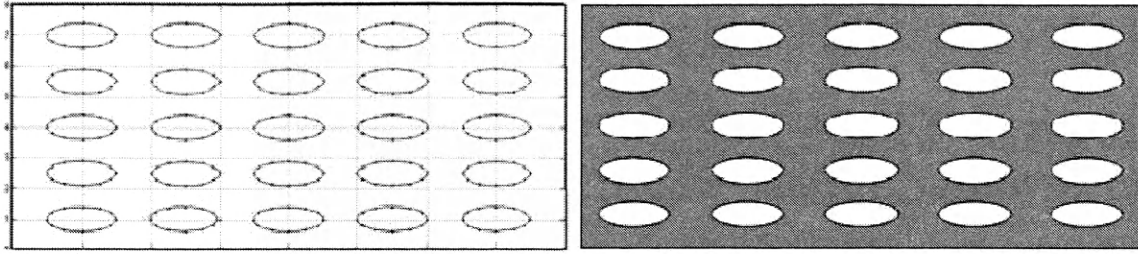
Figure 5.1: Grayscaling images and BEM models for I1 material model with constant volume fraction and aspect ratio of a/b=0.4.
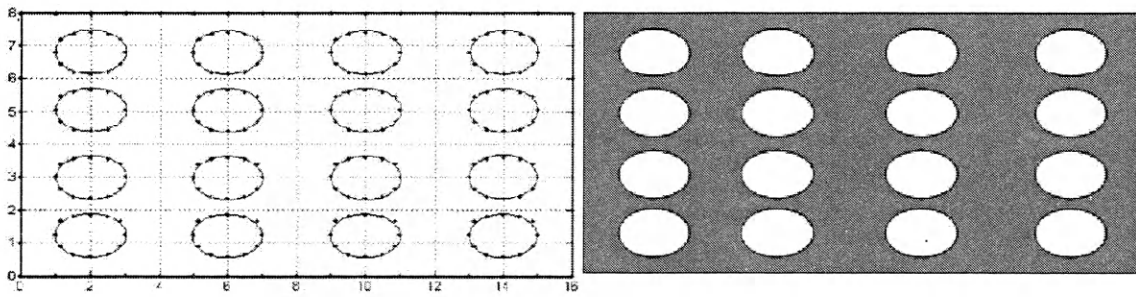
Figure 5.2: Grayscaling images and BEM models for I2 material model with constant volume fraction and aspect ratio of a/b=0.625.
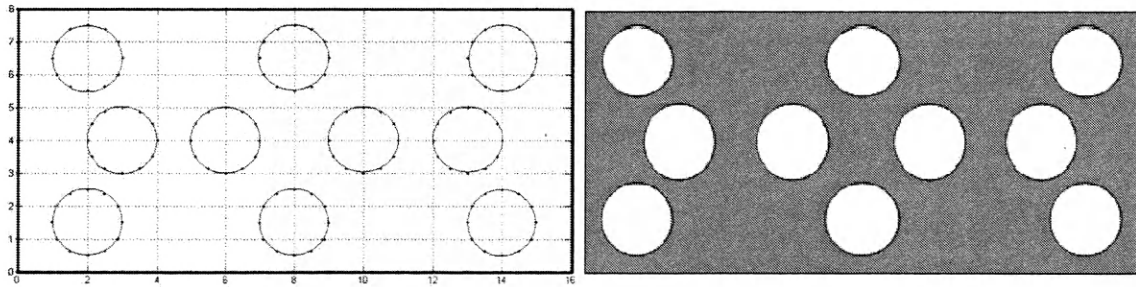
Figure 5.3: Grayscaling images and BEM models for I3 material model with constant volume fraction and aspect ratio of a/b=1.

Table 5.2: Comparison of elastic constants using the three fabric tensor methods. The last column reports the volume averaged values.

	MIL	SVD	SLD	$\langle \sigma \varepsilon \rangle$ with SUBC
I1 (a/b=0.4)				
E_1	133.57	147.81	145.77	140.29
E_2	107.39	97.41	108.90	112.65
G_{12}	49.08	49.17	51.63	51.01
I2 (a/b=0.625)				
E_1	136.83	145.82	131.85	137.11
E_2	112.30	96.97	111.08	115.02
G_{12}	50.8064	48.7393	49.5997	52.11
I3 (a/b=1)				
E_1	127.16	135.66	134.41	132.97
E_2	123.48	111.82	111.14	117.65
G_{12}	51.35	50.47	50.09	53.74

Table 5.3: Results from SGBEM analysis for the three idealized models.

BCs:	KUBC	SUBC	MUBC
I1			
E_1	146.94	136.55	144.51
E_2	117.23	107.98	115.82
G_{12}	54.4	45.11	53.90
I2			
E_1	144.82	135.9	141.33
E_2	123.02	116.93	117.91
G_{12}	52.34	48.08	51.51
I3			
E_1	139.78	131.12	137.01
E_2	122.62	111.59	115.02
G_{12}	51.90	47.21	50.32

The results shown in Table 5.2 and Table 5.3 were obtained using E_o =380 GPa and ν_o = 0.22. Note that the stiffness values obtained for all models are always rotated such that $E1 > E2$. The KUBC (upper bound) and SUBCs (lower bound) of elastic constants is again verified and the highest differences are observed for the G_{12} shear moduli.

Finally, we plot the fabric tensor ellipses for the three idealized materials Figure 5.4. This figure shows the ellipses determined from MIL for each model. From this plot, the effect of the changing aspect ratios is clear. In comparing the ratio of z_1/z_2 to the aspect ratio of the pores yield the almost equal ratios for the three materials model as expected.

5.3 Effect of Void Orientation and Volume Fraction on the Fabric Tensor and Elastic Constants

In this section, we generate another set of idealized material models, $M1, M2$, and $M3$, to investigate the influence of the volume fraction, v_s, and void orientation, α, on the fabric tensor ellipse and apparent elastic properties. The three models are shown in Figure 5.5, Figure 5.7, and Figure 5.7. The aspect ratios are varied from 0.1 to 1, as seen in figures.

For two additional cases we select model M1 (aspect ratio of 0.1) and model M3 (aspect ratio of 0.2) and vary the orientation of the voids. For these models, we also decrease the volume fraction, v_s, by extending the pores to increase the porosity; see Figure 5.8 and Table 5.4. For apparent elastic constant, we again follow the same procedure as was done previously to extract the apparent stiffness tensors using boundary element analysis, where the fabric tensor eigenvalues and eigenvectors were extracted using the commercial software Quant3D. The numerical results from the image analysis for the elastic constants are shown in Table 5.5. These results show

that the elastic Young's moduli E_1 and E_2 decrease with volume fraction, v_s, and increase with aspect ratio a/b. The same changes were noted on the shear modulus G_{12} with the change in volume fraction and aspect ratio.
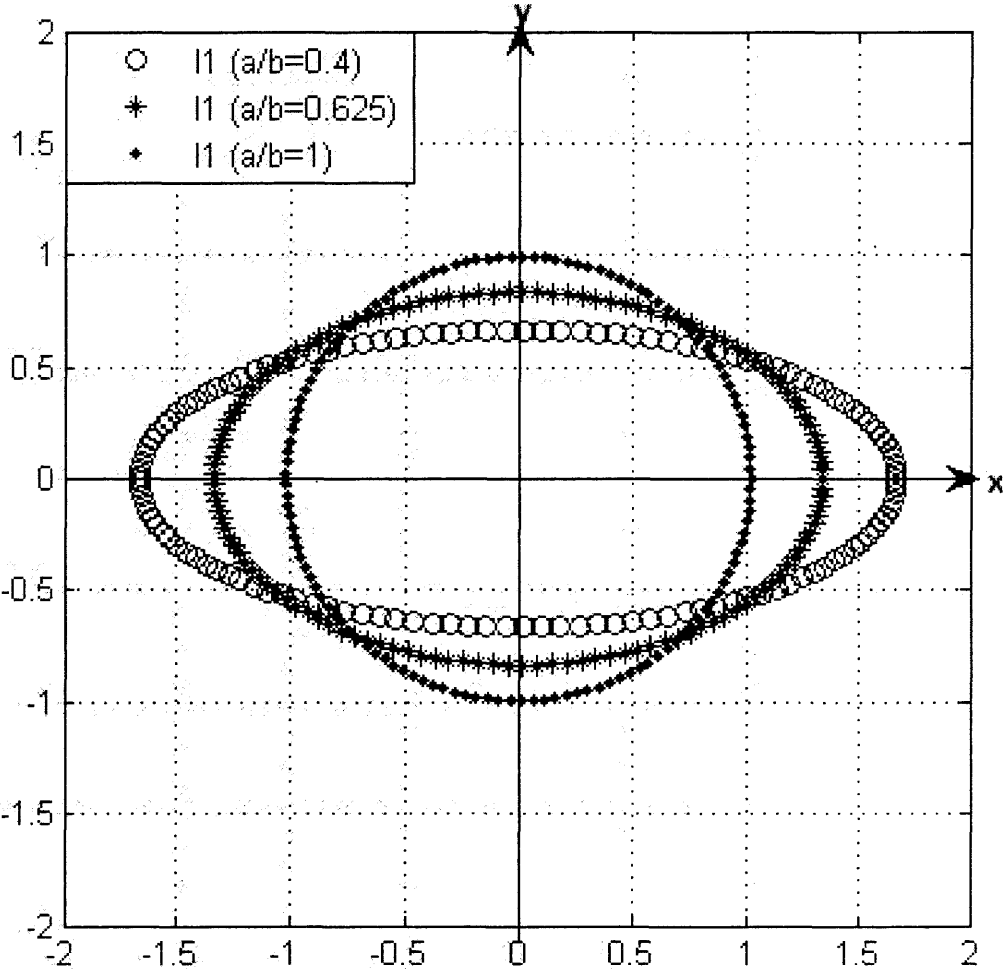
Figure 5.4: Fabric tensor ellipses comparison for I1, I2, and I3.

Table 5.4: Idealized models M1 and M3 for fabric orientation study.

	M1R1	M1R2	M1R3	M3R1	M3R2	M3R3
v_s	0.97	0.95	0.93	0.94	0.92	0.84
a/b	0.1	0.1	0.1	0.2	0.2	0.2
α^o	0	0	0	60	60	60

Table 5.5: Models M1, M2 and M3 with different aspect ratio and predicted apparent stiffness.

a/b	0.1	0.2	0.4	0.6	0.8	1
v_s	0.97	0.94	0.86	0.80	0.73	0.67
$M1\alpha = 0^o$						
E_1	319.02	240.22	221.77	205.34	183.97	170.76
E_2	240.36	134.73	117.85	110.39	96.76	89.77
G_{12}	109.19	88.55	77.65	65.83	55.78	50.66
$M2\alpha = 30^o$						
E_1	317.79	240.08	216.33	201.74	183.55	170.76
E_2	239.41	134.16	115.90	113.73	96.76	89.77
G_{12}	108.98	86.07	77.64	67.94	58.93	50.66
$M3\alpha = 60^o$						
E_1	316.99	241.86	220.57	203.83	185.90	170.76
E_2	238.88	132.70	114.63	109.95	99.40	89.77
G_{12}	108.43	87.17	78.68	63.70	56.87	50.66

In Table 5.6 we present results for the M1 model ($\alpha = 0^o$), with an aspect ratio of $a/b = 0.1$, and different volume fractions (0.97, 0.95, 0.93), and the M3 model ($\alpha = 60^o$) with aspect ratio of $a/b = 0.2$, and different volume fractions (0.944, 0.9238, 0.8445). These materials models are shown in Figure 5.8.
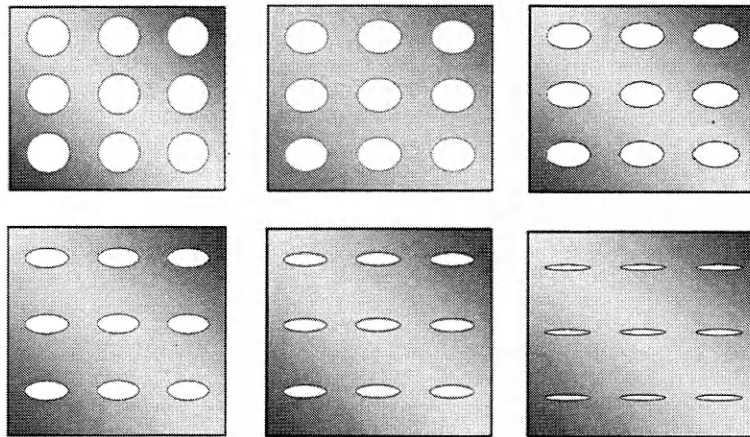
Figure 5.5: Model M1 with pore angle $\alpha = 0^o$.
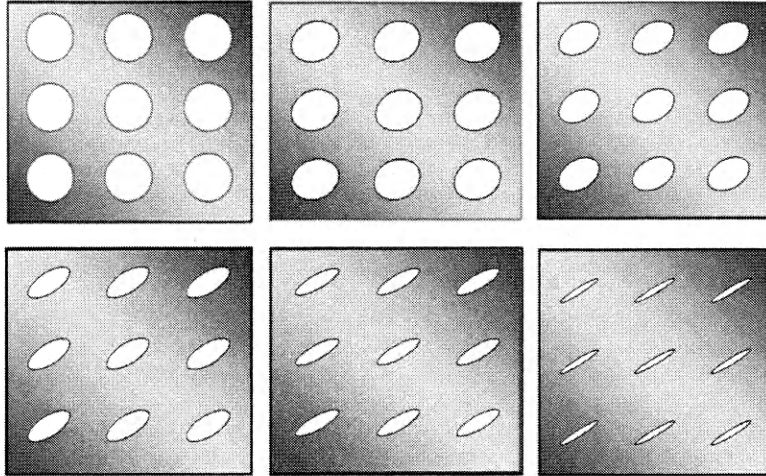
Figure 5.6: Model M2 with pore angle $\alpha = 30^o$.
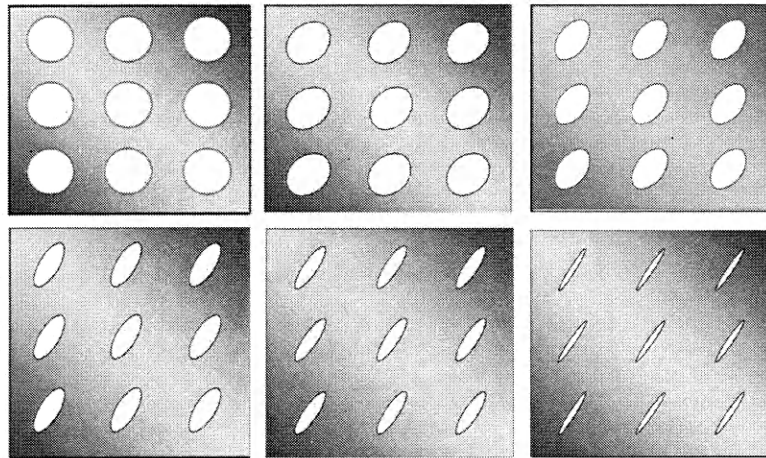
Figure 5.7: Model M3 with pore angle $\alpha = 60^o$.

We next plot the MIL ellipses for these materials to show the changes in fabric tensor orientation and the effect of volume fraction and pore orientation on the fabric tensor ellipses. Figure 5.9 and Figure 5.10 show the MIL ellipses for M1 and M3 with variation in v_s and aspect ratio, respectively. From these figures we can see that the volume fraction does not affect the size and orientation of the MIL ellipse or the corresponding eigenvalues. This result is expected since the fabric tensor is a measure of the structural anisotropy which should be independent of the material's volume
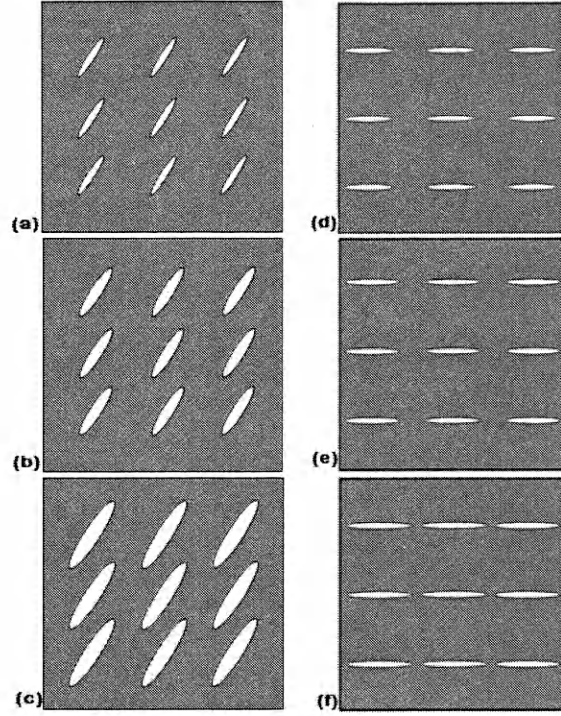
Figure 5.8: M1 and M3 models for studying the influence of volume fraction on material fabric tensor: (a) M3R1 (b) M3R2 (c) M3R3 (d) M1R1 (e) M1R2 (f) M1R3.

fraction, v_s.

5.4   Impact of Fabric Tensor Determination Method

In this section we will investigate the effect of the method of fabric tensor determination on predictions of elastic constants in idealized materials. The results of using the MIL, SVD, and SLD method for these models are shown in Table 5.8 and Table 5.9. Overall we find that the method of fabric tensor determination does not affect the prediction of elastic constants in a systematic way for the class of materials we considered. For idealized material M1, the minimum difference with volume average values occurred for E_2 from SVD, and the maximum difference occurred with G_{12} from MIL. For M3, the minimum was with E_1 from MIL and the maximum with G_{12} from MIL. Where, for M2 idealized material, the results are not reported here.
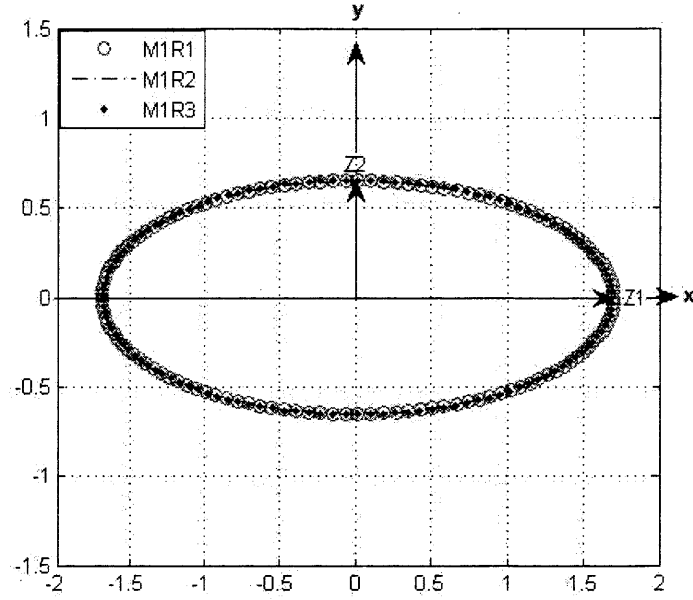
Figure 5.9: MIL ellipses for M1R1, M1R2, and M1R3 show no change with volume fraction changes.

Table 5.6: MIL fabric tensor values for Model M1 ($\alpha = 0^o$) and aspect ratio a/b=0.1 and Model M3 ($\alpha = 60^o$).

model M1	M1R1	M1R2	M1R3
v_s	0.97	0.95	0.93
z_1	1.6986	1.7031	1.6879
z_2	0.6507	0.6484	0.6561
θ	0.34	1.05	1.02
model M3	M3R1	M3R2	M3R3
v_s	0.94	0.92	0.84
z_1	1.4548	1.4902	1.5075
z_2	0.7726	0.7549	0.7463
θ	60.30	60.10	59.63
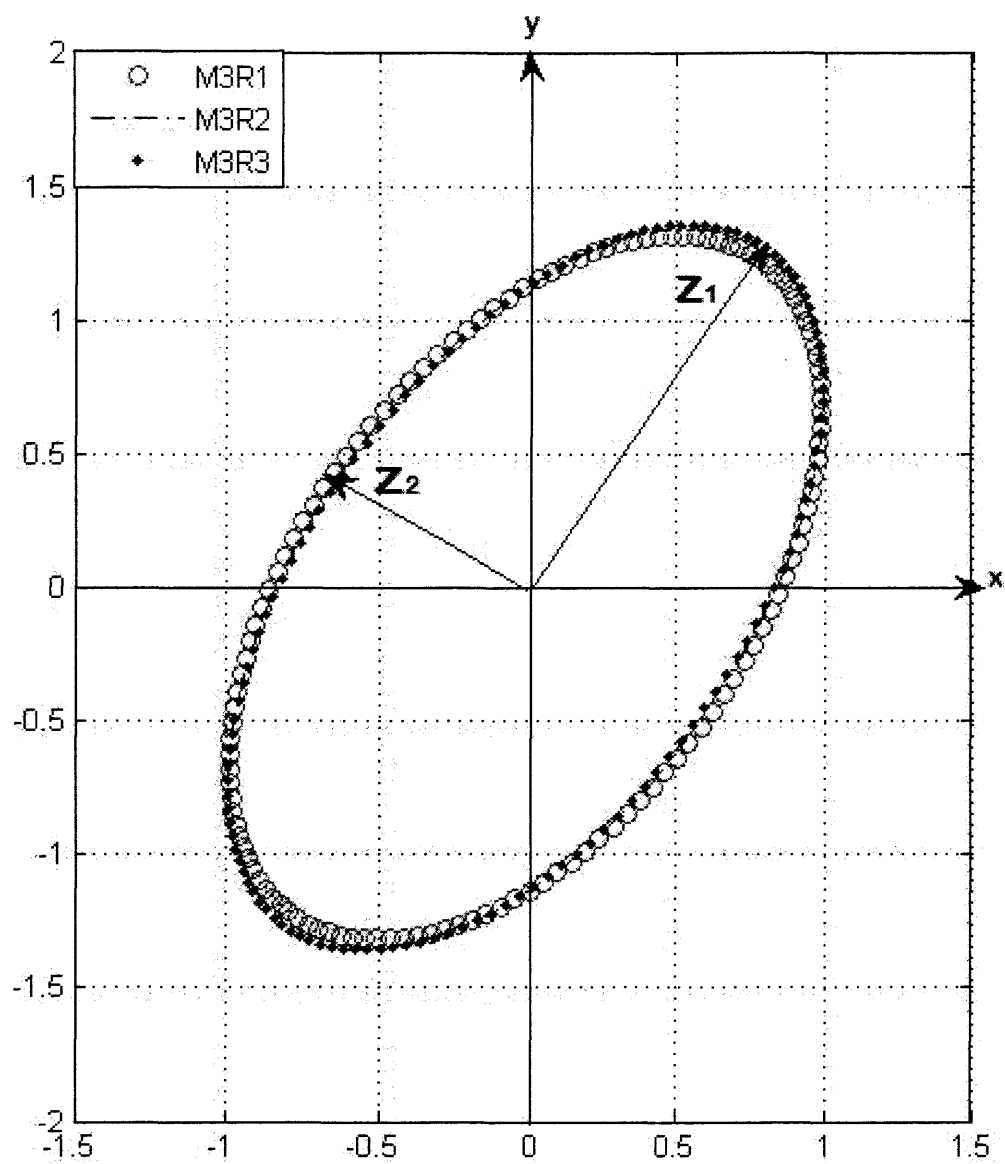
Figure 5.10: MIL ellipses for M3R1, M3R2, and M3R3 show no change with volume fraction changes.

Table 5.7: MIL, SVD, and SLD fabric tensor construction method and Zysset constants k, l for Model M1R1, M1R2, and M1R3.

	MIL	SVD	SLD
M1R1 ($v_s = 0.97$)			
z_1	1.6986	1.9991	1.8325
z_2	0.6507	0.5005	0.5838
k	9.5921	9.8422	10.8420
l	0.1501	0.1231	0.1621
M1R2 ($v_s = 0.95$)			
z_1	1.7031	1.9950	1.8351
z_2	0.6484	0.5025	0.5824
k	8.3101	7.9040	8.2987
l	0.1421	0.1121	0.1221
M1R3 ($v_s = 0.93$)			
z_1	1.6879	1.9988	1.8312
z_2	0.6561	0.5006	0.5844
k	6.6779	6.5711	6.8411
l	0.1321	0.1101	0.1191

Table 5.8: MIL, SVD, and SLD fabric tensor construction method and Zysset constants k, l for Model M3R1, M3R2, and M3R3.

	MIL	SVD	SLD
M3R1 ($v_s = 0.94$)			
z_1	1.4548	2.3004	1.5443
z_2	0.7726	0.3498	0.7278
k	13.7971	12.9171	13.8569
l	0.4257	0.1491	0.4157
M3R2 ($v_s = 0.92$)			
z_1	1.4902	2.2880	1.5470
z_2	0.7549	0.3560	0.7265
k	10.3810	9.810	10.3941
l	0.4110	0.1410	0.3994
M3R3 ($v_s = 0.84$)			
z_1	1.5075	2.1402	1.5406
z_2	0.7463	0.4299	0.7297
k	6.1811	5.55486	6.0391
l	0.5491	0.2600	0.5301

Table 5.9: The apparent elastic constants of M1 and M3 with different volume fractions using MIL,SVD, SLD and volume averaging methods.

	MIL (% Difference)	SVD (% Difference)	SLD (% Difference)	$\langle \sigma \varepsilon \rangle$
M1R1: E_1	332.63 (4.26)	333.92 (4.67)	332.38 (4.18)	319.02
E_2	249.38 (3.75)	237.45 (1.21)	229.39 (4.56)	240.36
G_{12}	118.04 (8.10)	115.40 (5.68)	113.16 (3.63)	109.19
M1R2: E_1	288.65 (1.38)	295.77 (3.88)	287.94 (1.13)	284.72
E_2	219.37 (2.67)	217.12 (3.67)	217.56 (3.47)	225.39
G_{12}	103.13 (1.20)	103.85 (1.92)	102.57 (0.66)	101.90
M1R3: E_1	268.77 (1.61)	274.73 (3.87)	267.15 (1.00)	264.49
E_2	209.39 (0.46)	202.53 (3.72)	203.51 (3.25)	210.36
G_{12}	97.22 (0.03)	96.67 (0.53)	95.56 (1.67)	97.19
M3R1: E_1	236.09 (1.61)	231.41 (3.87)	245.40 (1.00)	240.22
E_2	137.74 (0.46)	131.97 (3.72)	131.29 (3.25)	134.73
G_{12}	73.90 (0.03)	71.62 (0.53)	73.56 (1.67)	88.55
M3R2: E_1	231.66 (1.33)	233.64 (2.20)	236.24 (3.33)	228.61
E_2	132.45 (1.14)	138.26 (3.18)	129.16 (3.59)	133.98
G_{12}	71.79 (6.34)	73.66 (3.90)	71. 59 (6.60)	76.65
M3R3: E_1	209.821 (0.32)	221.012 (4.99)	216.52 (2.86)	210.49
E_2	96.94 (3.46)	95.89 (4.52)	98.04 (2.38)	100.43
G_{12}	58.45 (17.69)	59.66 (15.98)	59.71 (15.91)	71.01

In conclusion, each values of elastic moduli, E_1, E_2 and G_{12} for models M1 and M3 are listed in Table 5.9. These results were obtained by symmetric galerkin boundary element method (SGBEM) where E_o was 380 GPa and $\nu_o = 0.22$ using SUBC boundary conditions and volume averages for stress and strain. In order to compare the voids orientation and the variation of volume fractions of the models M1 and M3, Figure 5.11 shows how the MIL ellipses is coincided with void orientations. The MIL fabric tensor ellipses which shown in Figure 5.11 are the orientation of the ellipse relative to the x_1 axis can clearly be seen for M1 and M3.
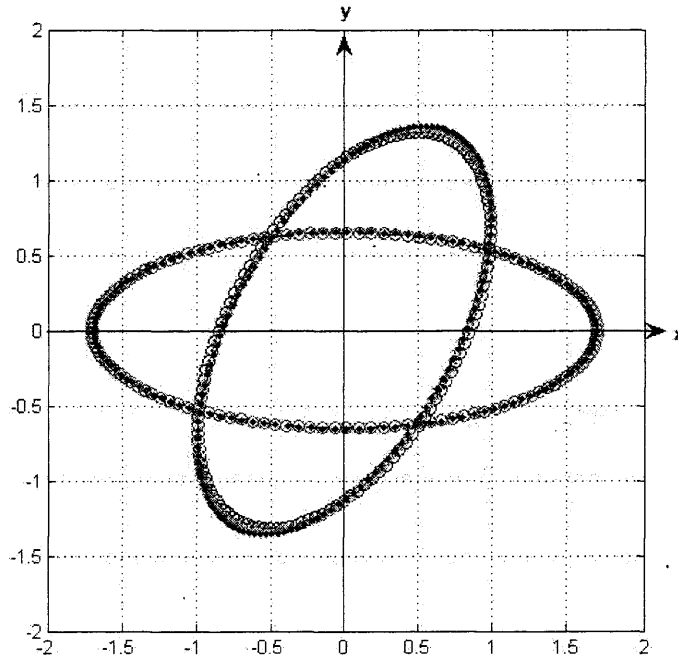
Figure 5.11: MIL ellipses for M1R1, M1R2, and M1R3 with M3R1, M3R2, and M3R3 show that the MIL ellipse orientation coincided with the voids orientation.

5.5   PZT Ceramics and Fabric Tensor Construction Methods

Here we construct three different fabric tensors for each PZT ceramic micrograph, PZT1 (irregular pore) and PZT2 (spherical pores). This procedure is to investigate the effect of the method of determination of fabric tensor (MIL, SVD, and SLD) on

78

the apparent elastic stiffness tensors. The fabric tensors for each of the PZT ceramic micrographs were constructed using these three method by the Quant3D commercial software. The symmetric Galerkin boundary element method and volume averaged stress and strain were also used to compare the stiffness tensors from each method. The PZT ceramic samples which were characterized in [75] are reanalyzed here.

Three fabric tensor construction methods (MIL, SVD, and SLD) were used to construct the fabric tensor for each sample, and then the eigenvalues were extracted and properly normalized as z_1 and z_2 for the two-dimensional analysis. For the two-dimensional problem studied here we assume $z_2 = z_3$ in order for $E_2 = E_3$, $\nu_{12} = \nu_{13}$ and $G_{12} = G_{13}$ from Eq.(2.30). Also, the eigenvectors corresponding to the fabric tensor eigenvalues were extracted from the image analysis, see Table 5.10. The eigenvectors are needed to know the orientation (θ) of the principal material axes relative to the (x, y) coordinates fixed by the boundaries of the micrograph. It is in the principal material axes where the relationships given by Eq. (2.30) are valid. It has been shown in previous studies [7], [69], [70] that the principal axes of the fabric tensor are coincident with the principal axes of the material.

As previously shown in Chapter 2, the PZT1 ceramic with irregular pores and PZT2 with spherical pores were discretized for analysis by SGBEM with three types of boundary conditions. When the volume averaged stresses and strains are computed from the boundary element analysis, using static uniform boundary condition, SUBC, a system of five equations (in two dimensions) can be formed and the four material properties needed to compute the apparent stiffness tensor can be obtained. Note that since we are calculating the apparent stiffness tensor in the principal material coordinates, we must first transform the stresses and strains used in the volume averaging to the principal material coordinates. This is straightforward since we know the rotation angle from the eigenvectors of the fabric tensor, and the tensor rotation can be performed using standard transformation methods. The results for

the elastic constants are shown in Table 5.11. Note in Table 5.11 that the elements of the apparent stiffness tensor of PZT1 and PZT2 are compared with the apparent stiffness tensor values obtained from volume averages calculations.

Table 5.10: MIL, SVD, and SLD fabric tensor eigenvalue and Zysset constants k, l for PZT1 and PZT2.

	MIL	SVD	SLD
PZT1			
z_1	1.0612	1.1681	1.2171
z_2	0.9687	0.9159	0.8915
θ^o	41.13	43.27	38.52
k	3.6621	3.7021	3.592
l	0.4395	0.2011	0.1590
PZT2			
z_1	1.0306	1.2201	1.0682
z_2	0.9847	0.8900	0.9659
θ^o	27.83	33.82	22.94
k	3.2851	3.4011	3.3980
l	0.5495	0.2201	0.6144

Table 5.11: Apparent elastic constants of PZT1 and PZT2 using MIL, SVD, SLD, and volume averaging methods.

	MIL (% Difference)	SVD (% Difference)	SLD (% Difference)	$\langle \sigma \varepsilon \rangle$
PZT1				
E_1	92.89 (2.74)	90.49 (2.44)	93.67 (0.98)	92.76
E_2	85.00 (2.41)	82.06 (3.81)	84.84 (0.55)	85.32
$G12$	35.85 (0.96)	35.31 (0.39)	36.53 (3.85)	35.18
PZT2				
E_1	100.67 (0.14)	104.78 (3.51)	104.24 (2.89)	101.31
E_2	94.36 (2.35)	91.27 (2.90)	92.11 (2.01)	94.01
$G12$	33.94 (3.68)	40.09 (2.81)	38.90 (2.97)	39.00

80

5.5.1 PZT Ceramics Fabric Analysis Results and Discussions

Having estimates of the apparent stiffness tensor as well as the eigenvalues of the fabric tensor using the three methods mentioned previously, we may now estimate the constants k, ℓ appearing in Eq. (2.30) for each method. Since the bulk material is assumed to be isotropic, we use $E_0 = 165$ GPa and $\nu_0 = 0.22$ [75]. The results are given in Table 5.11 where the SUBC boundary conditions results from volume averages calculations were used to perform a least-squares estimate for k, ℓ. Predictions for E_1 as a functions of v_s using Eq. (2.30) and the constants in Table 5.10 are shown in Figure 5.12 and Figure 5.13, respectively. These plots show an excellent agreement with experimental results for E_1 as was reported in [75] for each sample. The fabric ellipses for PZT1 and PZT2 using the three construction methods are shown in Figure 5.14 and Figure 5.15, respectively. From these plots we note that the ellipses are not in good agreement for the three methods. This will slightly affect the calculation of predicted apparent elastic constants which leads us to look for uncertainty in theses value and the its impact on our calculation. The errors and uncertainties in fabric tensor eigenvalues will be discussed in details in Chapter 6.
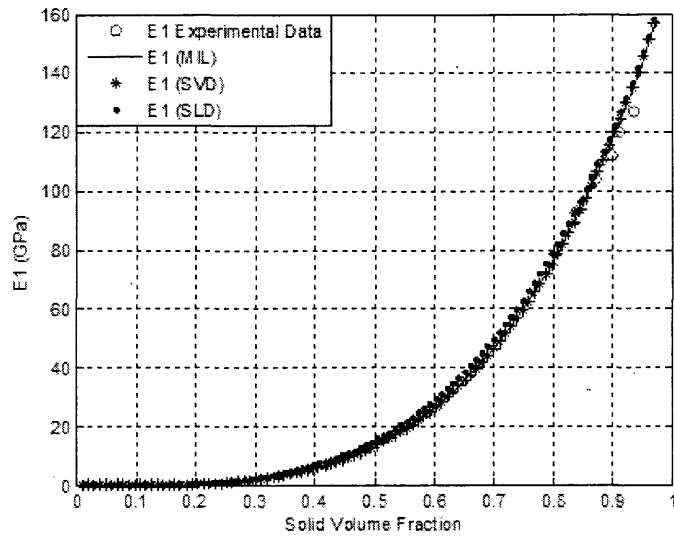
Figure 5.12: Variation of E_1 with volume fraction for PZT1 (irregular pores). The circles represent the experimentally measured values [75].
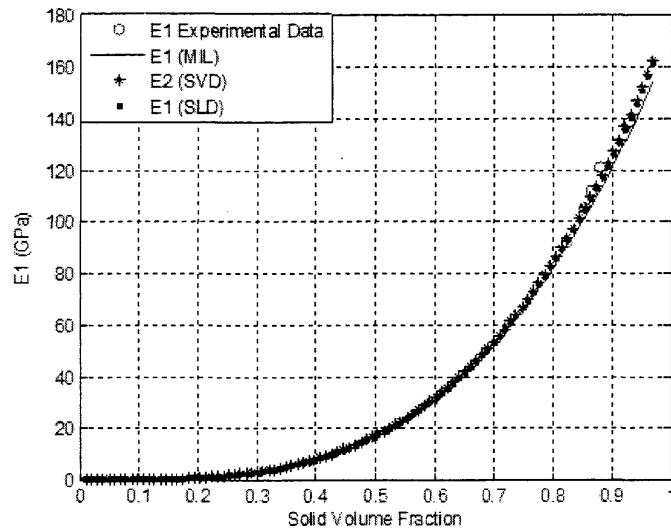
Figure 5.13: Variation of E_1 with volume fraction for PZT2 (spherical pores). The circles represent the experimentally measured values [75].
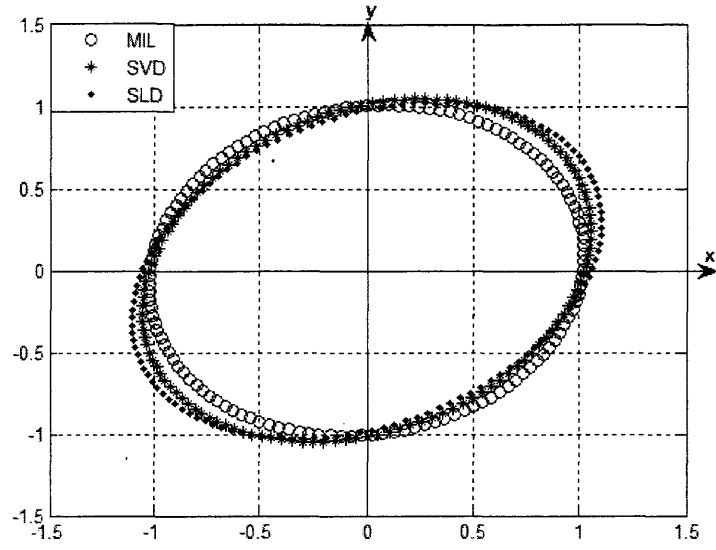
Figure 5.14: Fabric tensor ellipses for PZT2 from MIL, SVD, and SLD measurements.
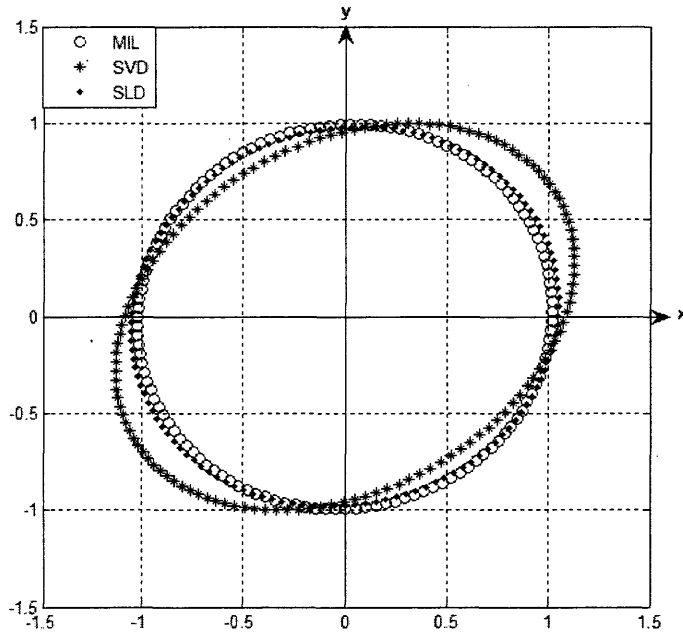
Figure 5.15: Fabric tensor ellipses for PZT1 from MIL, SVD, and SLD measurements.

83

CHAPTER 6

SENSITIVITY ANALYSIS OF FABRIC TENSORS AND APPARENT ELASTIC CONSTANTS

Regardless of precision and accuracy, every physical measurement is usually subject to a certain degree of uncertainty. This is caused by two factors, the bias (systematic) error, which is the limitation of the measuring instrument and the precision (random) error results from physical limitations of the analyst. In order to provide an accurate measurement of uncertainty, error propagation of the measurements is introduced and analyzed in this chapter. Error propagation is also known as the propagation of uncertainty and is defined as a calculus-derived statistical calculation designed to combine uncertainty from multiple variables or the effects on a function by a variable's uncertainty [75].

6.1 Precision and Bias Errors

All measurements are subjected to several different types of errors. Typically, all error and uncertainties in measurements are due to either precision (random) error or bias (systematic) errors. Some of these errors are made in calculations or in computer readings which are not considered in error analysis. Precision errors usually result from the human skills needed to measure and analyze under good conditions, and most often result from limitations in the tools or methods used to make a measurement. In contrast, bias errors are reproducible errors that are consistently in the same direction, and often due to a problem which persists throughout the entire process of measurand. Calibration of the machine being used, or incorrectly reading an instrument in the wrong way would cause a systematic error. These errors are statistical fluctuations in the measured data due to the accuracy limitations of the tool. In fact, working on limiting and reducing these error takes a lot of effort and time.

For bias error, the following terms are used to describe the quality of an instrument's readings [2]:

1. Accuracy. The difference between the measured and true value. The accuracy of a measurement is the closeness of agreement between the test result and the true value.

2. Precision. The difference between the instrument's reported values during repeated measurements of the same quantity. This value is determined by statistical analysis of repeated measurements.

3. Resolution. The smallest increment of change in the measured value from instrument.

4. Sensitivity. The change of an instrument's output per unit change in the measured quantity.
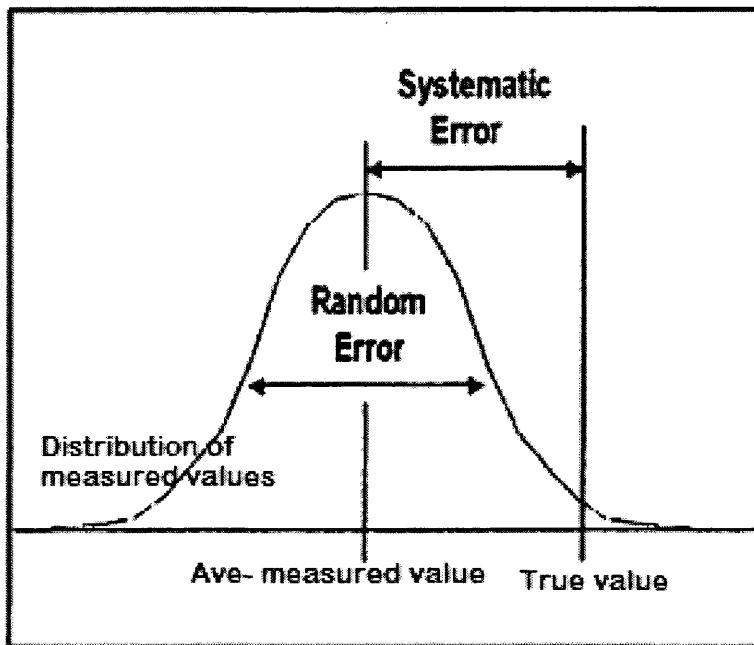
Figure 6.1: Precision and bias errors [68].

6.2 Uncertainty

The error in any measurement of a particular quantity is the difference between the measurement and the "true value" of this quantity. As previously mentioned, in uncertainty estimation we deal with two types of error, precision (random) and systematic error or bias, and two classes of experiments, single sample experiments and repeated sample experiments. A sample in this case refers to an individual measurement of specific quantity. The measurement uncertainty is composed of bias and precision errors. Bias error is a non-statistical, and precision errors are associated with random effects and are most commonly estimated using statistical techniques [75]. When we construct the fabric tensor (measurand) for a porous material several times, we have repeatedly sampled that particular fabric tensor. With such repeat sampling, we can, for example, statistically estimate the distribution of precision errors in the fabric tensor measurement. If we have only one measurement, our result does not reveal the distribution of the precision error. In that case, we must resort to other means for estimating the precision error in our result [2].

The remaining sections of this chapter are devoted to estimating precision errors in the fabric tensor for PZT ceramic. Procedures for statistical analysis of precision error in repeated sampled fabric tensor eigenvalues are determined. After determining the individual precision uncertainty in measurement of fabric tensor eigenvalues, we must combine them to obtain the total uncertainty U_z for each eigenvalue to calculate the uncertainty in the apparent elastic constants.

If we have both bias and precision error observed in the measurement process, then we must combine them to obtain the total uncertainty U_Z in our result for z_i as

$$U_z = (B_Z^2 + P_Z^2)^{0.5} \qquad (6.1)$$

where B_Z is the bias uncertainty and P_Z the precision uncertainty. Eq.(6.1) show that algebraically adding B_z and P_z gives an uncertainty that roughly covers 99% of

the data.

6.3 Theories Based on the Population and Sampling

Practically, we are able to analyze samples from which to extract statistical information. In most cases, it is impossible to analyze the whole population. Nevertheless, some useful results can be established at the outset by considering the properties of the entire population. If we have a big population of data, which is not the case here, each datum represents a measurement of a single quantity, and we assume each datum differs in magnitude from the rest only as a result of precision error. Effectively, each time a different number of the population is randomly selected and measured and has its own a precision error. The probability of getting a specific value of x depends on the magnitude of x, and the probability distribution of x-values is described by a probability density function (PDF), $f(x)$, which has a variety of shapes and could be determined by the nature of our data. For instance, the precision error is often distributed according to a curve given by Gaussian distribution or student t-distribution [2]. For an infinite population, the mathematical form for a Gaussian probability density function is

$$f(x) = \frac{1}{\sigma\sqrt{2\pi}} e^{-\frac{(x-\mu)^2}{2\sigma^2}} \tag{6.2}$$

where x is the magnitude of a particular measurement, μ is the mean value of the entire population, and σ the standard deviation of the entire population.

6.4 Statistics to Estimate Random Uncertainty

In any numerical calculation, we deal with samples from a population and note that the data do not always abide by a Gaussian distribution. If not, like in our case here, we must use another method, such as the student t-distribution. Basically, in this method we are looking to use average values from the sample to estimate the

87

mean or standard deviation. Thus, If a large number of measurements are taken with equal care, then the average (true value) of these n measurements, $\bar{x}$, is

$$\bar{x} = \sum_{i=1}^{n} \frac{x_i}{n}, \tag{6.3}$$

and the standard deviation of the population, S_x is given by,

$$S_x = \sqrt{\frac{(x_1 - \bar{x})^2 + (x_2 - \bar{x})^2 + ... + (x_n - \bar{x})^2}{n-1}} = \sqrt{\frac{1}{v}[\Sigma_{i=1}^{n} x_i^2 - n\bar{x}^2]} \tag{6.4}$$

where $v = (n - 1)$ is the degrees of freedom.

In general, the Gaussian distribution method is used for large sampling and the student t-distribution is used for small sampling. Confidence intervals can be determine for each method. The ASME/ANSI standard on uncertainty calls for specification of the precision error in x by

$$P_x = t\frac{S_x}{\sqrt{n}}(c\%) \tag{6.5}$$

where t depends on the degrees of freedom in calculating S_x and confident interval assigned. An important aspect of this methodology, is that the degrees of freedom associated with cited estimates of precision should be calculated and quoted. This becomes important when the number of degrees of freedom in the result is small, so that error limits and propagated errors have student t-distribution not Gaussian error distribution. Even if it is assumed that the individual measurements are distributed according to a Gaussian distribution, the true standard deviation for an average of n samples, $\bar{x}$, is not known and must be calculated from the data [2].

The appropriate distribution for small population data is the student t-distribution. The difference between the Gaussian and student t-distributions is generally not important when the number of degrees of freedom exceeds about thirty, but for small data sizes the differences can be very significant [62].

Procedure

1. Determine the mean value, $\bar{x}$, and the standard deviation estimation, S_x, for n measurements.

2. Determine the t-value from tables for $t_{\alpha,v}$, $(v = 1 - (c/100))$ (for a given c in % where c is the confidence).

3. Form the confidence intervals (note with upper and lower bounds): $\pm t_{\alpha,v} \cdot \frac{S_x}{\sqrt{n}}$

Typically, we'd like to have some guarantee $\bar{x}$ and S_x accurately approximate the corresponding values for the population and to infer the probability distribution of the population from that of the sample. For small samples (n < 30) knowledge of distribution is assumed in estimating the uncertainty of $\bar{x}$. [75] provides tables and details on the statistical analysis by using Gaussian and Student-t distribution.

6.4.1 Student t-distribution (small sample sizes)

The student t-distribution or was formulated by W.S. Gosset, a scientist in the Guinness brewery in Ireland, who published his formulation in 1908 under the pen name (pseudonym) "Student". The student t-distribution can be defined as being the distribution of the random variable, t, defined as

$$t = \frac{(\bar{x} - \mu)}{S_x/\sqrt{n}} \tag{6.6}$$

where $\bar{x}$ is the sample mean, μ is the population mean, S_x is the standard deviation of the sample, and n is the sample size. The distribution of the t statistic is called the t-distribution or the student t-distribution. In other words, suppose we have a simple random sample of size n drawn from a normal population with mean $\bar{x}$ and standard deviation S_x. Then the quantity has a t distribution with $n - 1$ degrees of freedom.

Note that there is a different t distribution for each sample size. When we speak of a specific t distribution, we have to specify the degrees of freedom v. The degrees of freedom for this t statistic comes from the sample standard deviation S_x in the denominator of Eq.(6.8).

The t distribution curves are symmetrical and bell-shaped like the normal distribution and have their peak at 0, see Figure 6.2. However, the wings of the curve are more flat than that of the standard normal distribution shape. Consequently, since S_x is a random quantity varying with various samples, the variability in t is more, resulting in a more spread. As the degree of freedom become large, the t-distribution approaches the Gaussian (normal) distribution.
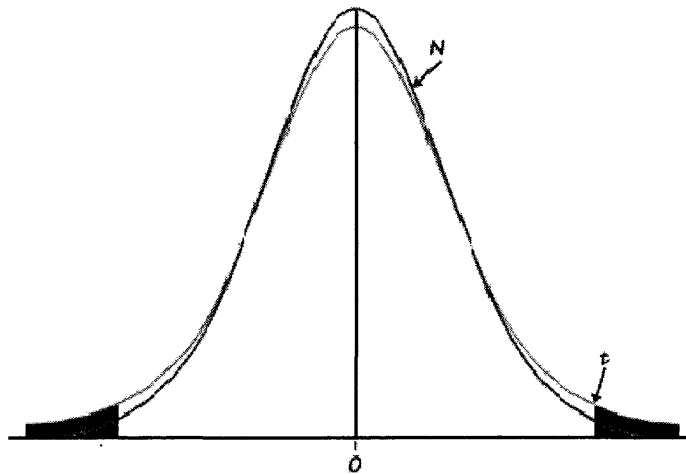
Figure 6.2: Comparing a student $t-$distribution with the standard normal distribution N [42].

Moreover, since the t-distribution is a PDF, the probability that t will lie in interval $t_2 - t_1$ is equal to the area beneath the curve α between t_2 and t_1. For $n > 30$, the two distributions are the same. For simplicity, the area under the t-distribution is tabulated in tables, for instance, see [2]. Since the t-distribution is symmetric, and we want a two-sided confidence interval with confidence $c\%$, the lower and upper bounds on the mean are determined. The true mean value lies in the interval

$$\bar{x} - t_{\alpha/2,v}\frac{S_x}{\sqrt{n}} < \mu < \bar{x} + t_{\alpha/2,v}\frac{S_x}{\sqrt{n}} \qquad (c\%) \qquad (6.7)$$

where $\alpha = 1 - c$ is the level of significance and $v = n - 1$. At proper confidence level $c\%$, this confidence interval defines the precision uncertainty in the value $\bar{x}$ as

$$P_x = t_{\alpha/2,v}\frac{S_x}{\sqrt{n}} \qquad (c\%) \qquad (6.8)$$

This precision uncertainty is what we need in Eq. (6.1) for the total uncertainty U_Z.

6.4.2 Propagation of Error and Uncertainty

Normally, not all uncertainties are small or equal. Therefore, the evaluation of the uncertainty in engineering measurements is a task that cannot be neglected. Consequently, the ability to properly combine uncertainties from different measurements is not an easy task. Error propagation in numerical values comes in diverse ways: input data, different observers, sample differences, etc. For uncertainties in the independent variables, the procedure rests on a statistical theorem that is exact for a linear function y of several independent variables x_i with standard deviation σ_i. Basically, the standard deviation of a measurement gives the sense of the error and the theorem of propagation of uncertainty states that the standard deviation of y is

$$\sigma_y = \sqrt{(\frac{\partial y}{\partial x_1}\sigma_1)^2 + (\frac{\partial y}{\partial x_2}\sigma_2)^2 + \ldots + (\frac{\partial y}{\partial x_n}\sigma_n)^2} \qquad (6.9)$$

In the same way, we may consider y as a function of several independent measured variables, $x_1, x_2, ..., x_n$. For example, in this dissertation we use a model for the elastic constants which are defined as a function of the fabric tensor eigenvalues z_1 and z_2. Each measured variable has an some uncertainty, u_1, u_2, u_3 and these uncertainties lead to uncertainty in y which we call U_y. To estimate U_y, we assume that the relative uncertainty in each quantity is small so that a first order Taylor expansion of

$y(x_1, x_2, ..., x_n)$ provides a good approximation,

$$y(x_1 + u_1, x_2 + u_2, ..., x_n + u_n) = y(x_1, x_2, ..., x_n) + \frac{\partial y}{\partial x_1} u_1 \frac{\partial y}{\partial x_1} u_2 + ... + \frac{\partial y}{\partial x_n} u_n$$
$$(6.10)$$

Under this approximation, y is a linear function of the independent variables. Now we can apply the theorem, assuming that uncertainties will behave much like standard deviations,

$$U_y = \sqrt{(\frac{\partial y}{\partial x_1} u_1)^2 + (\frac{\partial y}{\partial x_2} u_2)^2 + ... + (\frac{\partial y}{\partial x_n} u_n)^2} \qquad (6.11)$$

As mentioned previously, the uncertainties u_i may be either bias or precision uncertainties. The estimation of uncertainty is obtained by assuming each of the measurements was made under the same conditions, is independent, and the distribution from each measurement follows a t-distribution. In this way, the actual uncertainty is computed like a sample standard deviation.[2]. Eq.(6.11) can be simplified when y has certain common functional forms as in the Zysset model, Eq.(2.30), that we used in this dissertation.

6.5 Sensitivity of Elastic Constants of PZT Ceramics to Fabric Tensors

The relationships between the stiffness and fabric tensors has been established using two different approaches, Cowin [7] and Zysset [77]. This dissertation has used the relationship derived by Zysset [77] to predict the relation between the elastic constants and fabric tensor eigenvalues. Here we also use this relation to determine the uncertainties in elastic stiffness of the PZT ceramics. The Zysset relations, presented earlier in this dissertation, are

$$E_i = E_0 v_s^k z_i^{2\ell} \qquad (6.12)$$
$$\nu_{ij} = \nu_0 \left(\frac{z_j}{z_i} \right)^\ell$$
$$G_{ij} = G_0 v_s^k z_i^\ell z_j^\ell$$

The uncertainties in z_1 and z_2 for each sample are calculated by using the student t-distribution. We then determine the uncertainties in E_2, and E_2, from Eq.(6.11) as

$$U_{E_1} = \sqrt{\left(\frac{\partial E_1}{\partial z_1}U_{z_1}\right)^2} = |\frac{\partial E_1}{\partial z_1}U_{z_1}| \tag{6.13}$$

$$\cdot \; U_{E_2} = \sqrt{\left(\frac{\partial E_2}{\partial z_2}U_{z_2}\right)^2} = |\frac{\partial E_2}{\partial z_2}U_{z_2}|$$

where U_{z_1}, and U_{z_2} are the uncertainties in z_1, z_2, respectively. and

$$\frac{\partial E_1}{\partial z_1} = E_0 v_s^k (2\ell) z_1^{2\ell-1} \tag{6.14}$$

$$\frac{\partial E_2}{\partial z_2} = E_0 v_s^k (2\ell) z_2^{2\ell-1}.$$

The uncertainty in Poisson's ratio ν_{12} is given by

$$U_{\nu_{12}} = \sqrt{\left(\frac{\partial \nu_{12}}{\partial z_1}U_{z_1}\right)^2 + \left(\frac{\partial \nu_{12}}{\partial z_2}U_{z_2}\right)^2} \tag{6.15}$$

where

$$\frac{\partial \nu_{12}}{\partial z_1} = \nu_0 z_2^\ell z_1^{\ell-1} \tag{6.16}$$

$$\frac{\partial \nu_{12}}{\partial z_2} = \nu_0 z_1^\ell z_2^{\ell-1}$$

The uncertainty in shear modulus G_{ij} is calculated from

$$U_{G_{12}} = \sqrt{\left(\frac{\partial G_{12}}{\partial z_1}U_{z_1}\right)^2 + \left(\frac{\partial G_{12}}{\partial z_2}U_{z_2}\right)^2} \tag{6.17}$$

where

93

$$\frac{\partial G_{12}}{\partial z_1} = G_0 v_s^k \ell z_2^\ell z_1^{\ell-1} \tag{6.18}$$

$$\frac{\partial G_{12}}{\partial z_2} = G_0 v_s^k \ell z_1^\ell z_2^{\ell-1}$$

6.6 Uncertainty Results and Discussion

There are two approaches in determining the uncertainty in fabric tensor eigenvalues U_Z, of PZT ceramics. For the first case we consider the construction of the fabric tensor by using only the mean intercept length (MIL). This process of constructing the MIL was conducted multiple times to obtain 25 measurements for each PZT ceramic micrograph, see Table 6.1 and Table 6.2. Here, only precision error is considered. The precision error in the fabric tensor eigenvalues can be averaged to find a 95% confidence interval. The standard deviation S_x and mean value $\bar{x}$ were calculated. To find the uncertainty in this mean value $\bar{x}$, the precision uncertainty must be estimated using the student t-distribution. From student t-distribution tables [2] with a degree of freedom, $v = 25 - 1 = 24$ and $\alpha = (1 - 0.95)/2 = 0.025$, we obtain $t_{\alpha,v} = t_{0.025,24} = 2.064$. Applying Eq.(6.7) and Eq.(6.8) we then calculate the uncertainty in each of the fabric tensor eigenvalues see Table 6.3 for PZT1 and PZT2. Finally, we use Eq. (6.13) to Eq. (6.17) to determine the uncertainty in the elatic constants of PZT ceramics. These values are also reported in Table 6.3.

From Table 6.3, we note that the uncertainties in fabric tensor eigenvalues of PZT2 is higher than PZT1. Also the uncertainties in the fabric tensor eigenvalues z_1 for the two samples is larger than z_2 uncertainty. The uncertainties in Young's module E_1 in both PZT ceramics are the higher, where the uncertainty in Poisson ratio ν_{12} is the smallest.

Table 6.1: z_1 and z_2 for PZT1 Ceramic Using MIL Method and Calculation of Mean and Standard Deviation.

Number of reading	z_1	z_2
PZT1		
1	1.0612	0.9687
2	1.0626	0.9687
3	1.0617	0.9692
4	1.0681	0.9659
5	1.0688	0.9656
6	1.0419	0.9790
7	1.0411	0.9795
8	1.0407	0.9797
9	1.1246	0.9377
10	1.1199	0.9401
11	1.1139	0.9431
12	1.1819	0.9091
13	1.1009	0.9495
14	1.1860	0.9070
15	1.0615	0.9699
16	1.0817	0.9591
17	1.0897	0.9552
18	1.0000	1.0000
19	1.1443	0.9278
20	1.1754	0.9123
21	1.2235	0.8883
22	1.2097	0.8951
23	1.2498	0.8751
24	1.1411	0.9295
25	1.6161	0.6919
Mean $\bar{x}$	1.1306	0.9347
Standard Deviation S_x	0.1201	0.0600

Table 6.2: z_1 and z_2 Data for PZT2 Ceramic Using MIL Method and Calculation of Mean and Standard Deviation.

Number of reading	z_1	z_2
PZT2		
1	1.0306	0.9847
2	1.0317	0.9841
3	1.0617	0.9756
4	1.0623	0.9688
5	1.1720	0.9140
6	1.1379	0.9311
7	1.0101	0.9949
8	1.0064	0.9968
9	1.0150	0.9925
10	1.0614	0.9693
11	1.1091	0.9454
12	1.1177	0.9411
13	1.1491	0.9254
14	1.0733	0.9634
15	1.0081	0.9960
16	1.0092	0.9954
17	1.0752	0.9624
18	1.0000	1.0000
19	1.0695	0.9652
20	1.0948	0.9526
21	1.0874	0.9563
22	1.1022	0.9489
23	1.1228	0.9386
24	1.1434	0.9283
25	1.0926	0.9537
Mean $\bar{x}$	1.0737	0.9634
Standard Deviation S_x	0.0507	0.0255

Table 6.3: Calculation of elastic constants uncertainties with $E_o = 165$ GPa, $\nu_o = 0.22$, and $t_{\alpha/2,v} = 2.064$.

	$\bar{x}$	S_x	$t_{\alpha/2,v}$	U_Z	U_{E_1}	U_{E_2}	$U_{G_{12}}$	$U_{\nu_{12}}$
PZT1								
z_1	1.1306	0.1201	2.064	0.0496	3.7031	1.8723	0.8312	0.0119
z_2	0.9347	0.0600	2.064	0.0248				
PZT2								
z_1	1.0737	0.0507	2.064	1.1063	2.2582	1.1284	0.5098	0.0051
z_2	0.9634	0.0255	2.064	0.9469				

96

We next consider uncertainties in the fabric tensor eigenvalues constructed for each PZT ceramic using the three methods were employed in Chapter 2 (MIL, SVD, SLD). As we have done before, the uncertainties in each of the elastic constants are calculated based on the uncertainties of the eigenvalues from each method. To find the uncertainty in the mean value, the precision uncertainty must be estimated using the student t-distribution because of the small sample data. From the student t-distribution table [2] with a degree of freedom $v = 3 - 1 = 2$ and $\alpha = (1 - 0.95)/2 = 0.025$, we obtain $t_{\alpha,v} = t_{0.025,2} = 4.303$. Applying Eq.(6.7) and Eq.(6.8) again, the calculation of the uncertainties in each of the fabric tensor eigenvalues and the elastic constants are listed in Table 6.4 and Table 6.5, respectively, for both PZT1 and PT2 samples.

Table 6.4: Calculation of the eigenvalue uncertainties using MIL, SVD, and SLD.

	MIL	SVD	SLD	$\bar{x}$	S_x	U_z
PZT1						
Z_1	1.0612	1.1681	1.2171	1.1488	0.0797	0.1981
Z_2	0.9687	0.9159	0.8915	0.9254	0.0395	0.0980
PZT2						
Z_1	1.0306	1.2201	1.0682	1.1063	0.1003	0.2493
Z_2	0.9847	0.8900	0.9659	0.9469	0.0501	0.1246

Table 6.5: Calculation of elastic constants uncertainties with $E_o = 380$ GPa, $\nu_o = 0.22$, and $t_{\alpha/2,v} = 4.303$.

	MIL	SVD	SLD	U_z	U_{E_1}	U_{E_2}	$U_{G_{12}}$	$U_{\nu_{12}}$
PZT1								
Z_1	1.0612	1.1681	1.2171	0.1981	6.4522	3.6345	1.4894	0.0451
Z_2	0.9687	0.9159	0.8915	0.0980				
PZT2								
Z_1	1.0306	1.2201	1.0682	0.2493	9.9625	5.4316	2.2844	0.0580
Z_2	0.9847	0.8900	0.9659	0.1246				

Results listed in Table 6.4 present the uncertainties in fabric tensor eigenvalues as well as in the elastic moduli of the PZT ceramics. The uncertainties in the fabric tensor eigenvalues z_1 for the two samples is larger than z_2 uncertainty. Where, the

97

uncertainties in the fabric tensor eigenvalues of PZT2 are bigger than PZT1. Also, for both PZT ceramics, this table shows that the Young's modulus E_1 has the highest uncertainty, where the uncertainty in Poisson ratio ν_{12} is the smallest.

The presented treatment of uncertainty in the PZT ceramic properties is of equal importance to the engineering industries and material applications. We have presented a framework for quantifying uncertainty in apparent elastic properties of PZT ceramic, estimated with the multiple measurements of fabric tensor. The presented results shows that we should increase the number of specimens used in the fabric tensor measurements to achieve the requested confidence level. This will provide in one hand insight to the designers and certification bodies on the quality of the measurements on material properties, irrespective of whether these are related to stiffness or strength issues. On the other hand, thorough examination of the uncertainty introduced in the apparent properties following specific test procedures, will lead to an improvement of the test procedures applicable to a wide range of porous solid [41].

6.7 Conclusion

To identify the errors and the uncertainties for our fabric tensor measurement, the concept of uncertainty have been reviewed and two techniques for estimating the propagation of uncertainty are presented. Basically, the two methods described here are not the only techniques available, but they are the most widely used. The measurement uncertainty may not be commonly applied as it should be in numerical and experimental investigations. A general review of student t-distribution is made of our data to determine the uncertainty in the numerical results. For the sake of simplicity, only precision error is considered and the difference between uncertainties in the model, micrographs, or in computer simulations are ignored. The main objective from this chapter is an appreciation for the term used in specifying expected errors for model, micrographs, calculations, etc. In particular, the uncertainty in

fabric tensor eigenvalues of PZT ceramic models were calculated, and consequently, the uncertainty in the apparent elastic constant is determined using two approaches.

CHAPTER 7

CONCLUSIONS AND SUGGESTION OF FUTURE WORK

Concluding remarks on numerical homogenization, symmetric Galerkin boundary element method, and the fabric tensor approach are presented in this Chapter. After presenting our conclusions, we present a several ideas for future research topics in this area.

7.1 Conclusions

The study performed in this dissertation establishes a numerical process for modeling of porous materials utilizing the boundary element method and a fabric tensor approach. Here, we evaluate the effectiveness of our approach for single-phase, voided materials. We summarize our conclusions for analysis: homogenization theory, fabric tensor descriptor methods and measurements error, in the following paragraphs.

- *Homogenization theory.* With such an approach, a representative volume element (RVE) is sought which is representative of the material behavior including microstructural features that may affect the stress analysis. Here, we used the RVE approach and extracted the *effective* elastic constants from numerical experiments, where the elastic constants related to volume averages of stress and strain. In some engineering problems, its impossible to identify a material RVE, or the size of the RVE may be far too large in comparison to the mechanical component under consideration. For this reason we constructed a volume element (VE) which is smaller than RVE to determine *apparent* elastic constants for porous solids. The dependence of apparent elastic constants on the boundary condition imposed are proved numerically. The apparent elastic constants are varied with the position of the volume element in the porous structure. Consequently, we compute the apparent elastic constants in such a way that the Hill

criterion is satisfied through appropriate choices of the boundary conditions.

In terms of boundary condition, three types of boundary conditions were imposed on the RVE, namely: displacement uniform boundary conditions (KUBC), static uniform boundary conditions (SUBC), and mixed boundary conditions (MUBC). A comprehensive study has been performed on the impact of these types of boundary conditions on the effective and apparent elastic stiffness tensors of the porous solids. The boundary conditions which satisfy the Hill criterion, are imposed on volume elements to extract the elastic properties of heterogeneous materials through the concept of homogenization. To satisfy the ergodicity assumption, we assumed that elastic properties extracted from the volume averages of stress and strain on the volume elements can be taken as the overall properties of the homogenized material.

Boundary integral equations needed for the calculation of volume averages of stress and strain were easily evaluated using boundary values from the boundary element analysis. Overall, the apparent stiffness tensors for mixed boundary conditions is shown to fall between the apparent tensors associated with the static and kinematic uniform conditions. Finally, we observed that as the size of volume element increases, the differences between apparent properties under different kinds of boundary conditions decreases.

- *Fabric tensor and materials elastic stiffness tensor.* We use the concept of a fabric tensor to predict the elastic constants of porous materials. The elastic constants could be found through the volume fraction and the fabric tensor eigenvalues. This allowed us to predict the variation of the elastic stiffness tensor as a function of the solid volume fraction, v_s. For the porous solids considered in this dissertation, the fabric tensors were constructed from mean intercept lengths (MIL), star-volume distribution (SVD), and the star-length distribution

101

(SLD). In this approach, high resolution imaging software, Quant3D, provides the fabric measurements from 2D gray scale images of the material. We investigated the impact of the fabric tensor construction method on predictions of elastic constants in both idealized and actual materials. Despite some error in the measurements, these methods do not impact the prediction of elastic constants in a systematic way.

- *Measurements Error.* In this part of the dissertation we investigated the uncertainty in elastic properties of porous materials which resulted from the error in estimation of fabric tensors. The uncertainties in fabric tensor eigenvalues calculated using the student t-distribution method. We found that the uncertainties in fabric tensor measurements leads to some errors in prediction of stiffness tensor. These errors are very small relative errors in the elastic constants. The uncertainties in Young's moduli are slightly greater than uncertainties in other elastic constants because of the uncertainty in eigenvalue z_1 is bigger than z_2 in both samples .

7.2 Suggestion for Future Work

The results reported here have validated the concept of homogenization based on the fabric tensor and has laid a foundation for continued research based on this approach. Here, a number of possible suggestions for future investigations are proposed.

7.2.1 Strength of Porous Materials

For structural and load-carrying applications, every material has a certain strength in terms of stress or strain. To calculate material strength, we should calculate the stresses/strains in the material principal directions which can be done by transformation of stresses from the global coordinates (from SGBEM) to local material coordinates as

$$\{\sigma\}_{x-y} = [T_\sigma]\{\sigma\}_{1-2} \quad or \quad \{\sigma\}_{1-2} = [T_\sigma]^{-1}\{\sigma\}_{x-y} \tag{7.1}$$
$$\{\varepsilon\}_{1-2} = [Q]_{1-2}\{\sigma\}_{1-2}$$

where T and Q are transformation matrices. By this we can apply the failure criteria in the material coordinate system. There are several theories of failure applied to anisotropic materials such as Tsai-Hill, and Tsai-Wu failure criterion. To apply these theories, biaxial testing is needed in addition to uniaxial testing which is achievable using SGBEM. In 2D principal stress space, an example of the Tsai-Wu failure envelope is shown in Figure 7.1.

It is necessary to deduce the proper scale for the corresponding idealization of homogeneity for materials failure problems. Failure criteria and strength characteristics of porous materials in light of the failure mechanisms could be a new area of research based on a material's fabric tensor.
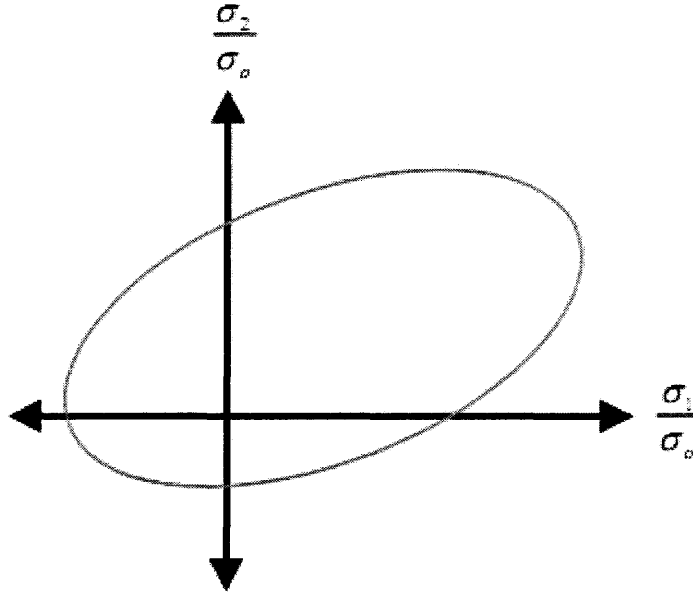
Figure 7.1: Tsai-Wu failure envelope [4].

103

7.2.2 3D Fabric Elasticity Relations

The fabric is a measure used to describe and characterize a material's anisotropy within a representative volume element through quantitative microstructural measurements. The second-rank fabric fabric tensor can be best viewed as a term in a tensorial series representation of an orientation distribution function. In this study, the fabric tensor was viewed as a quantitative measure of the structural anisotropy in porous solid utilizing SGBEM in two dimensional analysis. But, there was no investigations or analysis for three dimensional micrographs (Figure 7.2). Numerical modeling by boundary element analysis and the fabric tensor in three dimensions remains to be investigated for three dimensional porous structures. In boundary element meshing, three-dimensional boundary elements can either be flat sided or curved, and are generally triangles or quadrilaterals (Figure 7.2).
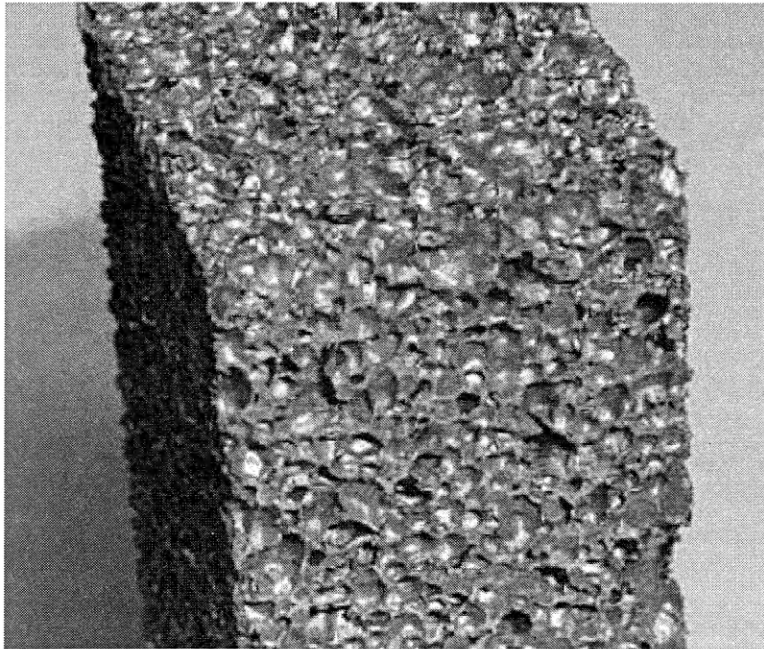
Figure 7.2: 3D metallic foam micrograph [4].

7.2.3   Fracture Mechanics of Porous Solids Using Fabric Tensor

In Chapter 5, the pore size distribution and aspect ratio in the structure was characterized in detail. We decreased the aspect ratio of the circular pore to $(a/b = 0.1)$, where a and b are the short axis and long axis length of the elliptical pores, respectively. But, if we keep decreasing the aspect ratio the pores will converted to cracks inside the structure Figure 7.3. A crucial component for analyzing crack extension is the ability to predict the crack initiation, stress intensity factor (fracture toughness) and crack path. SGBEM is an excellent method to investigate the properties of fracture initiation and propagation (Figure 7.4).
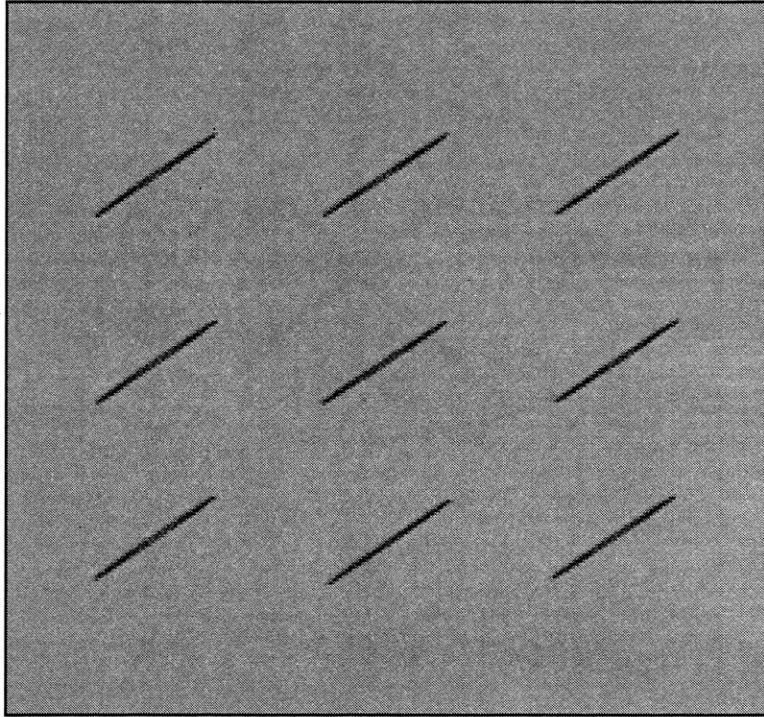
Figure 7.3: Model used in this work with pore converted to cracks.

The literature is rich in new developments in the composite and porous solids technology. But damage mechanics in single-phase porous materials is a rather complex problem that has challenged researchers during the past few decades. More research is needed for a comprehensive understanding of porous media failure processes under

different loading conditions.
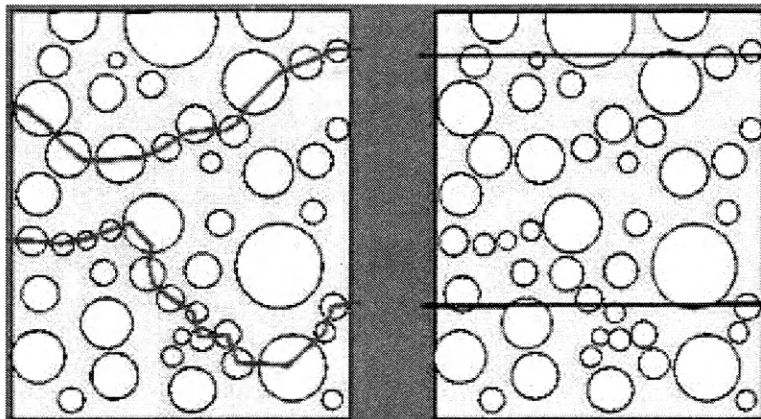
Figure 7.4: Example of fracture paths in porous structure [15].

REFERENCES CITED

[1] M. H. ALIABADI, *The Boundary Element Method, Applications in Solids and Structures*, Chichester [u.a.]: Wiley, 2002.

[2] G. T. BECKWITH, R. D. Marangoni, and J. H. LIENHARD, *Mechanichal Measurements*, Pearson Prentice Hall Publisher, 2007.

[3] J. R. BERGER, Fabric tensor based boundary element analysis of porous solids, *Engineering Analysis with Boundary Elements*, **35**: 430-435, 2011.

[4] C. A. BREBBIA and J. DOMINGUEZ, *Boundary Element An Introductory Course 2nd ed*, 1992.

[5] C. V. CAMP and G. S. GIPSON, Overhauser elements in boundary element analysis, *Journal of Materials Science*, **15**: 59-69, 1991.

[6] Concept Analyst. http://www.conceptanalyst.com/technical.htm, 1997.

[7] S. C. COWIN, The relationship between the elasticity tensor and the fabric tensor, *Mechanics of Materials*, **4**: 137-147, 1985.

[8] T. A. CRUSE, *Boundary Element Analysis in Computational Fracture Mechanics*. Kluwer: Dordrecht, 1988.

[9] T. A. CRUSE, Numerical Solutions in Three-Dimensional Elastostatics, *International Journal of Solids Structures*, **5**: 1259-1274, 1969.

[10] L. M. CRUZ-ORIVE, L. M. KARLSSON, S. E. LARSEN, and F. WAINSCHTEIN, Characterizing anisotropy: a new concept, *Micron and Microscopia Acta*, **23**: 75-76, 1992.

[11] F. EL HOUDAIGUI, S. FOREST, A.-F. GOURGUES, and D. JEULIN, On the size of the representative volume for isotropic elastic polycrystalline copper, *Yilong Bai (eds) IUTAM Symposium on Mechnical Behavior and Micromechanics of nanostructured materials*, **12**: 171-180, 2005.

[12] B. ELMABROUK, J. R. BERGER, L. J. GRAY, and A.-V. PHAN, Apparent Stiffness Tensors for Porous Solids using Symmetric Galerkin Boundary Elements, *Computational Mechanics*, DOI:10.1007/s00466-011-0650-1, 2011.

[13] B. Elmabrouk, and J. R. Berger, Boundary Element Analysis for Effective Stiffness Tensors: Effect of Fabric Tensor Determination Method, *Computational Mechanics*, (**in review**), 2012.

[14] N. I. Fisher, T. L. Lewis, and B. J. Embleton , Statistical analysis of spherical data, *Cambridge, U. K. Press Cambridge, U.K*, 1987.

[15] Foods under the microscope. `http://www.magma.ca/~scimat/foodmicr.htm`, Feb 2. 2009.

[16] A. Frangi, Regularization of boundary element formulations by the derivative transfer method. In eds. V. Sladek and J. Sladek, *Singular Integrals in the Boundary Element Method*, Advances in Boundary Elements, chapter 4, pp. 125–164. Computational Mechanics Publishers, 1998.

[17] L. J. Gibson and M. F. Ashby, *Cellular Solids: Structure and Properties*, Second Edition, Cambridge Solid State Science Series, Cambridge University Press, Cambridge, United Kingdom, 1999.

[18] L. J. Gray, Evaluation of singular and hypersingular Galerkin boundary integrals: direct limits and symbolic computation. In eds. V. Sladek and J. Sladek, *Singular Integrals in the Boundary Element Method*, Advances in Boundary Elements, chapter 2, pp. 33–84. Computational Mechanics Publishers, 1998.

[19] L. J. Gray, J. Glaeser, and T. Kaplan, Direct evaluation of hypersingular Galerkin surface integrals, *SIAM Journal of Scientific Computing* **25**: 1534–1556, 2004.

[20] L. J. Gray and G. H. Paulino, Symmetric Galerkin boundary integral fracture analysis for plane orthotropic elasticity, *Journal of Materials Science*, **20(1/2)**: 26-33, 1997.

[21] David Gregory and Debbie Marshall, Creative Commons by-nc-nd 2.0 UK, `Images.wellcome.ac.uk/indexplus/page/Prices.html`, 2011.

[22] T. P. Harrigan and R. W. Mann, Characterization of microstructural anisotropy in orthotropic materials using a second rank tensor, *Journal of Materials Science*, **19**: 761-767, 1984.

[23] F. Hartmann, C. Katz, and B. Protopsaltis, Boundary elements and symmetry, *Ingenieur-Archiv.* **55**: 440–449, 1985.

[24] Z. HASHIN, On elastic behaviour of fibre reinforced materials of arbitrary transverse phase geometry, *Journal of the Mechanics and Physics of Solids*, **13**: 119-134, 1965.

[25] Z. HASHIN and S. SHTRIKMAN, A variational approach to the theory of the elastic behaviour of multiphase materials, *Journal of the Mechanics and Physics of Solids*, **11**: (2) 127-140, 1963.

[26] S. HAZANOV and C. HUET, Order relationships for boundary conditions effect in heterogeneous bodies smaller than the representative volume, *Journal of the Mechanics and Physics of Solids*, **42**: 1995–2011, 1994.

[27] S. HAZANOV and M. AMIEUR, On overall properties of elastic heterogeneous bodies smaller than the representative volume, *International Journal of Engineering Science*, **33**: 1289–1301, 1995.

[28] R. HILL, Elastic properties of reinforced solids: some theoretical principles, *Journal of the Mechanics and Physics of Solids*, **11**: 357–372, 1963.

[29] S. J. HOLLISTER, and N. KIKUCHI, A comparison of homogenization and standard mechanics analyses for periodic porous composites, *Computational Mechanics*, **10**: 73–95, 1992.

[30] HRXCT Quantitation Software. http://www.ctlab.geo.utexas.edu/software/index.php, May 22. 2005.

[31] C. HUET, Application of variational concepts to size effects in elastic heterogeneous bodies, *Journal of the Mechanics and Physics of Solids* **38**: 813–841, 1990.

[32] C. HUET, Coupled size and boundary-condition effects in viscoelastic heterogeneous and composite bodies, *Journal of Mechanics of Materials*, **31**: 787-829, 1999.

[33] D. INGLIS, and S. PIETRUSZCZAK, Characterization of anisotropy in porous media by means of linear intercept measurements, *International Journal of Solids and Structure*, **40**: 1243-1261, 2003.

[34] MARK KACHANOV and IGOR SEVOSTIANOV, On quantitative characterization of microstructuresand effective properties; *Journal of Materials Science*, **42**: 309-336, 2005.

[35] K. KANATANI, Distribution of directional data and fabric tensors, *International Journal of Engineering Science*, **22**: 149-164, 1984.

[36] R. A. KETCHAM, Three-dimensional grain fabric measurements using high-resolution X-ray computed tomography, *Journal of Structural Geology*, **27**: 1217-1228, 2005.

[37] R. A. KETCHAM and T. M. RYAN, Quantification and visualization of anisotropy in trabecular bone, *Journal of Microscopy*, **22**: 158-171, 2004.

[38] M. KINZL, A. BOGER, P. K. ZYSSET, and D. H. PAHR, The effects of bone and pore volume fraction on the mechanical properties of PMMA/bone biopsies extracted from augmented vertebrae, *Journal of Biomechanics*, **15**: 2732-2736, 2011.

[39] E. KRÖNER, Berechnung der elastischen konstanten des vielkristalls aus den konstanten des einkristalls, *Zeitschrift für Physik* **151**: 504–518, 1958.

[40] SRIHARI KURUKURI, Homogenization of Damaged Concrete Meso-structures using Representative Volume Elements-Implementation and Application to SLang, Master Dissertation, Bauhaus University Weimar Germany, 2005.

[41] D. J. LEKOU, T. T. ASSIMAKOPOULOU, and P. T. PHILIPPIDIS, Estimation of the Uncertainty in Measurement of Composite Material Mechanical Properties During Static Testing, *An International Journal for Experimental Mechanic*, **47**: 430-438, 2011.

[42] A Level Maths Notes: Student t-Distribution Tables. http://www.astarmathsandphysics.com, 1997.

[43] S. LI, L. XIAO, and E. MEAR, Symmetric weak form integral equation method for three-dimensional fracture analysis, *Computer methods in applied mechanics and engineering*, **151**: 435-459, 1998.

[44] Dean-Mo Liu, Porous Ceramic Materials. http://www.ttp.net/978-0-87849-706-5.html, 1995.

[45] P. C. LYSNE and C. M. PERCIVAL, Electric energy generation by shock compression of ferroelectric ceramics: normal-mode response of PZT 95/5, *Journal of Applied Physics*, **46**: 1519-1525, 1975.

110

[46] G. MAIER, S. MICCOLI, G. NOVATI, and S. SIRTORI, Galerkin symmetric boundary element methods in plasticity: formulation and implementation. In eds. J. H. Kane, G. Maier, N. Tosaka, and S. N. Atluri, *Advances in Boundary Element Techniques*, pp. 288–328. Springer-Verlag, Berlin Heidelberg, 1993.

[47] G. MAIER, G. NOVATI, and S. SIRTORI, On symmetrization in boundary element elastic and elastoplastic analysis. In eds. G. Kuhn and H. Mang, *Discretization methods in structural mechanics*, pp. 191–200. Springer-Verlag, Berlin and New York, 1990.

[48] G. MAIER and C. POLIZZOTTO, A Galerkin approach to boundary element elastoplastic analysis, *Computer Methods in Applied Mechanics and Engineering* **60**: 175–194, 1987.

[49] P. A. MARTIN, J. D. RICHARDSON, L. J. GRAY, and J. R. BERGER, On Green's function for a three-dimensional exponentially graded elastic solid, *Proceedings of the Royal Society of London A*, **48**: 1931-1948, 2002.

[50] S. NEMAT-NASSER and M. HORI, *Overall Properties of Heterogeneous Materials*, Amsterdam; New York: North-Holland, 1993.

[51] S. NEMAT-NASSER, and M. TAYA, On effective moduli of an elastic body containing periodically distributed voids, *Quarterly of Applied Mathematics*, **39**: 43-59, 1981.

[52] A. ODGAARD, E. B. JENSEN, and H. J. G. GUNDERSEN, Estimation of structural anisotropy based on volume orientation: a new concept, *Journal of Microscopy* **159**: 335-342, 1990.

[53] A. ODGAARD, J. KABEL, B. VAN RIETBERGEN, M. DALSTRA, and R. HUISKES, Fabric and elastic principal directions of cancellous bone are closely related, *Journal of Biomechanics* **30**: 487-495, 1997.

[54] D. H. PAHR and P. K. ZYSSET, Influence of boundary conditions on computed apparent elastic properties of cancellous bone, *Biomechanics and Modeling in Mechanobiology*, **7**: 463-476, 2008.

[55] J. J. PEREZ-GAVILAN and M. H. ALIABADI, A symmetric Galerkin formulation and dual reciprocity for 2D elastostatics, *Engineering Analysis with Boundary Elements*, **25**: 229-235, 2001.

[56] M.-J. PINDERA, H. KHATAM, A. S. DRAGO, and Y. BANSAL, Micromechanics of spatially uniform heterogeneous media: a critical review, *Journal of Composites: Part B*, **40**: 349-378, 2009.

[57] M. PORFIR, N. GUPTA, and Y. RAYMOND, Characterization of vinyl ester-glass microballoon syntactic foams for marine applications, *Journal Composites Part A: Applied Science and Manufacturing*, **41**: 236-245, 2010.

[58] F. J. RIZZO, P. A. MARTIN, and R. A. ROBERTS, Boundary Elements and a Green's Function Library, *National Institute of Standards and Technology, Technology Administration, U.S. Department of Commerce*, **42**: 309-336, 1994.

[59] F. J. RIZZO, An Integral Equation Approach to Boundary Value Problems of Classical Elastostatics, *Quarterly of Applied Mathematics*, **25**: 83-95, 1967.

[60] A. P. ROBERTS and E. J. GARBOCZI, Elastic Properties of Model Porous Ceramics, *Journal of American Ceramics Society*, **83**: 3041-3048, 2000.

[61] K. SAB, On the homogenization and the simulation of random materials, *European journal of mechanics A Solids*, **11**: 585-607, 1992.

[62] R. E. SETCHELL, Shock wave compression of the ferroelectric ceramic hugoniot states and constitutive mechanical properties, *Journal of Applied Physics*, **94**: 1519-1525, 2003.

[63] S. SIRTORI, G. MAIER, G. NOVATI, and S. MICCOLI, A Galerkin symmetric boundary element method in elasticity: formulation and implementation, *International Journal for Numerical Methods in Engineering*, **35**: 255-282, 1992.

[64] S. SIRTORI, General stress analysis method by means of integral equations and boundary elements, *Meccanica*, **14**: 210-218, 1979.

[65] T. H. SMIT, E. Schneider, and A. ODGAARD, Star length distribution: a volume-based concept for the characterization of structural anisotropy, *Journal of Microscopy*, **191**: 249-257, 1998.

[66] P. SUQUET, Elements of homogenization theory for inelastic solid mechanics, in: Sanchez-Palencia, E.; Zaoui, A. (Eds): Homogenization Techniques for Composite Media. Springer-Verlag, Berlin, Heidelberg, New York, 194-278, 1987.

[67] A. SUTRADHAR, G. H. PAULINO, and L. J. GRAY, *The Symmetric Galerkin Boundary Element Method.* (Springer-Verlag, Berlin, 2008).

[68] The Truth About Forensic Science.
      http://www.thetruthaboutforensicscience.com/htm, June 1. 2005.

[69] C. H. TURNER and S. C. COWIN, Dependence of elastic constants of an anisotropic porous material upon porosity and fabric, *Journal of Materials Science*, **22**: 3178-3184, 1987.

[70] C. H. TURNER and S. C. COWIN, Errors induced by off-axis measurements of the elastic properties of bone, *Journal of Biomechanical Engineering*, **110**: 213-215, 1988.

[71] UNIVERSITY OF CAMBRIDGE, Solid-gas eutectic solidification (Gasar) aluminium foam System.
      http://www.doitpoms.ac.uk/miclib/keywords.php?id=276, Feb 11. 2007.

[72] C.-Y. WANG and M. DENDA, 3D BEM for general anisotropic elasticity, *International Journal of Solids and Structures*, **44**: 7073-7091, 2007.

[73] J. O. WATSON, Hermitian cubic and singular elements for plane strain, Developments in Boundary Element Methods, 4. *London: Elsevier*, pp.1-28, 1986.

[74] W. J. WHITEHOUSE, The quantitative morphology of anisotropic trabecular bone, *Journal of Microscopye*, **101**: (2), 153-168, 1974.

[75] T. ZENG, X. DONG, C. MAO, Z. ZHOU, and H. YANG, Effect of pore shape and porosity on the properties of porous PZT 95/5 ceramics, *Journal of the European Ceramics Society*, **27**: 2025-2029, 2007.

[76] P. K. ZYSSET, A review of morphology-elasticity relationships in human trabecular bone: theories and experiments, *Journal of Biomechanics*, **36**: 1469-1484, 2003.

[77] P. K. ZYSSET and A. CURNIER, An alternative model for anisotropic elasticity based on fabric tensors, *Mechanics of Materials*, **21**: 243-250, 1995.

APPENDIX - PROGRAMS DEVELOPED

The numerical simulation tool developed in MATLAB program for stress/strain
volume averaged calculations is basically composed of two main program files and
three subroutines. These programs and subroutines are presented here.

A.1 Stress/Strain Volume Averages MATLAB codes

The main program for calculating the volume averaged strain from SGBEM stress
analysis. Here $X-$file gives the x and y coordinates, $U-$file is for displacement
information from SGBEM result file. Also, in the program we have to define the
number of of structure sides NS and NV the number of voids in the model under
consideration, r is the volume fracture of the material and H and a are the shape
function variables.

Strain Class E

```
classdef Strain < handle
    % Strain Class

    methods(Static)
        function E = Calculate(X_file, U_file, NS, NV, a, H, r)
            disp 'Calculating strain...'
            [Nodes, MaxX, MaxY] = Node.Build(X_file, U_file);
            Elements = Element.Build(Nodes, NS, NV);
            dH = [diff(H(1), a) diff(H(2), a) diff(H(3), a)];

            E = zeros(3,1);
            for el = Elements
                NX = sum(dH.*([el.Nodes.y]));
                NY = sum(-dH.*([el.Nodes.x]));
                UX = sum(H.*([el.Nodes.bx]));
                UY = sum(H.*([el.Nodes.by]));
                E = E + [NX*UX; NY*UY; (NX*UY + NY*UX)/2];
            end
            E = double(int(E, a, -1, 1) / (r*MaxX*MaxY));
        end
    end
end
```

Stress Class

The main program for calculating the volume averaged stress S:

```
classdef Stress < handle
    % Stress Class

    methods(Static)
        function S = Calculate(X_file, T_file, NS, NV, a, H)
            disp 'Calculating stress...'
            [Nodes, MaxX, MaxY] = Node.Build(X_file, T_file);
            Elements = Element.Build(Nodes, NS, NV);
            dH = [diff(H(1), a) diff(H(2), a) diff(H(3), a)];

            S = zeros(3,1);
            for el = Elements
                X = sum(H .* ([el.Nodes.x]));
                Y = sum(H .* ([el.Nodes.y]));
                TX = sum(H .* ([el.Nodes.bx]));
                TY = sum(H .* ([el.Nodes.by]));
                S = S + [X*TX; Y*TY; (X*TY + Y*TX)/2].*sqrt(sum(
                    dH .* ([el.Nodes.x]))^2 + sum(dH .* ([el.Nodes
                    .y]))^2);
            end
            S = double(int(S, a, -1, 1) ./ (MaxX*MaxY));
        end
    end
end
```

This subroutine is only for classify the elements of the structure.

```
classdef Element < handle
    % Element Class
    properties
        Nodes
    end
    methods(Static)
        function Elements = Build(Nodes, NS, NV)
            if (NS < 3)
                return;
            end
            Elements = Element.empty();
            for side = 1:(NS-1)
                while (~((Nodes(1).x == Nodes(2).x) && (Nodes(1).
                    y == Nodes(2).y)))
                    Elements(end+1).Nodes = Nodes(1:3);
                    Nodes(1:2) = [];
```

```
                    end
                    Nodes(1) = [];
                end

            N = Elements(1).Nodes(1);
            for side = NS
                while (~((Nodes(1).x == N.x) && (Nodes(1).y == N.
                    y)))
                    Elements(end+1).Nodes = Nodes(1:3);
                    Nodes(1:2) = [];
                end
                Nodes(1) = [];
            end
            if (NV < 1)
                return;
            end

            % Note: It is assumed that all voids contain an equal
                amount of elements
            EpV = floor(length(Nodes) / (NV * 2));
            for void = 1:NV
                N = Nodes(1);
                for E = 1:(EpV-1)
                    Elements(end+1).Nodes = Nodes(1:3);
                    Nodes(1:2) = [];
                end
                for E = EpV
                    Elements(end+1).Nodes = [Nodes(1:2) N];
                    Nodes(1:2) = [];
                end
            end
        end
    end
end
```

This subroutine is only for classify the three nodes of each element of the structure.

```
classdef Node < handle
    % Node Class

    properties
        x
        y
        bx
        by
    end
```

```matlab
methods(Static)
    function [Nodes, MaxX, MaxY] = Build(X_file, B_file)
        XY = load(X_file);
        B = load(B_file);

        Nodes(length(XY)) = Node;

        for i = 1:length(Nodes)
            Nodes(i).x = XY(i,1);
            Nodes(i).y = XY(i,2);
            Nodes(i).bx = B(i,2);
            Nodes(i).by = B(i,3);
        end

        MaxX = max(XY(:,1));
        MaxY = max(XY(:,2));
    end
end
end
```

This subroutine called Script.

```matlab
clear;
clc;
format compact;
syms a;
% S = Stress.Calculate(X_file, T_file, NS, NV, a, [H1 H2 H3])NV
    is the # of
% pores NS # of model sides in case of rectangle NS=4 triangle NS
    = 3......
S = Stress.Calculate('X.dat', 'T.dat', 4, 9, a, [1/2*a*(a-1) (1-a
    )*(1+a) 1/2*a*(a+1)])
% E = Strain.Calculate(X_file, U_file, NS, NV, a, [H1 H2 H3], r)
    where r is the volume fracture ratio
E = Strain.Calculate('X.dat', 'U.dat', 4, 9, a, [1/2*a*(a-1) (1-a
    )*(1+a) 1/2*a*(a+1)], 0.97)
```

A.2 Quant3D Output File

Here present two output files from Quant3D software.

A.2.1 MIL Calculation Output File

```
MIL calculations for sample: 1              .
Threshhold range , BV/TV:          90.0000-255.000 0.948251
Random Orientations:     1000
Vector sampling:         Graphics
Random Points:. 2000 ·
Data orientation (strike , dip, up):        90.0000 0.000000            1
MIL Ellipse Eigenvectors:                            Trend   Plunge
     0.999166         0.0406076       -0.00418269           87.6727
               0.239651
    -0.0406034         0.999175        0.00109310           177.673
            0.0626302
     0.00422363      -0.000922360        0.999991           282.319
               89.7523
MIL Ellipse Eigenvalues:
     0.275417         .   1.87685            569.423
MIL Ellipse (H) Eigenvalues:
     0.711711         0.272637           0.0156524
MIL Ellipse Tensor (M):
     0.288210        -0.0671873           2.40377
    -0.0671873         1.87469          -0.523205
     2.40377         -0.523205            569.412
MIL (H) DA        I         E         Tb.N
     45.4697       · 0.0219927           0.616928            6.59057
MIL Fabric Eigenvectors:                             Trend   Plunge
    -0.998671         0.0505584         0.0100468           92.8982
               0.575649
     0.0505868         0.998716         0.00259199          182.900
            0.148510
    -0.00990285         0.00309678       -0.999946           287.365
             89.4055
MIL Fabric Eigenvalues:
     0.647973         0.333551           0.0184765
MIL Fabric Tensor:
     0.647106        -0.0158658        -0.00627470
    -0.0158658         0.334352         0.00113538
    -0.00627470        0.00113538         0.0185421
MIL (F) DA        ·I        E
     35.0701         0.0285143           0.485239
```

118

A.2.2 SVD and SLD Calculations Output File

Star length and volume calculations for sample: 1
Threshhold range, BV/TV: 91.0000−255.000 0.944686
Random Orientations: 1000
Vector sampling: Graphics
Random Points: 2000
Data orientation (strike, dip, up):   90.0000 0.000000   1
SVD Eigenvalues: Eigenvectors   Trend
   Plunge
      0.813770   0.999874   −0.0158527   0.000000
                 270.908   0.000000
      0.186230   0.0158527   0.999874   0.000000
                 180.908   0.000000   .
      0.000000   0.000000   0.000000   1.00000
                 270.000   90.0000
SVD Fabric Tensor:
      0.813612   −0.00994697   0.000000
    −0.00994697   0.186388   0.000000
      0.000000   0.000000   0.000000
SVD DA   I   E   Sum(tau)
         Inf   0.000000   0.771151   2.82957e+007
SLD Eigenvalues: Eigenvectors   Trend
   Plunge
      0.668935   0.999991   −0.00415241   0.000000
                 270.238   0.000000
      0.331065   0.00415241   0.999991   0.000000
                 180.238   0.000000
      0.000000   0.000000   0.000000   1.00000
                 270.000   90.0000
SLD Fabric Tensor:
      0.668929   −0.00140296   0.000000
    −0.00140296   0.331071   0.000000
      0.000000   0.000000   0.000000
SLD DA   I   E   Sum(tau)
         Inf   0.000000   0.505086   17274.0
Thickness (minimum line length at each point, non−zero points
   only)
Mean   Variance   Skewness   Kurtosis   Min
   Max   .
1.65552 0.430431   −0.153742   −0.0488055   0.0360000
                 3.39647
Thickness histogram
bin   num   norm
      0.188693   96   0.0492055
      0.566079   87   0.0445925
      0.943464   148   0.0758585

119

1.32085	615	0.315223
1.69824	153	0.0784213
2.07562	545	0.279344
2.45301	199	0.101999
2.83039	68	0.0348539
3.20778	40	0.0205023
3.58516	0	0.000000